Astronomy Letters, Vol. 29, No. 9, 2003, pp. 567–572. Translated from Pis'ma v Astronomicheskiĭ Zhurnal, Vol. 29, No. 9, 2003, pp. 643–648.

A Difference Method of Searching for Spectral–Spatial Fluctuations of the Cosmic Microwave Background Radiation

V. K. Dubrovich[1] and A. T. Bajkova[2*]

[1] *Special Astrophysical Observatory, Russian Academy of Sciences, St. Petersburg, Russia*

[2] *Institute of Applied Astronomy, Russian Academy of Sciences, St. Petersburg, Russia*

Received February 21, 2003

Abstract—We consider methods of searching for the spectral–spatial fluctuations of the cosmic microwave background radiation that were formed in the early Universe. Based on the narrow-band spatial-frequency properties of these fluctuations, we suggest a difference method of their search. We describe the method and present our simulation results. This technique is shown to have a significant advantage over the existing methods. We give recommendations to optimize the observing and reduction procedures.

Key words: *theoretical and observational cosmology.*

INTRODUCTION

The most recent achievements in studying the primary spatial fluctuations of the cosmic microwave background radiation (CMBR) temperature T_r provide a reliable experimental basis for choosing a theory of the evolution of matter in the early Universe (Sakharov 1968; Melchiorri *et al.* 2000). Thus, we can speak with greater confidence about the formation models of protoobjects at the postrecombination epoch. The increase in the matter overdensity with decreasing redshift z and the manifestations of peculiar processes in the cooling matter give rise to secondary CMBR fluctuations (Dubrovich 1977, 1997). Searching for, identifying, and studying these fluctuations are increasingly becoming of relevant interest. The importance of such studies lies in the possibility of obtaining unique information about the particular features of the evolution of matter in the pregalactic Universe and determining the role of various hidden forms of matter. At this epoch, the latter can manifest themselves to a much greater extent than they can during the formation of primary fluctuations. In particular, we can estimate the fraction of the radiation additional to the CMBR that is attributable to unstable dark matter.

In this problem, an optimal technique of searching for the secondary fluctuations is of great importance. Here, we imply an optimization in those properties that are known a priori from the physics of their formation processes. The most important property is the strong frequency dependence of some of the secondary fluctuations—spectral–spatial fluctuations (SSFs).

Therefore, our goal is to discuss one of the SSF searching techniques. As we show below, this technique allows the SSF detection probability to be significantly increased, which is crucially important because of their small theoretically predicted amplitude. We emphasize once again that we are dealing here with the searching method rather than with the SSF detection probability. Since the latter depends on a large number of unknown parameters, any new, more efficient method of their detection or limitation from above is of great importance.

FORMATION MECHANISMS AND PECULIARITIES OF THE FLUCTUATIONS

We know several processes that give rise to spatial CMBR temperature fluctuations. When $\delta T/T_r$ fluctuations are formed at the recombination stage, they result from gravitational effects (Sachs and Wolfe 1967) and scattering by free electrons (Zeldovich and Sunyaev 1969). These fluctuations have a blackbody spectrum because the scattering cross section does not depend on the photon frequency. A relatively low density of free electrons is characteristic of the later expansion stage of the Universe. At this stage, various extrapolations of the standard mechanisms that work in the interstellar medium of galaxies and quasars are considered most extensively (Lepp and Shull 1984). All of these schemes are based on the presence of internal energy sources in

*E-mail: bajkova@quasar.ipa.nw.ru

1063-7737/03/2909-0567$24.00

the protoobject. In this case, the radiation intensity is determined by specific models and can take on values in a wide range. Even a simple limitation of the $\delta T/T_r$ amplitude from above makes sense. The existing constraints in broad-band observations can be recalculated to the narrow bands that we use. At a wavelength of 6 cm in the 1-MHz band, this procedure yields $\delta T/T_r < 5 \times 10^{-3}$. The scattering by small density inhomogeneities with a peculiar velocity V_p and opacity to electromagnetic radiation can be one of the likely formation mechanisms of the CMBR temperature fluctuations after hydrogen recombination (Dubrovich 1977). Peculiar velocities of various spatial scales are predicted in all of the evolutionary models (Zeldovich and Sunyaev 1969; Silk 1968). At the same time, different factors can be responsible for the opacity.

When the temperature of the matter and radiation becomes lower than 500–600 K, the opacity can result from the scattering in molecular lines if there are various chemical elements, namely, He, D, Li, C, N, and O, in the matter. Previously (Dubrovich 1977), we considered the formation mechanism of these fluctuations for the case of opacity in lines of such molecules as LiH, HeH^+, $H2D^+$, etc. In addition to pure scattering, the luminescent transformation of superequilibrium photons and a combination of the two mechanisms are possible (Dubrovich 1977, 1997). In all of these cases, the fluctuations exhibit a significant feature—a strong frequency dependence of the effect. Thus, if an object contains a gas of certain molecules and has a redshift z, then it will be seen only at the frequencies

$$\nu_i = \nu_{0i}/(1+z), \tag{1}$$

where ν_{0i} is the discrete set of laboratory transition frequencies in a given molecule. This implies that we will be able to see the same object at different but discrete frequencies. Conversely, if an object is seen at a given frequency, then it can have any of the redshifts

$$z_i = \nu_{0i}/\nu - 1. \tag{2}$$

One of the corollaries of (1) and (2) is that we will see the same object with a redshift z_1, for example, at a frequency ν_1 and will not see it at a different frequency ν_2 if the following conditions are satisfied:

$$\nu_1 < \nu_2, \quad \nu_1 = \nu_{0i}/(1+z_1), \qquad \nu_2 < \nu_{0(i+1)}/(1+z_1). \tag{3}$$

Here, we assume that the object's linear size L is very small. A more accurate condition on $\Delta\nu$ that includes the object's finite size will be given below. At the same time, at the frequency ν_2, we will see objects with the redshift z_2, according to (2), that can be different than those seen at the frequency ν_1. In the case of a low opacity, the CMBR temperature-fluctuation amplitude $\delta T/T_r$ due to the object's peculiar velocity V_p is roughly defined (Dubrovich 1977) as

$$\delta T/T_r = V_\mathrm{p}\tau/c, \tag{4}$$

where τ is the object's optical depth in molecular lines ($\tau < 1$) and c is the speed of light.

Various possible values were calculated by different authors (Dubrovich 1977; Lepp and Shull 1984; Puy and Signore 1996). Clearly, they directly depend on the abundance of a particular molecule, which, in turn, are complex functions of z. The following general assertion can be made from expression (4): this mechanism can produce an effect only with $\delta T/T_r < V_\mathrm{p}/c < 10^{-3}$.

An object's linear size L is related to its angular size θ and the width of the band $\Delta\nu$ in which this object can be seen. For low z, the angular size of the object (at its constant linear size L) decreases with increasing distance and increases at z higher than some value. Currently available observational data favor the model of a flat expanding Universe with a cosmological constant Λ. The exact relations between θ and z in this model contain the parameters Ω_m and Ω_Λ—the ratios of the matter density n_m and the vacuum density to the critical density n_c, respectively ($\Omega_m + \Omega_\Lambda = 1$), and have the form (Sahni and Starobinsky 2000)

$$\theta = (H_0 L/c)(1+z)/\phi(z),$$

$$\phi(z) = \int_0^z [\Omega_m(1+z)^3 + \Omega_\Lambda]^{-1/2} dz.$$

For high z, $H_0 = 60\,\mathrm{km\,s^{-1}\,Mpc^{-1}}\,h_{60}$, $\Omega_m = 0.3$, and L in Mpc, we obtain

$$\theta \sim 15'' h_{60} L(1+z).$$

On the other hand, the front and back edges of the cloud are at different distances from us, i.e., have different z. This z difference is related to L by

$$\Delta z/(1+z) = (H_0 L/c)[\Omega_m(1+z)^3 + \Omega_\Lambda]^{1/2}.$$

The fact that the cloud spans a range of redshifts z implies that if it emits or reflects radiation locally in narrow lines, then all of the radiation will span the frequency range $\Delta\nu$, with

$$\Delta\nu/\nu = \Delta z/(1+z).$$

Consequently,

$$\Delta\nu/\nu \sim \theta\phi(z)[\Omega_m(1+z)^3 + \Omega_\Lambda]^{1/2}(1+z)^{-1}.$$

For high z and $\Omega_m = 0.3$, we numerically obtain

$$\Delta\nu/\nu \sim 1.3 \times 10^{-3}(\theta/1')[\phi(z)/\phi(20)](1+z)^{1/2}. \quad (5)$$

If we carry out observations simultaneously with two receivers with a frequency difference $\Delta\nu$, then we will see fluctuations larger than θ on both receivers. If the fluctuation is smaller, then it will be seen only on one receiver, while only a background (or a different object) will be seen on the other receiver at this point in the sky (Dubrovich 1982). Thus, to within noise, the correlation function of these two observations will be zero on small scales and nonzero on scales larger than some scale. The presence of a distinct break is possible only if all of the objects have the same size L. Actually, there is a certain spectrum of scales. The effect considered here shows that the initial spectrum can be significantly deformed. A more detailed study of this issue is beyond the scope of our paper. However, we see from the above discussion that analysis of the SSFs will provide additional information about the matter parameters and redshifts z for most of the protoobjects.

Molecular scattering in several lines results in a superposition of the images of different objects with different z. As we showed previously (Dubrovich 1977), the cosmological LiH and HD^+ molecules can exist at $50 < z < 200$. In this case, the wavelengths of the LiH lines lie within the range from 13 cm for $z = 200$ and $i = 1$ to 0.5 cm for $z = 50$ and $i = 6$. For HD^+, this range is from about 4.4 to 0.2 cm. As a result, the number of fluctuations increases at high frequencies. The power spectra of the maps obtained at centimeter and millimeter wavelengths must be distinguished by an increase in the fraction of small-scale fluctuations in the latter case.

The above estimates and relations hold for objects that freely expand according to the Hubble law. Actually, however, at late stages, their expansion slows down and their contraction under self-gravitation begins. In this case, the line width can be much smaller, while the amplitude can be larger (Zeldovich 1978).

THE DIFFERENCE METHOD

The difference method may be considered as an alternative to the method of analyzing the correlation function described above. In this case, the first derivative of the spatial distortions with respect to frequency is the subject of analysis.

The suggested method consists in analyzing the difference between the two-dimensional CMBR maps measured at different frequencies and reduced to the same beam. Clearly, the constructed difference maps carry information only about the secondary fluctuations, because the primary CMBR fluctuations, which are present on both maps due to their blackbody spectrum, will be cancelled out after the subtraction.

Let the difference between the frequencies at which the CMBR maps are measured be $\Delta\nu_1$. Let the limiting angular fluctuation size θ_1 correspond to this frequency difference, according to expression (5). Clearly, we will see fluctuations larger than θ_1 on both maps. When one map is subtracted from the other, fluctuations larger than θ_1 will be cancelled out, and we will see only fluctuations smaller than θ_1 on the residual map. Obviously, this fact will be reflected on the angular power spectrum of the difference map, which is virtually zero at frequencies $l < l_1$ and nonzero at frequencies $l > l_1$, where $l_1 \sim 1/\theta_1$ is the frequency of the spectral break. Now, let the frequency difference be $\Delta\nu_2$, where $\Delta\nu_2 > \Delta\nu_1$. The angular fluctuation size θ_2 corresponds to this frequency, with $\theta_2 > \theta_1$ (according to (5)). In this case, we will see fluctuations smaller than θ_2 on the difference map. The angular power spectrum of the difference map will have a break frequency $l_2 \sim 1/\theta_2 < l_1$.

Figures 1 and 2 illustrate the difference method. The four maps (1, 2, 3, and 4) measured at four different frequencies (ν_1, ν_2, ν_3, and ν_4) are shown in the upper row. All of the maps have the same angular power spectrum, which is indicated by the heavy dashed line in Fig. 2. The three difference maps 1–2, 1–3, and 1–4 obtained by the subtraction of maps 2, 3, and 4, respectively, from map 1 are shown in the lower row of Fig. 1. The frequency differences obey the relation $\nu_1 - \nu_2 > \nu_1 - \nu_3 > \nu_1 - \nu_4$. Accordingly, the maximum size of the fluctuations seen on the difference maps satisfies the relation $\theta_{1-2} > \theta_{1-3} > \theta_{1-4}$. Qualitatively, the fluctuation scale can also be estimated visually from the maps shown in Fig. 1. The angular power spectra of the difference maps 1–2, 1–3, and 1–4 are indicated in Fig. 2 by the solid, dotted, and thin dashed lines, respectively. The break points in the spatial spectra satisfy the relation $l_{1-2} < l_{1-3} < l_{1-4}$.

In the example considered above, we assumed that the measured CMBR maps contain nothing but the primary and secondary CMBR fluctuations. In practice, however, the measured maps of various sky regions contain many background components, such as pixel noise, a background of extragalactic unresolved sources, synchrotron radiation, the Sunyaev–Zeldovich effect, Galactic dust, and the like. Pixel noise causes the greatest trouble to the difference method. The remaining components, which are characterized by a relatively small spectral index compared to the secondary CMBR fluctuations being analyzed, are successfully cancelled out after the subtraction of the maps. Below, we present the simulation

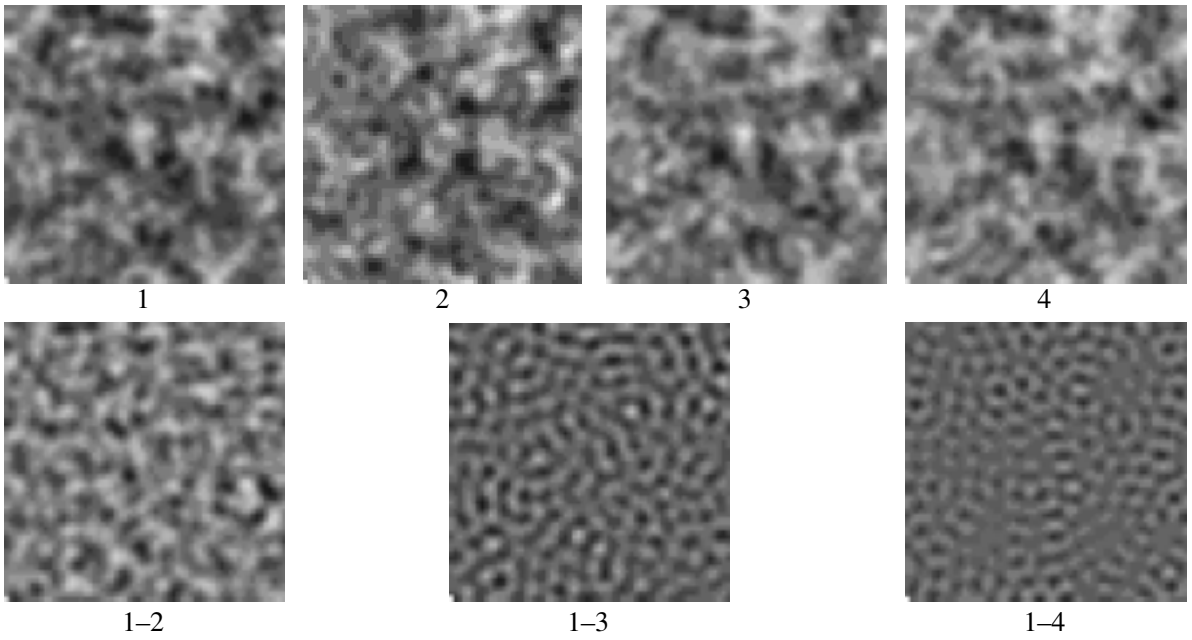

Fig. 1. An illustration of the difference method without pixel noise. Maps 1, 2, 3, and 4 at frequencies ν_1, ν_2, ν_3, and ν_4, respectively; 1–2, 1–3, and 1–4 are the difference maps obtained after the subtraction of maps 2, 3, and 4, respectively, from map 1.

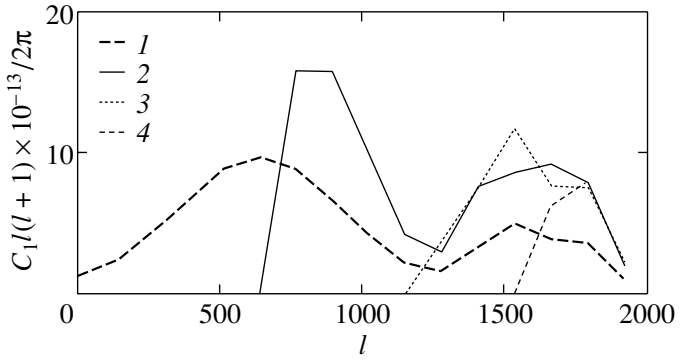

Fig. 2. The angular power spectra of maps 1, 2, 3, and 4 (*1*), and difference maps 1–2 (*2*), 1–3 (*3*), and 1–4 (*4*) corresponding to Fig. 1.

results for the difference method in the presence of significant pixel noise on the measured maps.

We added the square of the white Gaussian noise with a zero mean to the original maps 1, 2, 3, and 4 (Fig. 1). The signal-to-noise ratio for each map was about 1.44. The same noise realization was added to maps 2–4, which is of no fundamental importance, because we analyze the differences between each of these maps and the first map to which a different noise realization was added. The noisy maps 1–4 are shown in the upper row of Fig. 3. The difference maps 1–2, 1–3, and 1–4, which were subjected to low-frequency filtering with the pass band equal to the width of the CMBR spectrum, are shown in the lower row of Fig. 3. As we see from the figures, the presence of noise in the low-frequency range of the CMBR spectrum resulted in an appreciable blurring of the small-scale residual fluctuation structure. Therefore, the angular power spectrum of the difference maps should be analyzed to obtain the necessary qualitative and quantitative parameters. The angular power spectra of the difference maps are shown in Fig. 4. As we see, the break in the angular power spectra that corresponds to the joint of the pure-noise and CMBR + noise spectra clearly shows up even without the map preprocessing aimed at reducing the noise in the CMBR band. Obviously, at a higher noise level, more complex additional processing may be required (Bajkova 2002).

The accurately measured break in the angular

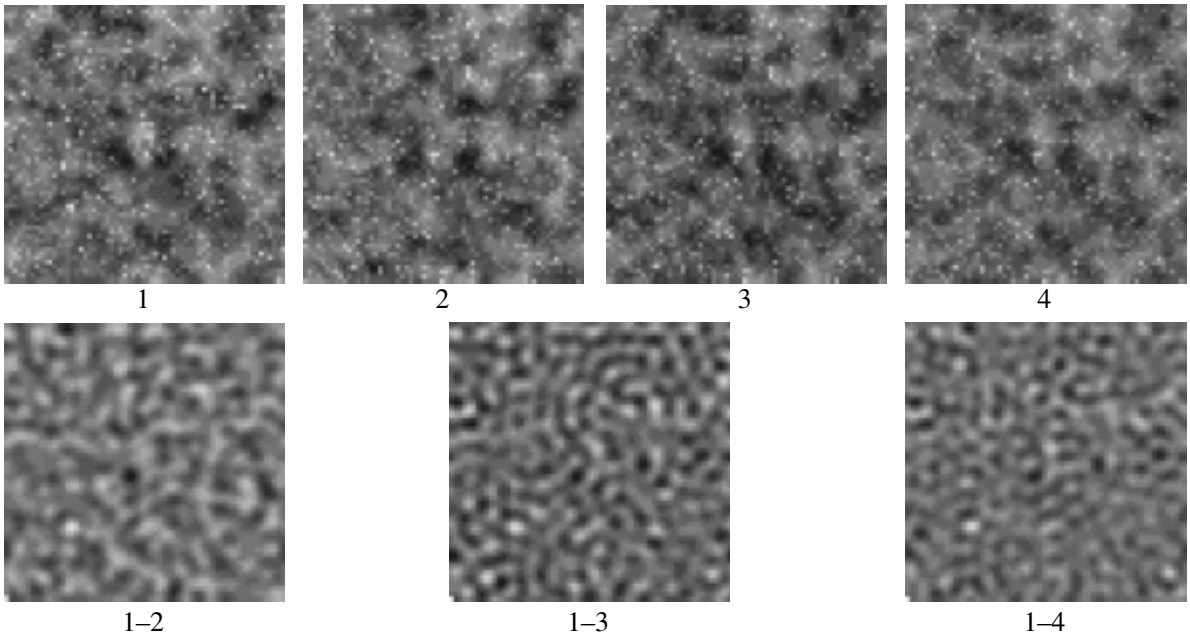

Fig. 3. Same as Fig. 1 but with pixel noise.

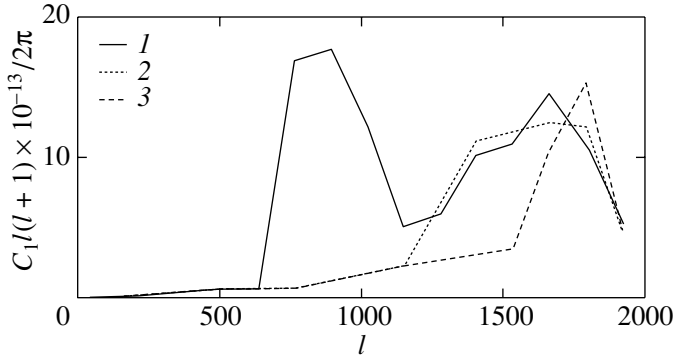

Fig. 4. The angular power spectra of the difference maps 1–2 (*1*), 1–3 (*2*), and 1–4 (*3*) corresponding to Fig. 3.

power spectrum l_c allows θ_c to be estimated, which, in turn, makes it possible to determine the deceleration parameter z and the type of cosmological molecules by using the technique described in detail previously (Dubrovich 1977).

CONCLUSIONS

Below, we formulate our main conclusions. The presence of molecular clouds at the early evolutionary stage of the Universe ($z > 100$) must give rise to spectral–spatial CMBR fluctuations. The amplitudes of these fluctuations can reach 3×10^{-3} K for simple scattering and exceed this value for sufficiently powerful early energy release, which allows them to be studied in detail. Here, we suggested a difference method of searching for the spectral–spatial CMBR fluctuations formed in the early Universe. It is based on the narrow-band spatial-frequency properties of these fluctuations. Our simulation results lead us to conclude that this method is more efficient than the previously suggested methods even in the presence of significant instrumental measurement noise. It should be noted that the difference between primordial molecules can be detected in principle and each of them can be identified. In addition, the z range in which these molecules exist and the parameter Ω_m can be determined.

REFERENCES

1. A. T. Baĭkova, Izv. Vyssh. Uchebn. Zaved., Radiofiz. **45**, 909 (2002); astro-ph/0205112.
2. V. K. Dubrovich, Astron. Astrophys. **324**, 27 (1997).

3. V. K. Dubrovich, Izv. Spets. Astrofiz. Obs. **15**, 21 (1982).
4. V. K. Dubrovich, Pis'ma Astron. Zh. **3**, 243 (1977) [Sov. Astron. Lett. **3**, 128 (1977)].
5. S. Lepp and J. M. Shull, Astrophys. J. **280**, 465 (1984).
6. A. Melchiorri, P. A. R. Ade, P. de Bernardis, *et al.*, Astrophys. J. **536**, L63 (2000).
7. D. Puy and M. Signore, Astron. Astrophys. **305**, 371 (1996).
8. R. K. Sachs and A. M. Wolfe, Astrophys. J. **147**, 73 (1967).
9. V. Sahni and A. Starobinsky, Int. J. Mod. Phys. D **9**, 373 (2000).
10. A. D. Sakharov, Dokl. Akad. Nauk SSSR **177**, 70 (1968) [Sov. Phys. Dokl. **12**, 1040 (1968)].
11. J. Silk, Astrophys. J. **151**, 459 (1968).
12. Ya. B. Zeldovich, Pis'ma Astron. Zh. **4**, 165 (1978) [Sov. Astron. Lett. **4**, 88 (1978)].
13. Ya. B. Zeldovich and R. A. Sunyaev, Astrophys. Space Sci. **4**, 301 (1969).

Translated by V. Astakhov

Astronomy Letters, Vol. 29, No. 9, 2003, pp. 573–578. Translated from Pis'ma v Astronomicheskiĭ Zhurnal, Vol. 29, No. 9, 2003, pp. 649–655.

The First Hours of the Optical Afterglow from the Cosmic Gamma-Ray Burst 030329

R. A. Burenin[1]*, R. A. Sunyaev[1], M. N. Pavlinsky[1], D. V. Denisenko[1], O. V. Terekhov[1], A. Yu. Tkachenko[1], Z. Aslan[2], I. Khamitov[2], K. Uluch[2], M. A. Alpar[3], U. Kiziloglu[4], A. Baikal[4], I. F. Bikmaev[5], N. R. Sakhibullin[5], and V. F. Suleymanov[5]

[1]*Space Research Institute, Russian Academy of Sciences, Profsoyuznaya ul. 84/32, Moscow, 117810 Russia*
[2]*TUBITAK National Observatory, Antalia, Turkey*
[3]*Sabanshi University, Ankara, Turkey*
[4]*METU, Ankara, Turkey*
[5]*Kazan State University, Kazan, Russia*

Received April 28, 2003

Abstract—We describe the first results of our observations of the exceptionally bright optical afterglow from the cosmic gamma-ray burst (GRB) of March 29, 2003 (030329), with the 1.5-m Russian–Turkish telescope (RTT150) installed at the TUBITAK National Observatory (Turkey) at Mount Bakyrlytepe. RTT150 was one of the first medium-class telescopes pointed at the afterglow. The observations began as early as about six hours after the GRB. During the first five hours of our observations, the $BVRI$ flux fell off exactly as a power law with the same slope -1.19 ± 0.01. Subsequently, in all of the $BVRI$ bands, we observed the same increase in the power-law slope of the light curve to a value that was later recorded during the observations at observatories in the western hemisphere. The break in the power-law light curve occurs at $t - t_0 \approx 0.57$ days (13.5 h) and lasts for about 0.2 days. Apart from this smooth decrease in the flux, the afterglow exhibited no flux variability. The upper limits on the variability are 10–1% on time scales of 0.1–1000 s, respectively. The $BVRI$ spectral flux distribution during the first night of our observations closely corresponds to a power-law spectrum with a spectral index $\alpha = 0.66 \pm 0.01$. The change in the power-law slope of the light curve at the end of our observations is probably attributable to the deceleration of the ultrarelativistic jet to a gamma factor when its structural features begin to show up in the light curve. The radio, optical, and X-ray broadband spectrum is consistent with the assumption about the synchrotron radiation of the ultrarelativistic jet. This unique object continues to be observed with RTT150.

Key words: *cosmic gamma-ray bursts, afterglows, optical observations.*

INTRODUCTION

Although the bulk of the energy of cosmic gamma-ray bursts (GRVs) is radiated in the hard X-ray and gamma-ray ranges, optical observations gave crucial information about their sources. Optical observations allowed us to measure the redshifts of some of the GRBs and thereby to establish the fact that the GRB sources are at cosmological distances. Observations of optical afterglows from GRBs became attainable after it became possible to measure the celestial coordinates of GRB sources with an accuracy of several arcminutes for several hours (at that time, with the BeppoSAX satellite; see, e.g., Costa *et al.* 1997a). The first optical afterglow was discovered by Bond (1997). GRB afterglows were also detected in other wavelength ranges, from the radio to gamma rays (see, e.g., Taylor *et al.* 1998; Costa *et al.* 1997b; Burenin *et al.* 1999).

At present, the total number of observed optical afterglows is already several dozen. The light curves of GRB afterglows in all wavelength ranges are generally described by power laws or their combination with breaks at different times after the GRB, which are attributed to changes in the motion of high-velocity jets (for references, see Frail *et al.* 2001). Occasionally, a different kind of variability that was explained as a contribution from the parent supernova (Sokolov 2001) is also observed.

The bright cosmic GRB of March 29, 2003 (030329), was detected with instruments onboard the HETE-II satellite at 11:37:14.7 UT. The peak flux

*E-mail: burenin@hea.iki.rssi.ru

was 7×10^{-6} erg s^{-1} cm^{-2} in the energy range 30–400 keV, and the duration was about 30 s (Vanderspek *et al.* 2003; Golenetskii *et al.* 2003). Two hours later, a very bright optical transient was discovered in the GRB error region (Peterson and Price 2003; Torii 2003). This object immediately became the main target for many telescopes worldwide. Extensive photometric and spectroscopic observations, which were well documented in GCN circulars (see, e.g., Burenin *et al.* 2003; Khamitov *et al.* 2003), were carried out. The redshift of this object was found to be $z = 0.1685$ (Greiner *et al.* 2003). Thus, this is the nearest GRB of those observed so far (except GRB 980425, if it was actually associated with the Supernova 1998bw at $z = 0.0085$). At such a distance to the source, the "isotropic" gamma-ray energy release of the GRB is about 10^{52} erg. Subsequently, the contribution from the parent supernova showed up in the spectrum of the transient (Stanek *et al.* 2003).

In this paper, we describe the first results of our observations of this exceptionally bright optical afterglow with the 1.5-m Russian–Turkish telescope RTT150[1] (the TUBITAK National Observatory, Turkey, Mount Bakyrlytepe, 2547 m, $2^{h}01^{m}20^{s}$ E, 36°49′30″ N). Because of its geographic position, RTT150 was one of the first medium-class telescopes pointed at the afterglow. The observations with RTT150 began as early as six hours after the GRB. At this time, the R magnitude of the afterglow was 14^{m}, which is $3–4^{m}$ brighter than the brightest optical afterglows of the GRBs observed so far on this time scale.

OBSERVATIONS

Our observations were carried out with an Apogee AP47p CCD array mounted at the Cassegrain focus of the telescope (1 : 7.7). This is a back-illuminated 1056×1024 CCD array with a pixel size of 13×13 μm. We used a 2×2 grouping mode, with the pixel angular size being $0''.46 \times 0''.46$. As usual, we subtracted a median zero-exposure frame and dark current from the images and then divided the images by a flat field. The images were reduced by using the standard IRAF (Image Reduction and Analysis Facility) package[2] and our own software.

From the very beginning of the night of March 29, 2003, at 17:50 UT, the telescope was pointed at the afterglow of GRB 030329. The observations continued until 01:30 UT, when the zenith distance of the object exceeded 68°. Throughout this period, we obtained images of the field sequentially in the $BVRI$ bands of the Bessel system with exposures of 10–30 s; the readout time was about 10 s. A total of 175 images were obtained in each band. Figures 1a and 1b show the images of the optical transient's field obtained on this night and on April 10, respectively.

PHOTOMETRY

All of the photometric measurements on the first night of our observations were made relative to the bright neighboring star denoted by the letter A in Fig. 1. This is the brightest star in our field. However, it is also much fainter than the afterglow of GRB 030329. Therefore, the measurement errors of the flux from the afterglow were dominated by the measurement errors of the flux from this star. We checked the results of our measurements by using other field stars, but all of them are much fainter than star A and their use as reference stars did not reduce the measurement errors.

To perform photometric calibration, we observed standard stars from the catalog by Landolt (1992) before and after the observations of the afterglow. These observations indicate that the night was almost exactly photometric. A slight decrease in atmospheric transparency was observed at the beginning of the night. The transparency was lower than the typical one by approximately 10% and smoothly returned to the typical value on a photometric night in several hours. This is clearly seen not only from the photometric solutions that we obtained from the observations of Landolt's stars but also from the magnitude measurements of star A and other field stars.

The photometric calibration of our measurements is in full agreement with the photometry of this field from the communication by Henden (2003). In this communication, it was rightly pointed out that star A greatly differed in color from the afterglow of GRB 030329 and that its use as a reference star could lead to additional systematic errors because of the different dependences of the decrease in flux on airmass. However, our observations of Landolt's stars revealed no significant changes of the color coefficients in our photometric solutions at different airmasses or during the decrease in transparency in the first hours of our observations. We estimated the systematic measurement error of the fluxes to be no more than 1%.

The R-band light curve for the afterglow of GRB 030329 obtained on the first night of our observations is shown in Fig. 2a. In the first five hours of our observations, the decrease in the flux from the afterglow closely followed a power law with a slope of -1.19 ± 0.01. Subsequently, for approximately three hours, the power-law slope of the light

[1] http://hea.iki.rssi.ru/AZT22/RUS/; http://www.tug.tubitak.gov.tr

[2] http://tucana.tuc.noao.edu/

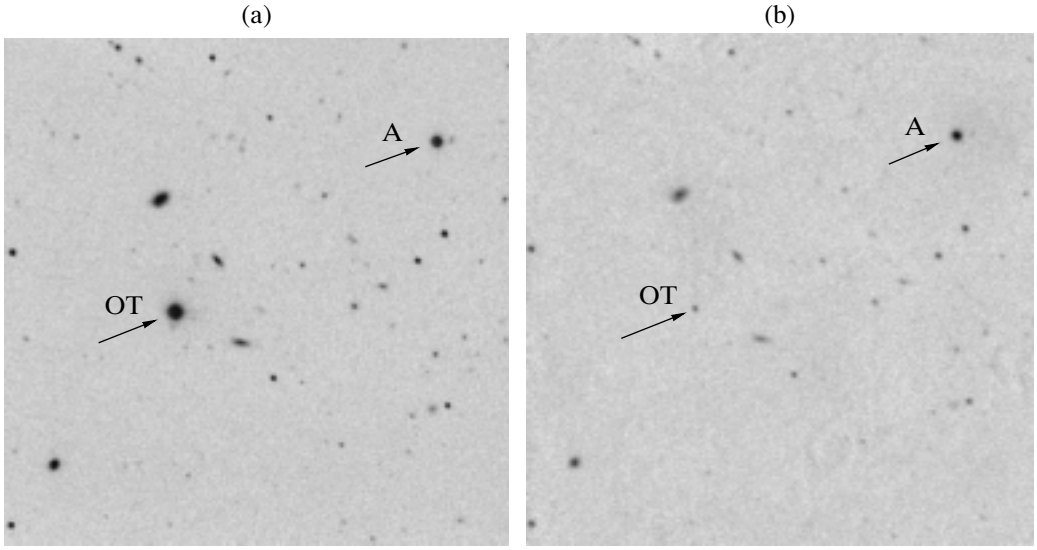

Fig. 1. The images of the afterglow from GRB 030329 obtained with RTT150 on (a) March 29 and (b) April 10, 2003. The arrows indicate the afterglow (OT) and the comparison star (A) that was used to construct the light curve.

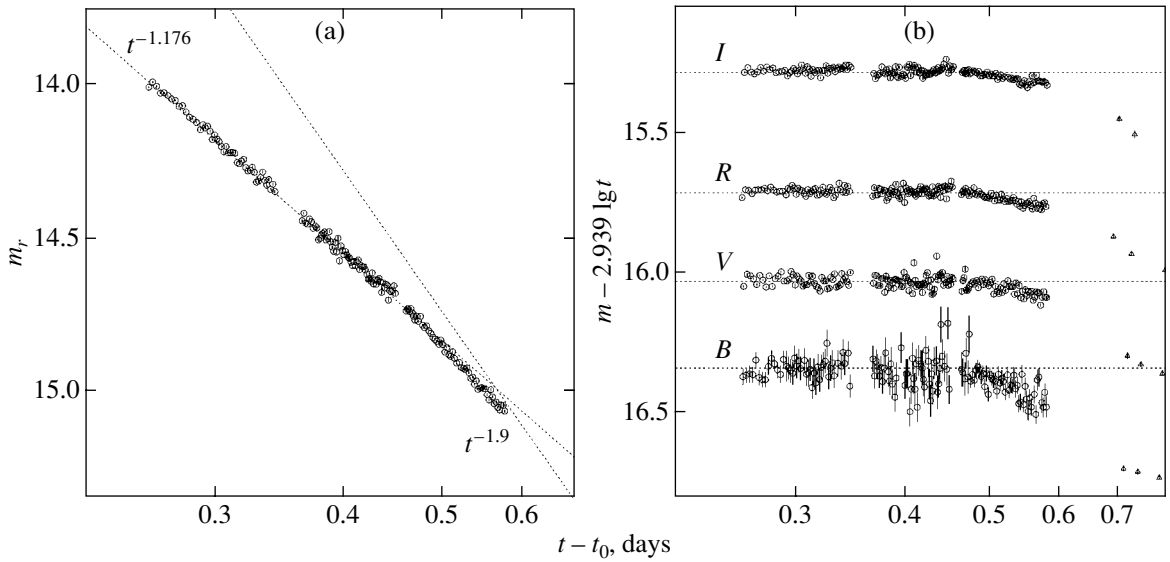

Fig. 2. The light curves for the afterglow of GRB 030329 on the first night of our observations: (a) in the R band (also shown is the power law with a slope of -1.9 obtained from the observations at $t - t_0 > 0.6$ days (Garnavich *et al.* 2003)); and (b) in the $BVRI$ bands minus the power-law decrease in flux with a slope of -1.8 ± 0.01 obtained by fitting the R-band data (the data from the communication by Fitzgerald and Orosz (2003) at $t - t_0 > 0.7$ are represented by triangles).

curve increased to a value that was later recorded at observatories in the western hemisphere. Figure 2a also shows the power law with a slope of -1.9 that was obtained by fitting the light curve using the observations with the 1.2-m FLWO telescope performed after our observations at $t - t_0 > 0.6$ days (Garnavich *et al.* 2003).

Figure 2b shows the $BVRI$ light curves minus the power-law slope that fits the R-band light curve in the first five hours of our observations (see above). We see that the power-law decrease in flux is the same in all of the four bands. The power-law slopes in the BVI bands are -1.22 ± 0.05, -1.19 ± 0.02, and -1.19 ± 0.01, respectively; within the error limits, these values do not differ from the slope in the R band. A deviation from the power-law decrease in flux occurs simultaneously in all of the bands at $t - t_0 \approx 0.05$ days. Closer to the end of our observations, a slightly larger decrease in flux was observed in the blue bands. Figure 2b shows the data from

the communication by Fitzgerald and Orosz (2003) at $t - t_0 > 0.7$ days. They roughly agree with the extension of the light curve measured with RTT150 at $t - t_0 < 0.6$ days.

A comparison of our data at $t - t_0 < 0.6$ days and the data from observatories in the western hemisphere at $t - t_0 > 0.6$ days (Fig. 2) shows that we were able to observe the beginning of a break in the power-law light curve of the afterglow. The change in the power-law slope occurs at $t - t_0 \approx 0.57$ days and lasts for about 0.2 days. Note that some (insignificant) decrease in the flux decline rate is observed in the RI bands before the beginning of this change, at $t - t_0 \approx 0.45$ days.

Before the beginning of our observations, the afterglow was observed with small telescopes without photometric filters (e.g., Rykoff and Smith 2003; Sato *et al.* 2003). Using these data for comparison with our data probably requires additional efforts to calibrate them. The power-law slope of the light curve at $t - t_0$ from 0.06 to 0.17 days (from 1.5 to 4 h), which was found from ROTSE data to be $\approx 1.1 \pm 0.1$ (Rykoff and Smith 2003), roughly agrees with our later measurements. A similar slope was also observed in the infrared (Nishihara *et al.* 2003). The power-law fading of the afterglow with a power-law slope of ≈ -1.2 probably began no later than one or two hours after the GRB.

VARIABILITY ON SHORT TIME SCALES

As we see from Fig. 2, apart from the smooth decrease in flux, no variability is observed on time scales of 100–1000 s. A detailed analysis of the nonperiodic variability of the light curve for the afterglow is beyond the scope of this paper and will be the subject of a separate paper. Note, however, that the rms deviation of the light curve from a uniform power-law decrease in flux is 1%. This value includes the contribution from the statistical and systematic errors and, thus, gives only a conservative upper limit on the intrinsic variability of the afterglow.

To check the variability on even shorter time scales of 0.1–10 s, we recorded the motion of the object over the field of view with the telescope drive switched off. The light curve can be reconstructed from the trail that it left on the CCD array with a resolution as high as about 0.1 s. In this case, an about 15-s-long segment of the light curve is recorded in one image. In this way, we recorded 20 images between 20:00 and 20:30 UT. One of these segments of the light curve is shown in Fig. 3. The rms deviation of the light curve from a uniform power-law decrease in flux is 10–3% on time scales of 0.1–10 s, respectively, which again gives a conservative upper limit on the variability of the source.

THE $BVRI$ SPECTRUM

As we see from Fig. 2, within the error limits, the colors of the afterglow did not change in the first five hours of our observations. The $BVRI$ spectral flux density corrected for Galactic extinction with $E(B - V) = 0.025$ (Schlegel *et al.* 1998) and referring to the beginning of our observations is shown in Fig. 4. The distribution closely corresponds to a power-law spectrum with an index $\alpha = 0.66 \pm 0.01$. This spectrum is flatter than the spectrum with a power-law slope $\alpha = 0.85$ obtained by Stanek *et al.* (2003) 2.6 days after the GRB.

Figure 5 shows how the radio, optical, and X-ray spectral radiation powers (νF_ν) are related. The RTT150 data are given at the time $t - t_0 = 0.25$ days (6 h). The second RXTE observation was carried out at exactly the same time (Marshall and Swank 2003). The RXTE X-ray fluxes and spectral slopes were taken from this communication, according to which the X-ray flux decreased at a rate of 20% per hour between $t - t_0 = 5$ and 6 h. This decrease roughly corresponds to a power law with a slope of -1, which is close to the slope that we observed in the optical range at this time.

We see from Fig. 5 that, at $t - t_0 = 0.25$ days, the peak of the spectral power is still approximately in the X-ray range. It is broad and also extends into the far-ultraviolet and, possibly, soft X-ray ranges. Figure 5 clearly shows that even the optical radiation power is only about half of the X-ray power.

The first radio observation was performed about 14 h after the GRB. The 8.46-GHz flux from the afterglow was 3.5 mJy (Berger *et al.* 2003). From 6 until 14 h after the GRB, the radio flux probably did not change by more than an order of magnitude. In addition, in general, the radio flux from GRB afterglows initially rises rather than falls, as in the optical and X-ray ranges. Such a behavior was also later observed for GRB 030329 (see, e.g., Pooley 2003). Thus, the radio flux was probably also five or six orders of magnitude lower than the optical and X-ray fluxes at $t - t_0 = 0.21$ days (5 h).

DISCUSSION

We presented the high-sensitivity measurement of the light curve for the optical afterglow of GRB 030329 that was carried out as early as several hours after the GRB. In all of the $BVRI$ bands, we observed a smooth decrease in flux, which was accurately described by a power law $F_\nu \propto t^{-1.19}$ in the first five hours of our observations. Subsequently, the flux decline rate increased compared to this law simultaneously in all of the spectral bands.

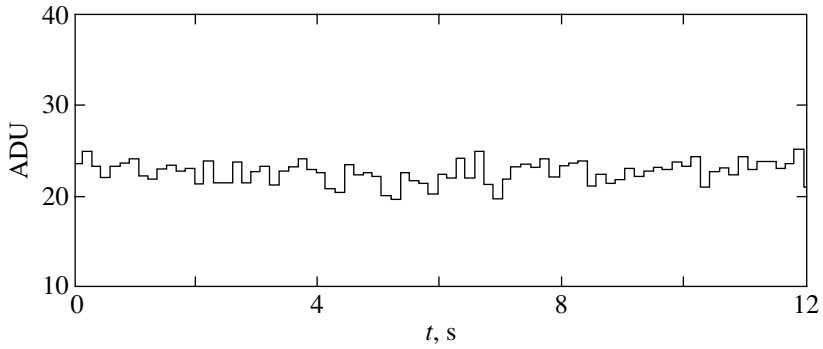

Fig. 3. A segment of the light curve for the afterglow taken with a high time resolution.

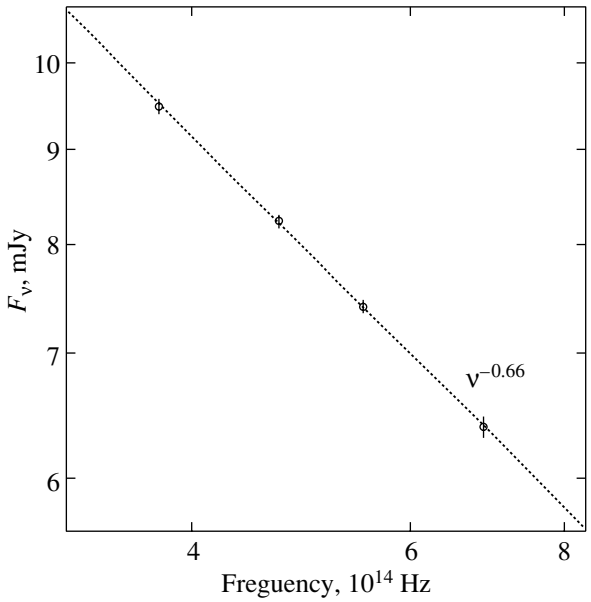

Fig. 4. The spectral flux density of the afterglow at the beginning of our observations at $t - t_0 = 0.25$ days (6 h) corrected for Galactic extinction with $E(B-V) = 0.025$ (Schlegel *et al.* 1998). This shape of the optical spectrum is exactly retained in the first five hours of our observations.

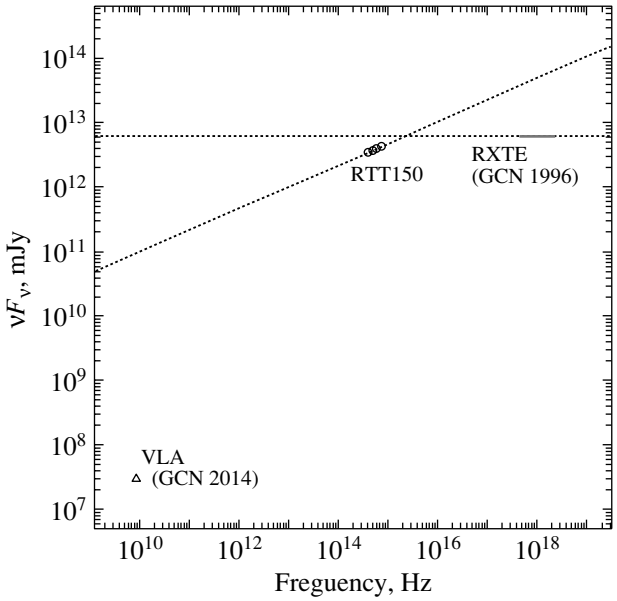

Fig. 5. The radio, optical, and X-ray spectral radiation powers. The RTT150 data are shown at the time $t - t_0 = 0.25$ days (6 h). The second RXTE observation was carried out at exactly the same time (Marshall and Swank 2003); its results are also shown in the figure. The radio fluxes were taken from the communication by Berger *et al.* (2003) and correspond to the time $t - t_0 = 0.58$ days (14 h).

The high signal-to-noise ratio during our observations allowed us to measure the afterglow flux with a much higher time resolution than previously. Apart from the smooth decrease in flux mentioned above, no flux variability is observed down to time scales of 0.1 s, within the error limits. The upper limits on the variability are 10, 3, and 1% on time scales of 0.1, 10, and 100–1000 s, respectively.

In general terms, our observations are consistent with the idea that the afterglow radiation is generated during the deceleration of an ultrarelativistic jet (see, e.g., Hurley *et al.* 2003). The break in the light curve observed at $t - t_0 = 0.57$ days may correspond to the moment that the gamma factor of the ultrarelativistic jet decreases to a value at which its structural features begin to show up in the observed light curve. This explanation is supported by the fact that this break is clearly observed in all of the color bands. In this case, the power-law slope changes from -1.19 to -1.9, i.e., roughly, as is commonly observed in such cases (Harrison *et al.* 1999). In addition, during the motion of the ultrarelativistic jet, there can be no variability on short time scales before this time, which we clearly observe. Variability appears just after this break (see GCN circulars).

For a homogeneous jet directed toward the observer, this can be the time the gamma factor becomes smaller than the reciprocal of the jet opening

angle θ^{-1}. In this case, using the formula and typical parameters from Frail *et al.* (2001), we can determine the opening angle, $\theta = 0.08$. The actual gamma-ray energy release corrected for directivity is $10^{52}\theta^2/2 = 3 \times 10^{49}$ erg. This value is approximately an order of magnitude lower than the typical value obtained by Frail *et al.* (2001) and comparable to the energy radiated during a supernova explosion.

The spectral shape of the afterglow at the beginning of our observations (Fig. 5) is roughly consistent with the assumption about the synchrotron nature of the radiation. In this case, there may be a characteristic electron-cooling frequency between the optical and X-ray ranges, and synchrotron self-absorption is probably observed in the radio range.

The observations of the optical afterglow from the cosmic GRB 030329 are currently being continued with RTT150. The results of these observations will be presented in our next papers.

ACKNOWLEDGMENTS

We wish to thank M.G. Revnivtsev for help in analyzing the RXTE data and S.Yu. Sazonov for a helpful discussion of the observations. This study was supported in part by the Russian Foundation for Basic Research (project nos. 02-02-16619, 03-02-06768, and 02-02-17342), the Program of State Support for Leading Scientific Schools (project no. 2083.2003.2), and the Program of the Presidium of the Russian Academy of Sciences "Nonstationary Phenomena in Astronomy." The study was also supported by the Workgroup on High-Energy Astrophysics of the Research Council of Turkey (TUBITAK) through support of Basic Research at Turkish Universities and the Turkish Academy of Sciences (for MAA).

REFERENCES

1. E. Berger, A. M. Soderberg, and D. A. Frail, GCN Circ. No. 2014 (2003).
2. H. E. Bond, IAU Circ. No. 6654 (1997).
3. R. Burenin, R. Sunyaev, M. Pavlinsky, *et al.*, GCN Circ. No. 2001 (2003); GCN Circ. No. 2024 (2003); GCN Circ. No. 2046 (2003); GCN Circ. No. 2051 (2003); GCN Circ. No. 2054 (2003); GCN Circ. No. 2079 (2003).
4. R. A. Burenin, A. A. Vikhlinin, O. V. Terekhov, *et al.*, Pis'ma Astron. Zh. **25**, 483 (1999) [Astron. Lett. **25**, 411 (1999)]; astro-ph/9902006.
5. E. Costa, M. Feroci, L. Piro, *et al.*, IAU Circ. No. 6649 (1997a).
6. E. Costa, F. Frontera, J. Heise, *et al.*, Nature **387**, 783 (1997b).
7. J. B. Fitzgerald and J. A. Orosz, GCN Circ. No. (2)056 (2003).
8. D. Frail, S. R. Kulkarni, R. Sari, *et al.*, Astrophys. J. **562**, L55 (2001).
9. P. Garnavich, K. Z. Stanek, and P. Berlind, GCN Circ. No. 2018 (2003).
10. S. Golenetskii, G. Grew, J. Doty, *et al.*, GCN Circ. No. 1997 (2003).
11. J. Greiner, M. Peimbert, C. Estaban, *et al.*, GCN Circ. No. 2020 (2003).
12. F. A. Harrison, J. S. Bloom, D. A. Frail, *et al.*, Astrophys. J. Lett. **523**, L121 (1999).
13. No. Henden, GCN Circ. No. (2)023 (2003); GCN Circ. 2082 (2003).
14. K. Hurley, R. Sari, and S. G. Djorgovski, astro-ph/0211620 (2002).
15. I. Khamitov, Z. Aslan, O. Golbasi, *et al.*, GCN Circ. No. 2094 (2003); GCN Circ. No. 2105 (2003); GCN Circ. No. 2108 (2003); GCN Circ. No. 2119 (2003).
16. A. Landolt, Astron. J. **104**, 340 (1992).
17. F. E. Marshall and J. H. Swank, GCN Circ. No. 1996 (2003).
18. E. Nishihara, O. Hashimoto, and K. Kinugasa, GCN Circ. No. 2118 (2003).
19. B. A. Peterson and P. A. Price, GCN Circ. No. 1985 (2003).
20. G. Pooley, GCN Circ. No. 2043 (2003).
21. E. S. Rykoff and D. A. Smith, GCN Circ. No. 1995 (2003).
22. R. Sato, Y. Yatsu, M. Suzuki, and N. Kawai, GCN Circ. No. 2080 (2003).
23. D. J. Schlegel, D. P. Finkbeiner, and M. Davis, Astrophys. J. **500**, 525 (1998).
24. V. V. Sokolov, Izv. Spets. Astrofiz. Obs. **51**, 38 (2001).
25. K. Z. Stanek, T. Matheson, P. M. Garnavich, *et al.*, Astrophys. J. (in press); astro-ph/0304173.
26. G. B. Taylor, D. A. Frail, S. R. Kulkarni, *et al.*, Astrophys. J. Lett. **502**, L115 (1998).
27. K. Torii, GCN Circ. No. 1986 (2003).
28. R. Vanderspek, G. Crew, J. Doty, *et al.*, GCN Circ. No. 1997 (2003).

Translated by V. Astakhov

Astronomy Letters, Vol. 29, No. 9, 2003, pp. 579–586. Translated from Pis'ma v Astronomicheskiĭ Zhurnal, Vol. 29, No. 9, 2003, pp. 656–663.

Optical and Radio Studies of Radio Sources

V. L. Afanasiev[1], S. N. Dodonov[1], A. V. Moiseev[1], V. Chavushyan[2], R. Mujica[2], Y. Juarez[2], A. G. Gorshkov[3*], V. K. Konnikova[3], and M. G. Mingaliev[1]

[1] *Special Astrophysical Observatory, Russian Academy of Sciences, Nizhnii Arkhyz, Karachai-Cherkessian Republic, 357147 Russia*

[2] *National Institute of Astrophysics, Optics, and Electronics, Puebla, Mexico*

[3] *Sternberg Astronomical Institute, Moscow State University, Universitetskii pr. 13, Moscow, 119992 Russia*

Received January 15, 2003

Abstract—We present the classification of optical identifications and radio spectra of six radio sources from a complete (in flux density) sample in the declination range 10° to 12°30′ (J2000.0). The observations were carried out with the 6-m Special Astrophysical Observatory telescope (Russia) in the wavelength range 3600–10 000 Å, the 2.1-m GHAO telescope (Mexico) in the range 4200–9000 Å, and the RATAN-600 radio telescope in the frequency range 0.97–21.7 GHz. Three of the six objects under study are classified as quasars, one is a BL Lac object, one is an absorption-line radio galaxy, and one is an emission-line radio galaxy. Five objects have flat radio spectra, and one object has a power-law radio spectrum. All of the radio sources identified as quasars or BL Lac objects show variable radio flux densities. The spectra of three objects were separated into extended and compact components. © *2003 MAIK "Nauka/Interperiodica"*.

Key words: *active galactic nuclei, quasars and radio galaxies, spectra.*

INTRODUCTION

In this paper, we classify the optical objects that were associated with radio sources from a complete (in flux density) sample. The sample contains 154 sources with flux densities from the GB6 catalog (Gregory *et al.* 1996) $S_{4.85} > 200$ mJy in the ranges of declinations 10° to 12°30′ (J2000.0) and right ascensions 0 to 24^h and $|b| > 15°$; it has been observed with the RATAN-600 radio telescope since 2000 (Gorshkov *et al.* 2000). One of the goals of studying this sample is to detect the cosmological evolution of quasars. For this purpose, it is necessary to determine the redshifts for most of the objects identified with the radio sources under study. We identified 86% of the sample sources with flat spectra and 60% of the sample sources with normal spectra with optical objects. A large number of identified objects were classified previously; the remaining objects are classified by using the 2.1-m G. Haro Observatory (GHAO) telescope of the National Institute of Astrophysics, Optics, and Electronics (INAOE) in Cananea (Mexico) (Chavushyan *et al.* 2000, 2001, 2002) and the 6-m (BTA) Special Astrophysical Observatory (SAO) telescope of the Russian Academy of Sciences in Nizhnii Arkhyz (Russia) (Afanasiev *et al.* 2003). The redshifts (for some of the BL Lac objects, only the classification is available) of 64 objects with flat spectra and 32 objects with normal spectra are known to date.

OPTICAL AND RADIO OBSERVATIONS

We obtained the spectra of the objects with the 6-m BTA telescope on February 6–8, 2002. We used the SCORPIO spectrograph (http://www.sao.ru/moisav/scorpio/scorpio.html) in the long-slit mode and a 1024 × 1024 pixel TK1024 CCD detector with a readout noise of $3e^-$. The covered spectral range was 3600–10000 Å with a dispersion of 6 Å per pixel. The effective instrumental resolution was about 20 Å. We reduced the spectra in a standard way by using the software developed at the Laboratory of Spectroscopy and Photometry of the SAO.

We obtained the spectra of the objects with the 2.1-m GHAO telescope on March 8, 2002. In our observations, we used the LFOSC spectrophotometer equipped with a 600 × 400-pixel CCD array (Zickgraf *et al.* 1997); the detector readout noise was $8e^-$, and the covered spectral range was 4200–9000 Å with a dispersion of 8.2 Å per pixel. The effective instrumental spectral resolution was about 16 Å. The reduction of our observations was performed with the IRAF package and included cosmic-ray hit removal,

*E-mail: algor@sai.msu.ru

Table 1. Coordinates and magnitudes of the objects

Object name	Radio coordinates, J2000.0		Optical–radio		Magnitude	
	α	δ	$\Delta\alpha$	$\Delta\delta$	R	B
0946 + 1017	$09^h46^m35\overset{s}{.}069$	+10°17′06″.13	$0\overset{s}{.}011$	−0″.15	18.7	18.7
1015 + 1227	10 15 44.024	+12 27 07.07	−0.001	0.19	18.2	19.2
1103 + 1158	11 03 03.530	+11 58 16.61	0.005	−0.10	18.4	18.9
1207 + 1211	12 07 12.625	+12 11 45.88	0.008	0.05	18.9	19.0
1306 + 1113	13 06 19.248	+11 13 39.79	0.015	−0.01	13.0	15.4
1315 + 1220	13 15 01.853	+12 20 52.63	0.062	0.10	17.8	18.7

flat fielding, wavelength linearization, and flux calibration.

The radio observations of the sources were carried out with the Northern Sector of RATAN-600 in 2000–2002 at frequencies of 0.97, 2.3, 3.9, 7.7, 11.1, and 21.7 GHz in a fixed-focus mode (Soboleva *et al.* 1986). The observing and reduction techniques were described by Botashev *et al.* (1999). The parameters of the RATAN-600 receivers used for the Northern Sector are presented in Berlin *et al.* (1997). The beam width changed from 11″ to 235″ in right ascension and from 1′.4 to 30′ in declination at frequencies from 21.7 GHz to 0.97 GHz. To calibrate the flux densities of the sources, we used the radio source 1347+1217 with a constant flux density, which is a point source for our beams at all frequencies. The adopted flux densities of the calibration source at frequencies 0.97–21.7 GHz are 6.15, 4.12, 3.23, 2.36, 1.99, and 1.46 Jy, respectively. The procedure for separating the radio spectra of the sources into extended and compact components was described by Gorshkov *et al.* (2000).

RADIO AND OPTICAL COORDINATES OF THE OBJECTS

Table 1 gives the radio coordinates of the program objects for the epoch J2000.0, the differences between their optical and radio coordinates in right ascension and declination, and their R and B magnitudes. The source names are composed of hours and minutes of right ascension and degrees and arcminutes of declination. For our identifications of the radio sources with optical objects, we used the coordinates from the JVAS[1] catalog at a frequency of 8.4 GHz (Wrobel *et al.* 1998); the rms error of the coordinates in right ascension and declination is 0.014 arcseconds. The optical coordinates and magnitudes were taken from the USNO Astrometric Survey (Monet *et al.* 1996).

[1] JVAS is the Jodrell Bank–VLA Astrometric Survey.

RESULTS

The spectra of the objects taken with the 2.1-m telescope in Mexico and the 6-m BTA telescope are shown in Figs. 1 and 2, respectively. Figure 3 shows the radio spectra of the sources. Table 2 presents the optical observations. Table 3 contains the flux densities of the radio sources and their rms errors in the frequency range 0.97–21.7 GHz. The last column gives the epochs of our observations.

Below we give remarks on each of the program objects. In all of the formulas that fit the spectra, the frequencies are in GHz and the flux densities are in mJy.

The source 0946+1017. The optical spectrum taken with the 2.1-m telescope (Fig. 1a) exhibits one strong line identified with the MgII 2798 Å line at the redshift $z = 0.999$. Two lines, MgII 2798 Å and CIII] 1909 Å were identified in the spectrum taken with the 6-m telescope (Fig. 2a). The redshift determined from these lines is $z = 1.007$. This object is a quasar with the mean redshift $z = 1.004$.

The source was observed with RATAN-600 twice, in 2000 and 2001. Using the Texas survey data at a frequency of 0.365 GHz (Douglas *et al.* 1996), we can separate a power-law component from the spectra with $S = 200\nu^{-0.85}$ mJy. After the subtraction of the power-law component, the spectrum of the compact component for the epoch 09.2000 can be fitted by the logarithmic parabola $\log S = 2.202 + 0.765\log\nu - 0.497\log^2\nu$. The spectrum has a peak at a frequency of 5.9 GHz, with a peak flux density of 313 mJy. In Fig. 3a, the original spectrum and the spectra of the compact and power-law components are indicated by crosses and solid and dashed lines, respectively. The spectrum of the compact component after the subtraction of the power-law component from the data for the epoch 07.2001 can be fitted by the logarithmic parabola $\log S = 2.237 + 0.616\log\nu - 0.483\log^2\nu$; the peak in the spectrum

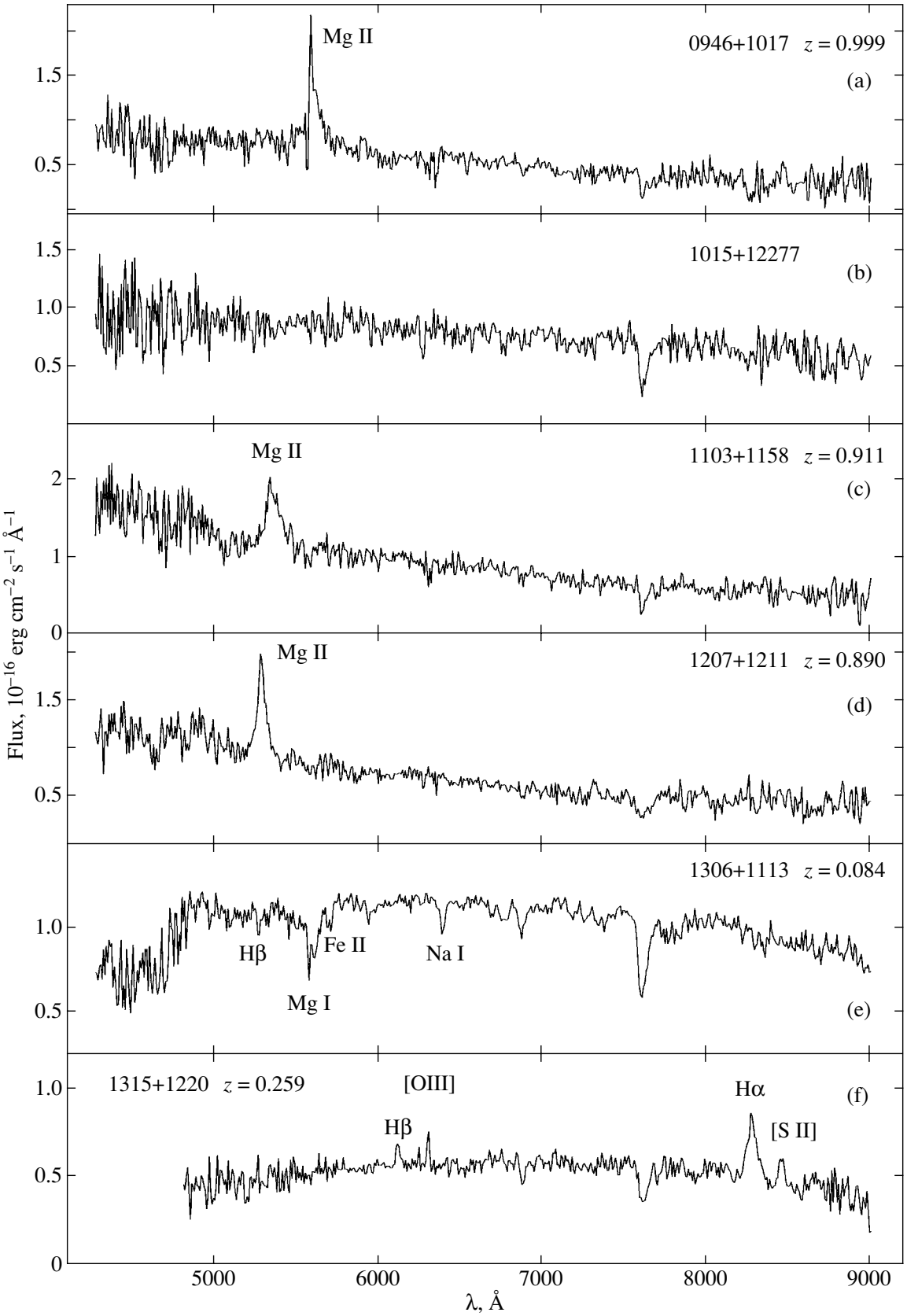

Fig. 1. The optical spectra of the objects taken with the 2.1-m telescope (Mexico).

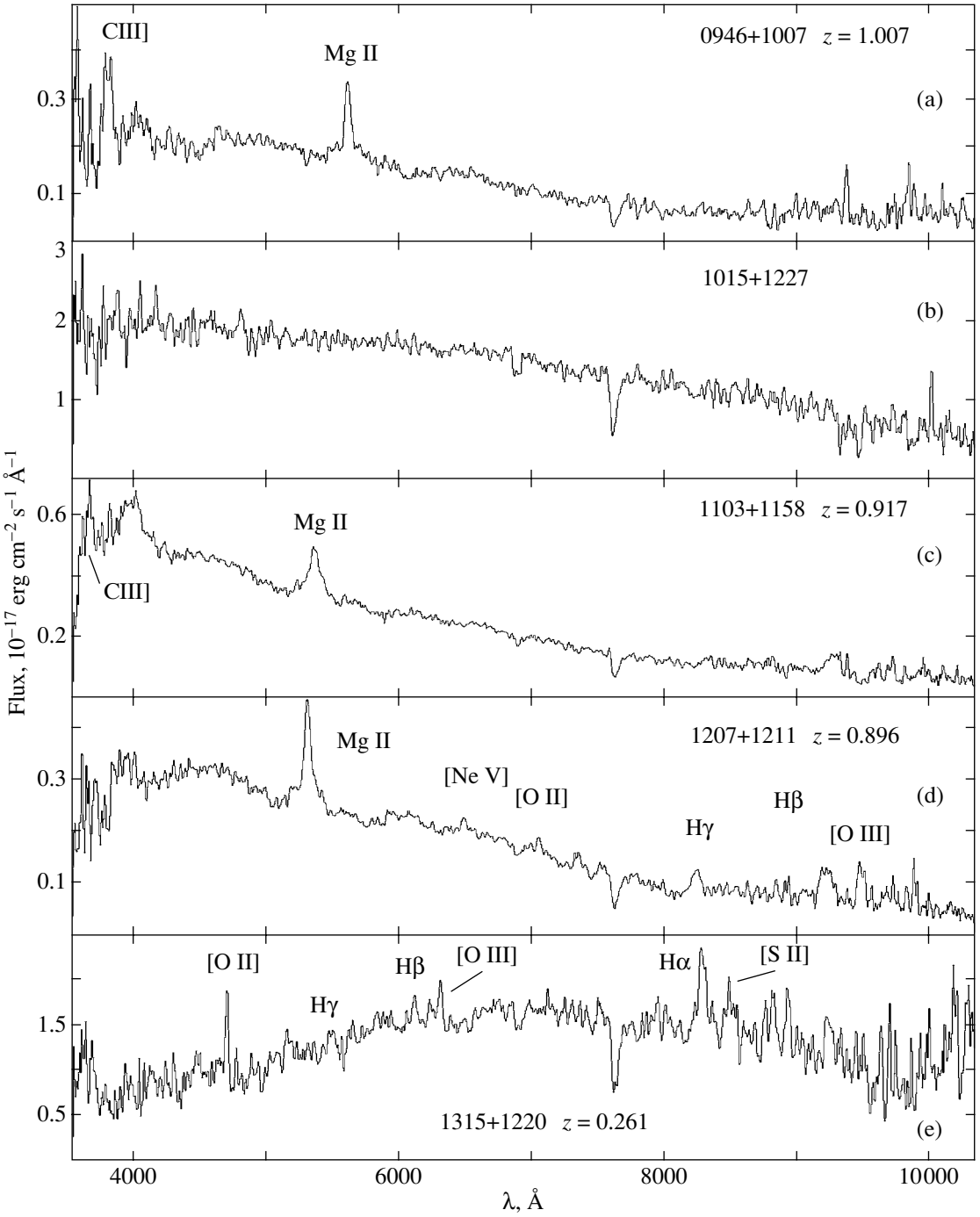

Fig. 2. The optical spectra of the objects taken with the 6-m BTA telescope (Russia).

shifted to a frequency of 4.3 GHz. In this source, we are most likely observing the development of an outburst.

The source 1015+1227. Since both optical spectra (Figs. 1b and 2b) contain no lines, we classified this source as a BL Lac object.

We observed the source with RATAN-600 three times, in 2000–2002. All of the spectra obtained rise toward higher frequencies. Figure 3b shows the spectra for the epochs 09.2000 (upper spectrum) and 06.2002 after the subtraction of a small power-law component with $S = 45\nu^{-0.8}$ mJy from the original spectra. The spectrum taken at the epoch 07.2001 (Gorshkov *et al.* 2002) is located between the shown spectra. The flux densities at frequencies of 0.97–2.3 GHz were constant within the limits of the mea-

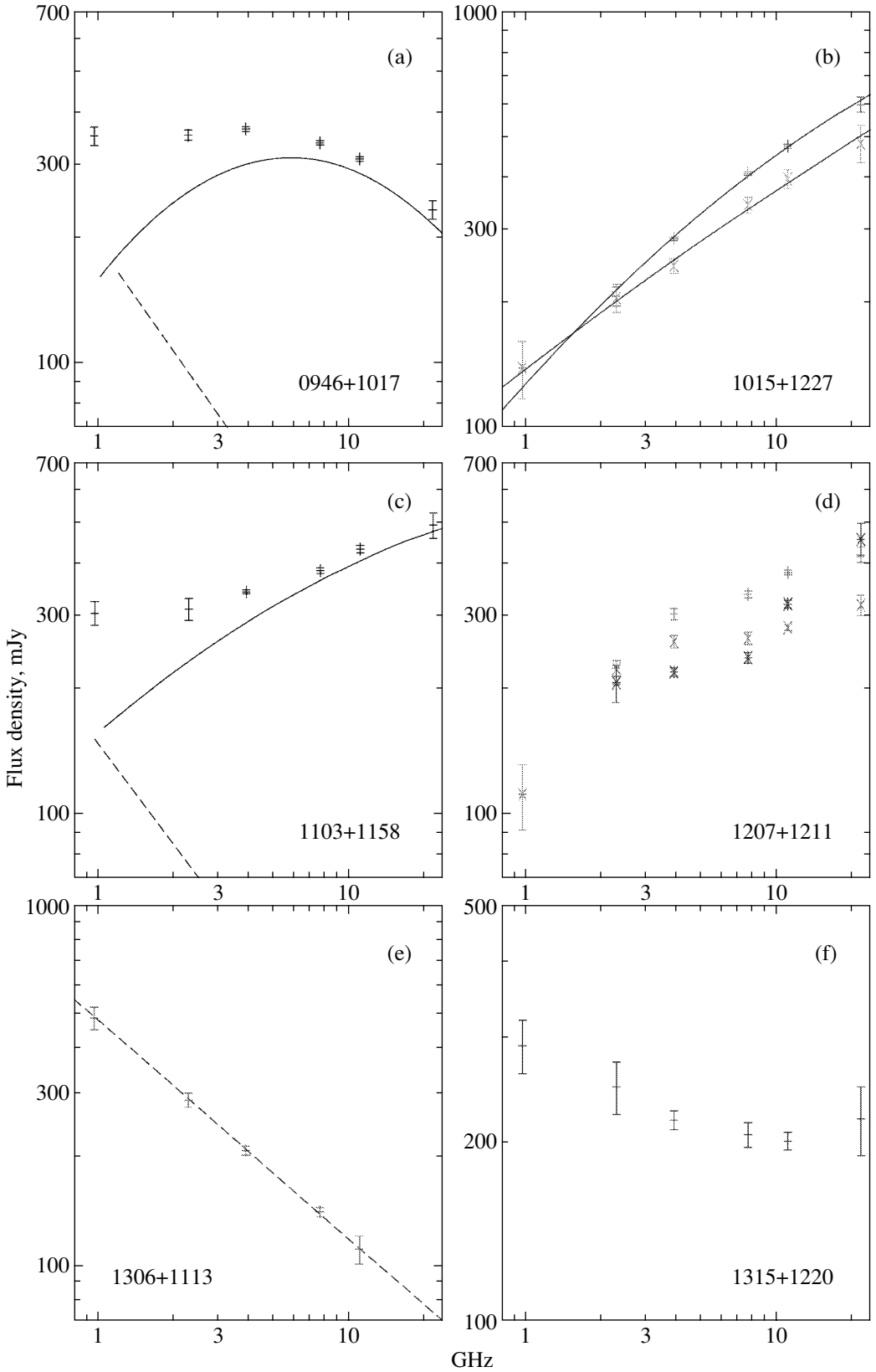

Fig. 3. The radio spectra of the sources. The spectra of the sources 0946+1017 and 1103+1158 (a, c) were separated into components: the original spectra are indicated by crosses, the spectra of the extended components are indicated by dashed lines, and the spectra of the compact components are indicated by solid lines. The spectrum of the source 1207+1211 (d) is indicated by pluses, crosses, and asterisks for the epochs 09.2000, 07.2001, and 06.2002, respectively.

Table 2. Optical observations

Object name	Spectral lines	Wavelengths, in rest frame and observed, Å	z	Object type	Date of observation	Exposure time, min	Telescope	$\bar{z}$
0946+1017	CIII]	1909/3830	1.007	QSO	Feb. 7, 2002	10	BTA	
	MgII	2798/5615						1.004
	MgII	2798/5592	0.999	QSO	Mar. 8, 2002	90	GHAO	
1015+1227				Lac	Feb. 7, 2002	20	BTA	
				Lac	Mar. 8, 2002	60	GHAO	
1103+1158	CIII]	1909/3660	0.917	QSO	Feb. 8, 2002	20	BTA	
	MgII	2798/5364						0.915
	MgII	2798/5346	0.911	QSO	Mar. 8, 2002	60	GHAO	
1207+1211	MgII	2798/5300	0.896	QSO	Feb. 8, 2002	20	BTA	
	[NeV]	3426/6495						0.895
	[OII]	3727/7065						
	Hγ	4340/8230						
	Hβ	4861/9220						
	[OIII]	5007/9490						
	MgII	2798/5288	0.890	QSO	Mar. 8, 2002	30	GHAO	
1306+1113	Hβ	4861/5269	0.084	Abs.G	Mar. 8, 2002	30	GHAO	
	MgI	5175/5610						0.084
	FeII	5270/5706						
	NaI	5896/6396						
1315+1220	[OII]	3727/4700	0.261	Em.G	Feb. 6, 2002	20	BTA	
	Hγ	4340/5473						0.260
	Hβ	4861/6130						
	[OIII]	5007/6310						
	Hα	6563/8280						
	[SII]	6724/8480						
	Hβ	4861/6120	0.259	Em.G	Mar. 8, 2002	90	GHAO	
	[OIII]	4959/6249						
	[OIII]	5007/6306						
	Hα	6563/8272						
	[SII]	6724/8455						

surement errors; the largest change in flux density, from 490 ± 44 to 605 ± 25 mJy, was recorded at a frequency of 21.7 GHz.

The spectra of the compact components shown in Fig. 3b were fitted by the logarithmic parabolas $\log S = 2.110 + 0.670 \log \nu - 0.120 \log^2 \nu$ (09.2000) and $\log S = 2.103 + 0.573 \log \nu - 0.098 \log^2 \nu$ (06.2002). We see all of the spectra in an optically thick region; the flux density peaks at frequencies much higher than the range under study.

The source 1103+1158. The optical spectra shown in Figs. 1c and 2c exhibit a broad emission

Table 3. Radio observations

Object name	Flux densities and errors, mJy						Epoch
	0.97 GHz	2.3 GHz	3.9 GHz	7.7 GHz	11.1 GHz	21.7 GHz	
0946+1017	353 18	355 10	367 05	340 04	311 04	235 12	09.2000
	358 20	352 10	338 04	280 03	250 03	181 16	07.2001
1015+1227	185 20	231 11	302 03	420 04	483 05	605 25	09.2000
		230 26	263 07	354 15	406 21	490 44	06.2002
1103+1158	310 21	305 15	312 05	350 04	396 07	490 17	09.2000
	305 20	293 07	320 04	345 06	388 05	474 20	07.2001
		312 19	343 04	386 06	434 09	496 35	06.2002
1207+1211	112 19	215 10	303 09	338 07	381 05	420 16	09.2000
	112 20	224 10	260 09	265 09	281 05	318 18	07.2001
		207 21	220 05	238 07	320 07	458 42	06.2002
1306+1113	498 35	290 13	210 06	142 04	112 10		11.2001
1315+1220	298 20	245 18	219 08	205 10	210 07	215 20	06.2001

line identified with MgII 2798 Å. The line width is FWHM $\approx$ 90 Å. The CIII] 1909 Å line was additionally identified in the BTA spectrum. We measured the redshift from these lines, $z = 0.915$. The object is a quasar.

We observed the object with RATAN-600 three times, in 09.2000, 07.2001, and 06.2002. A power-law component of the source's extended part with $S = 180\nu^{-0.78}$ mJy was separated from the original spectra. After the subtraction of the power-law component, the spectrum of the compact component in the frequency range 0.97–21.7 GHz can be fitted by the parabolas $\log S = 2.151 + 0.433\log\nu - 0.035\log^2\nu$ (09.2000), $\log S = 2.128 + 0.509\log\nu - 0.092\log^2\nu$ (07.2001), and $\log S = 2.135 + 0.618\log\nu - 0.161\log^2\nu$ (06.2002). The peak in these spectra successively shifted toward lower frequencies; the development of an outburst is observed. We observed all of the spectra of the compact components in an optically thick region. Figure 3c shows the original spectrum of the source for the epoch 06.2002 (crosses), the spectrum of the extended component (dashed line), and the spectrum of the compact component (solid line).

The source 1207+1211. One strong emission line that was identified as MgII 2798 Å at the redshift $z = 0.890$ can be identified in the object's optical spectrum taken with the 2.1-m telescope (Fig. 1d). The line width is FWHM $\approx$ 55 Å. In addition to the magnesium line, five more weaker lines can be identified in the BTA spectrum (Fig. 2d): [NeV] 3426 Å, [OII] 3727 Å, Hγ 4340 Å, Hβ 4861 Å, and [OIII] 5007 Å. The object's redshift was estimated from all of these lines to be $z = 0.896$. We classify the object as a quasar with the mean redshift $z = 0.895$.

We observed the source with RATAN-600 in 09.2000, 07.2001, and 06.2002. Figure 3d shows the source's spectra for these epochs. The source has a variable flux density. All of the spectra are complex and are poorly fitted by logarithmic parabolas. Several outbursts probably occur simultaneously in this source. The extended component is weak in the frequency range under consideration. The largest change in flux density, from 318 ± 18 to 458 ± 42 mJy, was observed at a frequency of 21.7 GHz.

The source 1306+1113. We identified the Hβ 4861 Å, MgI 5175 Å, FeII 5270 Å, and NaI 5896 Å absorption lines in the source's optical spectrum taken with the 2.1-m telescope (Fig. 1e). The redshift was estimated from all of these lines to be $z = 0.084$. The object is an absorption-line elliptical galaxy.

The radio source has a power-law spectrum in the frequency range 0.97–11.2 GHz: $S = 484\nu^{-0.606}$ mJy (Fig. 3e).

The source 1315+1220. Five emission lines classified as two hydrogen lines (Hα 6563 Å and Hβ 4861 Å), two forbidden oxygen lines ([OIII] 4959 Å and 5007 Å), and one forbidden silicon line ([SII] 6724 Å) can be identified in the object's optical spectrum obtained with the 2.1-m telescope (Fig. 1f). In addition to these lines, a strong [OII] 3727 Å

line and the Hγ 4340 Å line can be identified in the BTA spectrum (Fig. 2e). We classify this object as an emission-line galaxy. The object's redshift was estimated from all of these lines to be $z = 0.260$.

The source was observed with RATAN-600 in 09.2000 and 06.2001. Within the limits of the measurement errors, the flux density was constant at all frequencies. The spectrum is shown in Fig. 3f. The flattening of the spectrum toward higher frequencies is probably caused by the compact component, but we cannot separate the components in terms of the model under consideration.

CONCLUSIONS

Three of the six objects under study were classified as quasars with similar redshifts, 0.895, 0.915, and 1.004; one object exhibits no lines in its optical spectra, and we classified it as a BL Lac object. All of these objects show variable radio flux densities. The spectra of the objects 0946+1017, 1015+1227, and 1103+1158 were separated into two components: an extended component with a power-law spectrum and a compact component fitted by a logarithmic parabola. In the source 1207+1211, the extended component is weak in the frequency range under consideration.

We classified one object as an absorption-line galaxy with a redshift of 0.084 and a power-law radio spectrum and one object as an emission-line galaxy with the redshift $z = 0.260$ whose radio spectrum flattens toward higher frequencies.

ACKNOWLEDGMENTS

We wish to thank the staff of the Guillermo Haro Observatory for kind support during the observations. This study was supported in part by the Russian Foundation for Basic Research (project no. 01-02-16331), the "Universities of Russia" Program (project UR.02.03.005), the State Science and Technology Program "Astronomy" (project no. 1.2.5.1), and the CONACYT (grant nos. 28499-E and J32178-E).

REFERENCES

1. V. L. Afanasiev, S. N. Dodonov, A. V. Moiseev, *et al.*, Astron. Zh. **80**, 499 (2003) [Astron. Rep. **47**, 458 (2003)].
2. A. B. Berlin, A. A. Maksyasheva, N. A. Nizhel'skiĭ, *et al.*, *Proceedings of the XXVII Radioastronomical Conference, St.-Petersburg* **3**, 115 (1997).
3. A. M. Botashov, A. G. Gorshkov, V. K. Konnikova, and M. G. Mingaliev, Astron. Zh. **76**, 723 (1999) [Astron. Rep. **43**, 631 (1999)].
4. V. Chavushyan, R. Mujika, A. G. Gorshkov, *et al.*, Pis'ma Astron. Zh. **26**, 403 (2000) [Astron. Lett. **26**, 339 (2000)].
5. V. Chavushyan, R. Mujika, A. G. Gorshkov, *et al.*, Astron. Zh. **78**, 99 (2001) [Astron. Rep. **45**, 79 (2001)].
6. V. Chavushyan, R. Mujika, Kh. R. Valdes, *et al.*, Astron. Zh. **79**, 771 (2002) [Astron. Rep. **46**, 697 (2002)].
7. J. N. Douglas, F. N. Bash, F. Bozyan, *et al.*, Astron. J. **111**, 1945 (1996).
8. A. G. Gorshkov, V. K. Konnikova, and M. G. Mingaliev, Astron. Zh. **77**, 407 (2000) [Astron. Rep. **44**, 353 (2000)].
9. A. G. Gorshkov, V. K. Konnikova, and M. G. Mingaliev, Preprint No. 175, Spec. Astrophys. Obs. (Nizhniĭ Arkhyz, 2002).
10. P. C. Gregory, W. K. Scott, K. Douglas, and J. J. Condon, Astrophys. J., Suppl. Ser. **103**, 427 (1996).
11. D. Monet, A. Bird, B. Canzian, *et al.*, *USNO-SA1.0* (U. S. Naval Obs., Washington, 1996).
12. N. S. Soboleva, A. V. Temirova, and T. V. Pyatunina, Preprint No. 32, Spec. Astrophys. Obs. (Nizhniĭ Arkhyz, 1986).
13. J. M. Wrobel, A. R. Patnaik, I. W. A. Browne, and P. N. Wilkinson, Astron. Astrophys., Suppl. Ser. **193**, 4004 (1998).
14. F. J. Zickgraf, I. Thiering, J. Krautter, *et al.*, Astron. Astrophys., Suppl. Ser. **123**, 103 (1997).

Translated by N. Samus'

Astronomy Letters, Vol. 29, No. 9, 2003, pp. 587–593. Translated from Pis'ma v Astronomicheskiĭ Zhurnal, Vol. 29, No. 9, 2003, pp. 664–671.

IGR J16318–4848: An X-ray Source in a Dense Envelope?

M. G. Revnivtsev[1,2*], S. Yu. Sazonov[1,2], M. R. Gilfanov[1,2], and R. A. Sunyaev[1,2]

[1] *Max-Planck Institut für Astrophysik, Karl Schwarzschild Strasse 1, 86740 Garching-bei-München, Germany*

[2] *Space Research Institute, Russian Academy of Sciences, Profsoyuznaya ul. 84/32, Moscow, 117810 Russia*

Received March 20, 2003

Abstract—We analyze in detail the ASCA observations of the hard X-ray source IGR J16318–4848, which was recently discovered by the INTEGRAL observatory (Courvoisier *et al.* 2003). The source has an anomalously hard spectrum in the energy range 0.5–10 keV and is virtually undetectable below 4 keV because of strong photoabsorption ($n_H L > 4 \times 10^{23}$ cm^{-2}). The $K\alpha$ line of neutral or weakly ionized iron with an equivalent width of ~2.5 keV dominates in the energy range 4–10 keV. There is also evidence for the presence of a second line at energy ~7 keV. Our analysis of archival observational data for the infrared counterpart of IGR J16318–4848 that was discovered by Foschini *et al.* (2003) revealed the source in the wavelength range 1–15 μm. Available data suggest that the object can be an X-ray binary system surrounded by a dense envelope. The source may be a high-mass X-ray binary similar to GX 301-2. We believe that IGR J16318–4848 can be the first representative of a hitherto unknown population of strongly absorbed Galactic X-ray sources that could not be detected by previous X-ray observatories.

Key words: *X-ray and gamma-ray sources; IGR J16318–4848.*

INTRODUCTION

INTEGRAL, a powerful X-ray and gamma-ray observatory placed into orbit,[1] can discover a new population of strongly absorbed sources at energies $\lesssim$10 keV that could go unnoticed by previous observatories.

The absence of any X-ray sources in rich molecular clouds, where intense star formation is going on and high-mass binary systems must exist in principle, has been a puzzle to X-ray astronomy for many years. Another reason why we may expect the existence of X-ray sources in molecular clouds is that numerous single and binary neutron stars (~10^9 per galaxy) and black holes (~10^7–10^8 per galaxy) can pass through these clouds. Simple estimates based on Bondi's formula indicate that such an object can strongly brighten through the accretion of the surrounding molecular cloud. However, the large optical depth of massive molecular clouds for absorption can strongly attenuate the emergent X-ray emission and make such sources virtually unobservable for soft and standard X-ray telescopes, as well as for all-sky monitors, most of which also operate in the standard X-ray range.

On the other hand, theorists widely discuss the possibility of strongly super-Eddington accretion. Two accretion scenarios are currently being considered in this case: the formation of a geometrically and optically thick accretion disk that carries away trapped radiation into a black hole (Abramowicz *et al.* 1988) and the emergence of a strong mass outflow from an accreting black hole or neutron star (Shakura and Sunyaev 1973). SS 433-type binary systems may manifest themselves precisely in this way at a certain stage, and it is this regime that we observed during an outburst of V4641 Sgr, where a dense absorbing atmosphere formed around the accreting object (Revnivtsev *et al.* 2002).

X-ray binaries (including pulsars) surrounded by a dense wind that outflows from the surface of the donor star constitute another possible class of objects that were unobservable by previous observatories. Because of photoabsorption in such an envelope, the X-ray source can be virtually invisible for an external observer at energies below 5 keV. Moreover, in extreme cases, the envelope can be optically thick even for Compton scattering. As a result, the initially hard X-ray photons will lose their energy during multiple scatterings and a spectrum with the peak at energies 10–20 keV will be formed.

The discovery (Courvoisier *et al.* 2003) of the strongly absorbed X-ray source IGR J16318–4848

* E-mail: mikej@hea.iki.rssi.ru

[1] http://astro.estec.esa.nl/SA-general/Projects/Integral/integral.html

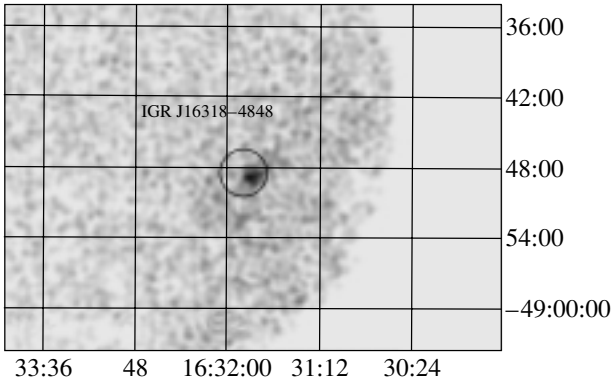

Fig. 1. The ASCA image of the sky region around IGR J16318–4848.

by the INTEGRAL orbital X-ray observatory is significant. Because of its high sensitivity at energies above 15 keV, INTEGRAL is capable of discovering relatively weak, strongly absorbed X-ray sources of the types mentioned above.

The INTEGRAL observatory spends much of its time scanning the Galactic plane. A hitherto unknown source that was called IGR J16318–4848 was discovered during one such observation on January 29, 2003. The position of the source was determined from IBIS (the operating energy range 15 keV–10 MeV) data: $\alpha = 16^{\rm h}31^{\rm m}52^{\rm s}$ and $\delta = -48^\circ48'5''$ (epoch 2000, $2'$ uncertainty; Courvoisier *et al.* 2003). The 15- to 40-keV flux from the source was recorded at a level of 50–100 mCrab and was variable on time scales of hours.

Analysis of archival ASCA observations (September 3, 1994) of this sky region revealed a weak X-ray source at the position that coincided with the position of IGR J16318–4848 determined by INTEGRAL (Murakami *et al.* 2003). The authors pointed out the presence of strong absorption in the source's spectrum and the possible presence of an iron line at energy 6.4 keV. The XMM observations that followed the discovery of the transient confirmed the presence of two strong emission lines at energies ~6.4 and ~7 keV (Schartel *et al.* 2003; de Plaa *et al.* 2003). Analysis of archival observations of the source's region revealed an infrared counterpart with the coordinates $\alpha = 16^{\rm h}31^{\rm m}48^{\rm s}$ and $\delta = -48^\circ49'01''$ (epoch 2000, $0.2''$ uncertainty; Foschini *et al.* 2003).

In this paper, we present the results of such an analysis of the ASCA observations for IGR J16318–4848. Based on all of the currently available observations of the source in various energy ranges, some of which are published here for the first time, we discuss the possible nature of the object.

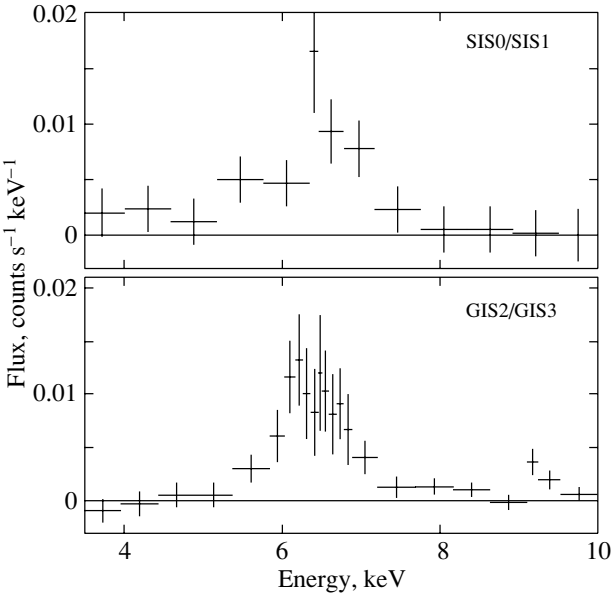

Fig. 2. The spectra of IGR J16318–4848, as constructed from GIS and SIS 3.5- to 10-keV data. Background #2 was used to construct these spectra, which reduced the statistical significance of the spectral points (cf. Fig. 3).

ANALYSIS OF ASCA OBSERVATIONS

The region of the sky around IGR J16318–4848 was observed by ASCA (Tanaka *et al.* 1994) on September 3, 1994, at 4:11–7:11 UT. The exposure time was ~4 ks. For our analysis, we used data from all of the ASCA instruments—the GIS gas counters and the SIS solid-state spectrometers. The standard LHEASOFT 5.2 software package was used to analyze the data. For spectral fitting, we used the XSPEC package. To avoid biased estimates of the best-fit parameters for the source's spectrum at a small number of recorded counts, we used the method of estimating the uncertainties of observed spectral points that was described by Churazov *et al.* (1996).

There is substantial stray light from the relatively bright nearby source 4U1624–49 on the detectors; its 2- to 10-keV flux is about 50 mCrab, and its distance from the field center is ~50′. Therefore, apart from the standard determination of the background from the observations of empty fields (background #1), we also estimated the background from the observation being analyzed by using an annular region with an inner radius of $4'$ and an outer radius of $8'$ (background #2). In the latter case, the statistical significance of the source's spectrum considerably decreases, because the uncertainty in the background estimate begins to have an effect due to the short exposure time.

The GIS image smoothed with a $0.5'$-wide Gaussian is shown in Fig. 1. The circle indicates the

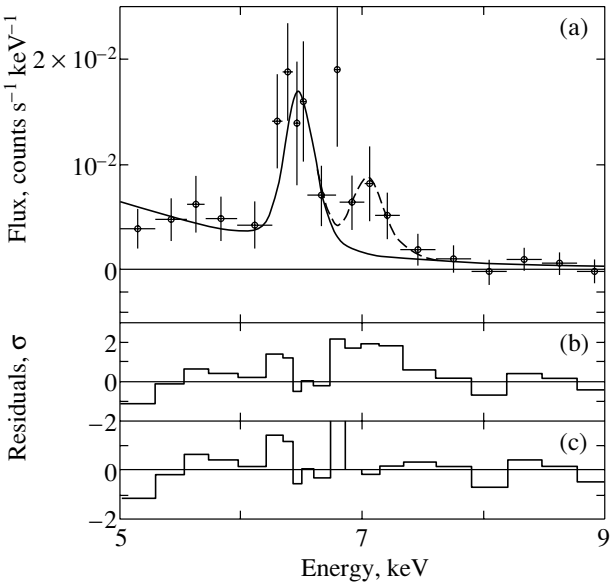

Fig. 3. (a) The spectrum of IGR J16318−4848, as constructed from SIS0 and SIS1 data. The solid and dashed curves represent the fits to the observed spectrum using the models with one and two emission lines, respectively. The difference between the observed spectrum and the spectrum for the models with only one line at ∼6.4 keV (b) and two lines (c).

Best-fit parameters for the spectrum of IGR J16318−4848, as derived from ASCA data

Parameter	Value
Line centroid E_1, keV	$6.46 \pm 0.02^{a} \pm 0.06^{b}$
Line width σ_1, keV	<0.2
Equivalent width EW_1, keV	2.5 ± 0.5
Line flux F_1, 10^{-4} phot. cm^{-2} s^{-1}	9.0 ± 2.1
Line centroid E_2, keV	7.05^{c}
Line width σ_2, keV	0.0^{c}
Equivalent width EW_2, keV	2.0 ± 0.6
Line flux F_2, 10^{-4} phot. cm^{-2} s^{-1}	3.7 ± 1.6
Photon index	1.0^{c}
$n_H L$, 10^{22} cm^{-2}	94 ± 35
Flux (2−10 keV), 10^{-11} erg s^{-1} cm^{-2}	1.2 ± 0.2
χ^2/d.o.f.	557.9/882

[a] Statistical error.
[b] Systematic error.
[c] The index was fixed at the given value.

INTEGRAL error region of the X-ray transient IGR J16318−4848. We clearly see a weak source within the error region of IGR J16318−4848. Its coordinates are $\alpha = 16^{h}31^{s}49^{m}$, $\delta = -48°49'.2$ (epoch 2000, $0'.8$ uncertainty; Murakami *et al.* 2003).

We used background #2 to study the broadband (0.5−10 keV) spectrum, because the effect of stray light on the detector becomes strong at low energies. Figure 2 shows the GIS and SIS spectra of IGR J16318−4848. We see a strong line in the spectrum near 6.4 keV and that the source is virtually undetectable at energies below ∼4 keV.

Let us first consider the region of the iron line (5−9 keV). The SIS data are best suited to this purpose as having a higher spectral resolution. In addition, the effect of stray light in this energy range is negligible and we can use background #1 to make the most of the observational statistics.

To fit the 5- to 9-keV spectrum of the source (see Fig. 3), we used a power-law energy dependence of the photon flux ($dF(E) \propto E^{-\alpha}dE$) together with a Gaussian at energy ∼6.4 keV (the $K\alpha$ line of neutral iron). Since our spectrum has a low statistical significance and we are working in a narrow spectral range (5−9 keV), the photon index α is of no importance in the model. In our fit, we fixed the parameter $\alpha = 1.0$. The χ^2 fitting (with specially determined weights in the spectral channels; see Churazov *et al.* (1996) for a description of the χ^2 method) yields a satisfactory value of $\chi^2 = 185.9$ (339 degrees of freedom). However, we see statistically significant deviations from the model in the spectrum near ∼7 keV, which may suggest the presence of an additional emission line in the spectrum. Including the $K\beta$ line of neutral iron with the centroid at 7 keV and a zero width in the model leads to an improvement in the χ^2 value by $\Delta\chi^2 \sim 12$, while the number of degrees of freedom per unit decreases. Statistically, this change in χ^2 implies that introducing the additional parameter is justified at a probability of $\sim 10^{-5}$.

Thus, we may assert with confidence that two lines, at energies $6.46 \pm 0.02(\pm 0.06)$ and 7.05 keV (the value in parentheses indicates the systematic error in the detector energy scale), are present in the source's spectrum. The equivalent widths of these lines are 2.5 ± 0.5 and 2.0 ± 0.6 keV, respectively. The ratio of the fluxes in the $K\alpha$ and $K\beta$ lines is $F\alpha/F\beta = 2.4 \pm 0.8$ without any correction for absorption or $F\alpha/F\beta = 3.6 \pm 1.5$ with a correction for absorption ($n_H L = 9.4 \times 10^{23}$ cm^{-2}; see the table). Note that this value is lower than the theoretical ratio of the $K\alpha$ and $K\beta$ fluorescence yields (∼8). Part of the discrepancy may result from radiative transfer in the dense medium that obscures the X-ray source.

The presence of a second line at energy ∼7.05 keV

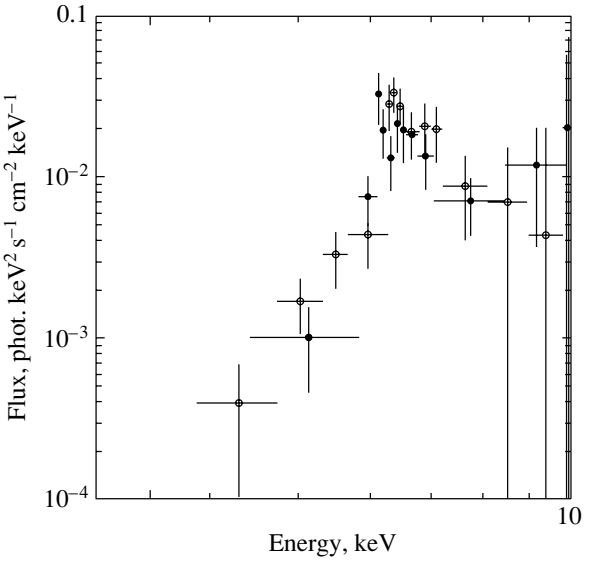

Fig. 4. The spectrum of IGR J16318−4848, as constructed from SIS (open circles) and GIS (filled circles) data.

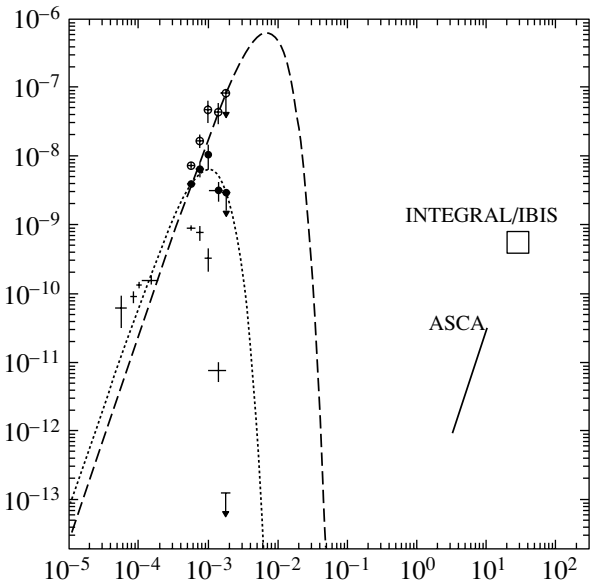

Fig. 5. The broadband spectrum of IGR J16318−4848, as constructed from various observations. The filled and open circles represent the fluxes corrected for interstellar absorption with the parameters $A_V = 13$ and 20 (Fitzpatrick 1999). The dotted and dashed lines indicate the rough fits to the points in the near infrared using a blackbody spectrum with effective temperatures of 3000 and 20 000 K, respectively.

is confirmed by the XMM observations (Schartel *et al.* 2003; de Plaa *et al.* 2003).

Now, having fixed the emission-line parameters, we will fit the source's spectrum by using 2- to 10-keV data from all of the ASCA instruments. For this purpose, we will include neutral photoabsorption in the model. The fitting results are presented in the table.

ARCHIVAL OBSERVATIONS OF THE SOURCE IN VARIOUS ENERGY RANGES

The TTM (Brinkman *et al.* 1985) and SIGMA (Paul *et al.* 1991) coded-mask X-ray telescopes repeatedly observed the region of the sky around IGR J16318−4848 (the SIGMA observations of this sky region were described by Trudolyubov *et al.* (1998)), but the source was not detected. The sensitivity of these telescopes imposes the following constraints on the mean flux from the source: $F_{2-30\,\mathrm{keV}} < 2 \times 10^{-10}$ erg s^{-1} cm^{-2} (TTM) and $F_{40-100\,\mathrm{keV}} < 10^{-10}$ erg s^{-1} cm^{-2} (SIGMA). The sensitivity to short (of the order of a day) bursts is slightly lower—the peak flux during a burst could not exceed 5×10^{-10} and 2×10^{-10} erg s^{-1} cm^{-2}, respectively. The flux and its upper limit obtained from GRANAT/SIGMA and INTEGRAL/IBIS data suggest that the X-ray source is variable on a time scale of several years. It should be noted, however, that the IBIS energy range in which the flux was measured (Courvoisier *et al.* 2003) does not overlap with the SIGMA energy range (40 keV−1 MeV).

The analysis of archival observations of the source's region by Foschini *et al.* (2003) revealed a counterpart in several infrared bands (J, H, K, and 8.6 μm) and imposed an upper limit on the R magnitude of the counterpart, $m_R < 21$. We performed our own analysis of the 2MASS survey data and were able to refine the near-infrared brightness of IGR J16318−4848: $m_J \sim 10.2$, $m_H \sim 8.5$, $m_K \sim 7.5$. At present, the 2MASS data for the region under consideration do not allow accurate photometric measurements to be made. Therefore, the above values must be considered rough estimates of the actual fluxes.

Our analysis of DSS2 (http://archive.eso.org/dss/dss/) and CAI/MAMA (http://dsmama.obspm.fr/) sky-survey data showed the clear presence of the source in the I band at an $\sim 15^m$ level and its weak detection in the R band at a level of $19-20^m$.

Finally, our analysis of MSX data for the Galactic plane (Price *et al.* 2001) showed the presence of the source in the wavelength ranges 11−13 (with a flux of ∼0.54 Jy) and 13−16 (∼0.44 Jy) μm and, possibly, its weak detection in the range 18−26 μm (∼0.4 Jy).

All of the above fluxes from IGR J16318−484, which were determined at different times and in different energy ranges, are gathered together in Fig. 4.

DISCUSSION

The observations of IGR J16318–4848 in the energy range 2–10 keV show that its spectrum is unique.

–The measured 2–10-keV spectrum essentially consists of only emission-line photons; the line positions suggest that we are observing the fluorescence of neutral or weakly ionized matter.

–The observed photoabsorption is strong: the absorption column density is at least $n_H L \sim 4 \times 10^{23}$ cm^{-2} (the exact value obtained from observations strongly depends on the assumed spectral shape of the unabsorbed source) and significantly exceeds the value for the Galactic interstellar gas toward the source—about 2×10^{22} cm^{-2} (Dickey and Lockman 1990; Dame *et al.* 2001). Therefore, we may conclude that the bulk of the absorption observed in the source's X-ray spectrum takes place in its immediate vicinity.

An Active Galactic Nucleus?

Interestingly, similar X-ray spectra with strong absorption and a strong fluorescent line of neutral iron are observed for some of the type-2 Seyfert galaxies (see, e.g., Moran *et al.* 2001). This raises the following natural question: Is IGR J16318–4848 an active galactic nucleus (AGN) with strong absorption? In this scenario, it would be virtually impossible to see the galaxy itself with the coordinates $l = 335\overset{\circ}{.}6$ and $b = -0\overset{\circ}{.}45$ either in the near infrared, because of the huge interstellar absorption along the plane of our Galaxy toward the source ($A_V \sim 15$–30, Schlegel *et al.* 1998; Dickey and Lockman 1990; Dame *et al.* 2001), or in the far infrared, because of the strong intrinsic radiation from the Galaxy (see Kraan-Korteweg and Lahav 2000).

In this case, the distance to IGR J16318–4848 cannot be larger than ~5 Mpc, as follows from the statistically insignificant redshift of the X-ray iron line (this paper; de Plaa *et al.* 2003). Therefore, the AGN luminosity corrected for internal absorption did not exceed $\sim 6 \times 10^{41}$ erg s^{-1} in the energy range 2–10 keV during the ASCA and XMM observations and was most likely an order of magnitude higher than its value during the burst detected by the INTEGRAL observatory. Interestingly, three AGNs with strong absorption ($n_H L$ from 10^{23} to 5×10^{24} cm^{-2}) with comparable X-ray luminosities are already known within 5 Mpc of our Galaxy: Centaurus A, Circinus, and NGC 4945 (Matt *et al.* 2000).

However, the infrared spectrum of IGR J16318–4848 (corrected for absorption $A_V \sim 20$, see Fig. 4), which radically differs from the observed spectra of Seyfert galactic nuclei with strong absorption (see, e.g., Marconi *et al.* 2000), strongly argues against the hypothesis of an AGN. It should be emphasized that the contribution from stars of the host galaxy to the spectrum shown in Fig. 5 in the infrared cannot be significant, because the observed source is compact (its size is less than 100 pc at a distance of 5 Mpc).

A Source in a Molecular Cloud?

If we turn to the more plausible origin of the source in our Galaxy, then Galactic sources for which a similar X-ray spectrum would always be observed are virtually unknown. In the case of IGR J16318–4848, however, the ASCA and XMM observations separated by ~8.5 years showed almost identical spectra and fluxes (this paper; Murakami *et al.* 2003; Schartel *et al.* 2003; de Plaa *et al.* 2003).

The only known exception is the molecular cloud Sgr B2. Its radiation may be the reprocessing of a bright outburst of Sgr A*, a supermassive black hole at the center of our Galaxy (Sunyaev *et al.* 1993; Murakami *et al.* 2000). However, based on CO radio maps (Dame *et al.* 2001), the hypothesis that IGR J16318–4848 is located in a large molecular cloud may be virtually excluded. In addition, it may be concluded from XMM data (Schartel *et al.* 2003) that the angular size of the cloud from which scattered and fluorescent X-ray radiation would come to us cannot exceed 5″–6″; i.e., if the distance to the source is ~8 kpc, then the linear size of the cloud does not exceed ~0.3 pc. To provide the observed absorption column density ($>5 \times 10^{23}$ cm^{-2}), a homogeneous cloud of this size must have a number density of $\sim 10^6$ cm^{-3}. This value is much higher than the typical number densities of molecular clouds in the Galaxy (see, e.g., Solomon *et al.* 1987).

An X-ray Binary in an Eclipse?

Such strong photoabsorption is observed during eclipses/dips (see, e.g., Church *et al.* 1998). In principle, we cannot rule out the possibility that the two (ASCA and XMM) observations took place during an eclipse of the X-ray source: the ASCA observation lasted only for 4 ks, and the XMM observation lasted for 27 ks. If the orbital period of the binary IGR J16318–4848 is at least two or three days, then this is possible but unlikely. However, even in this case, the almost complete absence of detectable radiation at energies <3 keV is very unusual (cf., e.g., the spectra of Vela X-1 or Cen X-3 during an eclipse in the papers by Sako *et al.* (1999) and Wojdowski and Liedahl (2001)).

An X-ray Source in a Compact Envelope?

If the ASCA and XMM observations of IGR J16318–4848 did not take place during eclipses in the X-ray binary, then the presence of strong absorption inevitably leads us to conclude that the source must be in a dense envelope. This envelope can also serve as the source of the fluorescent ($K\alpha$ and $K\beta$) iron lines.

Let us now consider the infrared counterpart of IGR J16318–4848. In this case, the main problem is that the distance to the source is unknown and, bsesides, the distribution of gas and dust near the Galactic plane is known only roughly. Therefore the interstellar absorption A_V can, in principle, take on any value between 0 and ~30.

Figure 5 shows two sample near-infrared spectra that were obtained from the measured fluxes corrected for the possible absorption with $A_V = 13$ and 20. The reconstructed spectrum can be satisfactorily described by a blackbody spectrum with a temperature $T_{\rm eff} \sim 3000$ K in the former case (weaker absorption) and $T_{\rm eff} > 6000$ K in the latter case. The luminosity of the source (under the assumption of isotropic radiation from a spherical surface) is, respectively, $\sim 2 \times 10^{37} (D/5\ {\rm kpc})^2$ erg s^{-1} and $\sim 6 \times 10^{38} (T_{\rm eff}/6 \times 10^3\ {\rm K})^3 (D/5\ {\rm kpc})^2$ erg s^{-1}, where D is the distance to the source. The shape of the spectrum leads us to the following independent conclusion: the absorption toward the source cannot significantly exceed $A_V \sim 20$; otherwise, the reconstructed spectrum in the near infrared would be steeper than the Rayleigh–Jeans law.

The maximum possible value of $A_V \sim 20$ (which can be attributed to interstellar absorption) corresponds to a neutral-gas column density $n_H L \sim 3 \times 10^{22}$ cm^{-2}, which is at least an order of magnitude lower than the absorption observed in the X-ray spectrum of IGR J16318–4848. This result leads us to conclude that the dense cloud surrounding the source is compact, most likely of the order of a binary system or smaller.

If the radiation that we observe in the K–R spectral channels comes from the stellar surface, then the star could be, for example, a red giant ~4 kpc away with an effective temperature of ~3000 K and a luminosity of $\sim 10^{37}$ erg s^{-1}. Interestingly, such a star is the companion of a black hole—the well-known X-ray transient GRS 1915+105 (Greiner *et al.* 2001). However, the X-ray spectrum of GRS 1915+105 bears absolutely no resemblance to the strongly absorbed spectrum of IGR J16318–4848.

A different solution that also satisfies the measured fluxes, or, more specifically, a massive optical companion with an effective temperature of >10000 K and a luminosity of $\sim 3 \times 10^{39} (T_{\rm eff}/10^4\ {\rm K})^3 (D/5\ {\rm kpc})^2$ erg s^{-1}, seems more plausible. This, in turn, suggests two main possible cases.

First, IGR J16318–4848 can be a system similar to SS 433 in which supercritical accretion proceeds through a geometrically and optically thick disk shrouded in a semitransparent wind that outflows from the disk (see, e.g., Fabrika 1997). The observed infrared radiation from J16318–4848 could then originate from outer accretion-disk regions or from a supermassive optical companion, while the observed X-ray radiation could originate from the wind. It should be noted, however, that the source SS 433 is primarily known by its jets from which the optically thin X-ray radiation (with many Doppler-shifted lines) of a hot (with a temperature of the order of 10^8 K) plasma is detected (Kotani *et al.* 1996). In the case of IGR J16318–4848, however, the ASCA and XMM observations revealed no such spectroscopic evidence.

Second, IGR J16318–4848 may be similar to GX 301–2—an X-ray pulsar that accretes matter from an intense wind from the surface of Wray 977, a B-type supergiant with $T_{\rm eff} \sim 2 \times 10^4$ K and $L_{\rm bol} \sim 6 \times 10^{38}$ or 5×10^{39} erg s^{-1} (depending on whether the source is at a distance of 1.8 kpc (Parkes *et al.* 1980) or 5.3 kpc (Kaper *et al.* 1995)). If the companion of IGR J16318–4848 is similar to the star Wray 977 and is 2 to 5 kpc away, then the measured near-infrared spectrum can be explained. Moreover, the X-ray spectrum of GX 301-2 is characterized by strong photoabsorption, which changes from 2×10^{23} to 2×10^{24} cm^{-2} over the 41-day orbital cycle. Besides, it exhibits fluorescent iron lines similar to those observed in IGR J16318–4848 (Endo *et al.* 2002). Finally, note that in systems with massive envelopes (e.g., GX 301-2 or Cygnus X-3), the optically thin radiation from the envelope can significantly contribute to the infrared radiation (at wavelengths >5–10 m) (Davidson and Ostriker 1974; Ogley *et al.* 2001), and it is in this range that we observe the change in the spectral slope (Fig. 5).

ACKNOWLEDGMENTS

We are grateful to R.A. Burenin for help in analyzing the infrared observations. We used the data retrieved from the High-Energy Astrophysics Archive at the Goddard Space Flight Center (NASA).

REFERENCES

1. M. Abramowicz, B. Czerny, J. Lasota, and E. Szuszkiewicz, Astrophys. J. **332**, 646 (1988).
2. A. Brinkman, J. Dam, W. Mels, *et al.*, *Non-Thermal and Very High Temperature Phenomena in X-ray Astronomy,* Ed. by G. C. Perola and M. Salvati (Institute Astronomico, Rome, 1985), p. 263.

3. E. Churazov, M. Gilfanov, W. Forman, and C. Jones, Astrophys. J. **471**, 673 (1996).
4. M. J. Church, M. Balucinska-Church, T. Dotani, and K. Asai, Astrophys. J. **504**, 516 (1998).
5. T. Courvoisier, R. Walter, J. Rodriguez, *et al.*, IAU Circ. No. 8063 (2003).
6. T. Dame, D. Hartmann, and P. Thaddeus, Astrophys. J. **547**, 792 (2001).
7. A. Davidson and J. Ostriker, Astrophys. J. **189**, 331 (1974).
8. J. M. Dickey and F. J. Lockman, Ann. Rev. Astron. Astrophys. **28**, 215 (1990).
9. T. Endo, M. Ishida, K. Masai, *et al.*, Astrophys. J. **574**, 879 (2002).
10. S. Fabrika, Astrophys. Space Sci. **252**, 439 (1997).
11. E. Fitzpatrick, Publ. Astron. Soc. Pac. **111**, 63 (1999).
12. L. Foschini, J. Rodriguez, and R. Walter, IAU Circ. No. 8076 (2003).
13. J. Greiner, J. G. Cuby, M. J. McCaughrean, *et al.*, Astron. Astrophys. **373**, L37 (2001).
14. L. Kaper, H. Lamers, E. Ruymaekers, *et al.*, Astron. Astrophys. **300**, 446 (1995).
15. T. Kotani, N. Kawai, M. Matsuoka, and W. Brinkmann, Publ. Astron. Soc. Jpn. **48**, 619 (1996).
16. R. C. Kraan-Korteweg and O. Lahav, Astron. Astrophys. Rev. **10**, 211 (2000).
17. A. Marconi, E. Oliva, P. P. van der Werf, *et al.*, Astron. Astrophys. **357**, 24 (2000).
18. G. Matt, A. C. Fabian, M. Guainazzi, *et al.*, Mon. Not. R. Astron. Soc. **318**, 173 (2000).
19. E. Moran, L. Kay, M. Davis, *et al.*, Astrophys. J. **556**, L75 (2001).
20. H. Murakami, K. Koyama, M. Sakano, and M. Tsujimoto, Astrophys. J. **534**, 283 (2000).
21. H. Murakami, T. Dotani, and R. Wijnands, IAU Circ. No. 8070 (2003).
22. R. Ogley, S. Bell Burnell, and R. Fender, Mon. Not. R. Astron. Soc. **322**, 177 (2001).
23. B. Paczynsky and P. J. Wiita, Astron. Astrophys. **88**, 23 (1980).
24. G. Parkes, J. Culhane, K. Mason, and P. Murdin, Mon. Not. R. Astron. Soc. **191**, 547 (1980).
25. J. Paul, J. Ballet, M. Cantin, *et al.*, Adv. Space Res. **11**, 289 (1991).
26. J. de Plaa, P. den Hartog, J. Kaastra, *et al.*, Astronomer's Telegram **119** (2003); http://www.atel.caltec.edu.
27. S. Price, M. Egan, S. Carey, *et al.*, Astron. J. **121**, 2819 (2001).
28. M. Revnivtsev, M. Gilfanov, E. Churazov, and R. Sunyaev, Astron. Astrophys. **391**, 1013 (2002).
29. M. Sako, D. Liedahl, S. Kahn, and F. Paerels, Astrophys. J. **525**, 921 (1999).
30. N. Schartel, M. Ehle, M. Breitfellner, *et al.*, IAU Circ. No. 8072 (2003).
31. D. J. Schlegel, D. P. Finkbeiner, M. Davis, *et al.*, Astrophys. J. **500**, 525 (1998).
32. N. Shakura and R. Sunyaev, Astron. Astrophys. **24**, 337 (1973).
33. P. Solomon, A. Rivolo, J. Barret, and A. Yahil, Astrophys. J. **319**, 730 (1987).
34. R. Sunyaev, M. Markevitch, and M. Pavlinsky, Astrophys. J. **407**, 606 (1993).
35. Y. Tanaka, H. Inoue, and S. Holt, Publ. Astron. Soc. Jpn. **46**, 37 (1994).
36. S. Trudolyubov, M. Gilfanov, E. Churazov, *et al.*, Astron. Astrophys. **334**, 895 (1998).
37. P. Wojdowski and D. Liedahl, Astrophys. J. **547**, 973 (2001).

Translated by V. Astakhov

Astronomy Letters, Vol. 29, No. 9, 2003, pp. 594–598. Translated from Pis'ma v Astronomicheskiĭ Zhurnal, Vol. 29, No. 9, 2003, pp. 672–677.

Long-Term Modulation of the Galactic Cosmic-Ray Fluctuation Spectrum

S. A. Starodubtsev[1]* and I. G. Usoskin[2]

[1] *Institute of Cosmophysical Research and Aeronomy, Siberian Branch, Russian Academy of Sciences, pr. Lenina 31, Yakutsk, 677891 Russia*

[2] *Sodankylä Geophysical Observatory (Oulu Unit), University of Oulu, P.O. Box 3000, FIN-90014, Finland*

Received February 6, 2003

Abstract—We study the temporal behavior of the power spectra for Galactic cosmic-ray fluctuations during the last two solar cycles. We use the 5-min data for 1980–2002 corrected for the barometric effect from two widely separated high-latitude cosmic-ray stations, Tixie Bay and Oulu. The cosmic-ray fluctuation spectrum is shown to be subjected to a regular long-term modulation with a period of about 11 years in phase with the solar cycle, in accordance with the variations in the inertial part of the turbulence spectrum for the interplanetary magnetic field. Based on independent measurements, we confirm the previously detected cosmic-ray fluctuation power enhancement at the maximum of the 11-year solar cycle and its subsequent decrease at minimum solar activity using new, more extensive data sets. We reach the conclusion about the establishment of a new cosmic-ray modulation phenomenon that has not been described previously in scientific literature. © *2003 MAIK "Nauka/Interperiodica"*.

Key words: *cosmic rays, solar activity.*

INTRODUCTION

Of the entire observed variety of cosmic-ray (CR) variations—temporal and spatial Galactic CR flux variations—the class of short-period variations—with periods from several minutes to several hours—is least understood. In scientific literature, this class of variations is called CR fluctuations. This name in many respects stems from the fact that the fluctuation amplitude is comparable to the noise level recorded by ground-based CR detectors. In general, a ground-based study of the CR fluctuations is based on neutron-monitor data due to the high efficiency of the counters and the large area of the detectors. In a 5-min recording mode, the statistical measurement error of the Galactic CR intensity for various stations is $\sigma \approx 0.7\%$, while the amplitude of the fluctuations themselves rarely exceeds 1.0%. Thus, the main problem in studying the CR fluctuations is to isolate the useful signal against a high noise background. The main tool for solving this problem is a spectral analysis of time series.

A systematic study of the physical nature of the CR fluctuations and the dynamics of their power spectrum began 30 years ago (Kozlov *et al.* 1973). By now, undeniable progress has been made in this field of studying the CR variations. Analysis of data from the numerous experiments carried out at different CR stations in different countries established the interplanetary origin of the CR fluctuations and revealed the characteristic frequency dynamics of the fluctuation power spectra before the arrival of large-scale solar-wind (SW) disturbances at the Earth's orbit (Starodubtsev 1985; Vashenyuk *et al.* 1995; Dorman *et al.* 1995; Perez-Peraza *et al.* 1998; Kudela *et al.* 1999; Kozlov *et al.* 2001) and their relationship to the IMF turbulence spectrum (Owens 1974; Toptygin 1983; Berezhko and Starodubtsev 1988).

The CR fluctuation spectra are very dynamic; they continuously exhibit variations both in the frequency range and in power, depending on the SW state. As a result, the information flow contained in them is very large. Therefore, analysis of the spectra, especially on long time scales, encounters considerable difficulties. To overcome these difficulties, some authors introduce various CR fluctuation indices that describe the temporal behavior of the CR power spectra (Kudela and Langer 1995; Kudela *et al.* 1999; Kozlov *et al.* 2001). These indices allow us to study the dynamics of the spectra on long time scales and to draw definitive conclusions.

Such an approach was used by Berezhko *et al.* (1993). Based on 5-min data from the Tixie neutron monitor, they calculated the monthly mean index of the CR fluctuation spectral power density $\overline{G}$ by using

*E-mail: starodub@ikfia.ysn.ru

Basic parameters of the Tixie and Oulu high-latitude CR stations

Station	Device type	Geographic latitude λ	Geographic longitude ϕ	Geomagnetic rigidity cutoff threshold R_C, GV
Oulu	9NM64	65°02	25°2	0.81
Tixie	12NM64	71°60	128°9	0.53

the fast Fourier transform and studied its behavior during the solar cycle (1980–1990). As a result of their studies, they concluded that there was a significant correlation between the CR fluctuation amplitude and the level of solar activity and hypothesized the corresponding spectral evolution of the magnetosonic SW turbulence associated with solar-flare activity.

If this modulation effect in Galactic CRs actually exists, then it must also be observed in data from other stations with parameters similar to those of the Tixie CR station. Here, our goal is to reliably establish this phenomenon by using independent measurements at two CR stations on a long time scale.

DATA AND THE TECHNIQUE OF ANALYSIS

In this paper, we use continuous 5-min CR recording data from the CR stations Tixie (Russia) and Oulu (Finland). The Tixie and Oulu data cover the periods from January 10, 1980, through June 25, 1991, and from January 19, 1985, through October 16, 2002, respectively. Thus, the observational data mutually overlap by 6.5 years and make it possible to mutually calibrate the measurements. As a result, the period under study spans more than 22 years (from 1980 until 2002), begins from the maximum of solar cycle 21, and includes the maximum of solar cycle 23.

The table lists the basic parameters of the stations. The two high-latitude stations are located at the sea level and have similar geomagnetic rigidity cutoff thresholds $R_C < 1$ GV; i.e., the effect of the Earth's magnetic field on the recorded CR particle fluxes is weak. Thus, the minimum energies of the CR particles that arrive at the stations are mainly determined by the thickness of the atmosphere. Both stations have narrow asymptotic acceptance cones for CR particles with energy up to 10 GeV (Inoue *et al.* 1983). The stations are widely separated in longitude, by more than 100°, suggesting an independence of the time series used in our analysis. Both stations are equipped with similar instruments—NM-64 neutron monitors, but a different number of counters: 12 at the Tixie station and 9 in Oulu, which affects the statistical counting of the instruments.

To avoid erroneous conclusions, in the primary reduction of the CR measurements great attention should be paid to the corrections for meteorological effects. Since the effect of the Earth's atmospheric temperature on the neutron CR component is less than 0.01% (Dorman 1974), we analyze here 5-min data corrected only for the much stronger barometric effect.

An indispensable condition for using data in analysis is their quality. As the initial data (as in Berezhko *et al.* 1993), we took a daily realization (288 points). In the absence of apparent errors and gaps for more than two hours (24 points), we considered them suitable for our analysis. In addition, we excluded from our analysis the periods when solar CR events were recorded at the stations; in general, such solar proton events have a rapid ($\sim$1 h), sharp rise and a large amplitude, which significantly distorts the results of the spectral analysis. We did not exclude Forbush decreases from our analysis, because the CR decrease in the 5-min data has the pattern of a low-frequency trend, which can be eliminated by digital filtering.

To compare the data from the two different stations, we expressed the CR intensity in percents of the average level for each data realization.

The first step in preparing the time series for spectral analysis is the standard procedure of reducing the data to a zero mean. The main problem in the spectral analysis is the signal-to-noise ratio. To obtain correct estimates of the calculated quantities, it is necessary to avoid here the power redistribution in the spectra in frequency.

Therefore, the next step—the reduction of the data to a quasi-stationary form—is achieved by high-frequency filtering. It can be implemented by any digital filter with an appropriate transfer function. An important condition at this step is the choice of a working filter frequency band $\nu_1 < \Delta\nu < \nu_2$. In our case, this band is determined at high frequencies by the data-sampling step $\Delta t = 300$ s, which corresponds to the Nyquist frequency $\nu_2 = 1.67 \times 10^{-3}$ Hz. The low frequency ν_1 of the working filter-frequency band $\Delta\nu$ is more difficult to choose, because it depends in many respects on the physical nature of the CR fluctuations under study. Here, taking into account the results of our previous studies (Berezhko and

Starodubtsev 1988; Berezhko *et al.* 1993; Starodubtsev 1999), we again chose it to be $\nu_1 = 1.67 \times 10^{-4}$ Hz.

In the third step of our analysis, we calculated the daily CR fluctuation power spectra by using the standard algorithm of Blackman and Tukey (1958). To reduce the power leakage through sidelobes, we used the Tukey correlation window, with the number of degrees of freedom being 12. Subsequently, from the daily spectra obtained in this way, we calculated the 27-day-averaged spectra $P(\nu)$ by using the ensemble averaging procedure; the errors in the estimated CR fluctuation power decreased sharply, while the number of degrees of freedom increased to 324.

It should be noted that Berezhko *et al.* (1993) used a different method of spectral analysis, a fast Fourier transform. Apart from its advantage—a considerable reduction in the computational time (by a factor of ~100)—this method has a serious drawback: when the spectrum is calculated from one data realization, the number of degrees of freedom is 2; therefore, the errors in the estimated spectral power are large. To overcome this effect, we used the procedure for ensemble averaging of the spectra, which increases the number of degrees of freedom and appreciably reduces the confidence intervals in estimating the power.

Thus, using the Blackman–Tukey method, we can not only check the previous results but also improve them.

In contrast to the monthly average, the 27-day average, which is related to the synodic solar rotation period, has a physical meaning and allows us to get rid of the quite possible effects of longitudinal inhomogeneities in the SW and the solar corona.

Next, to study the temporal behavior of the CR fluctuation power, we calculated the CR fluctuation power index $P2$ in the frequency range under investigation from the 27-day-averaged spectra (Kudela and Langer 1995):

$$P2 = \int_{\nu_1}^{\nu_2} P(\nu)d\nu.$$

In contrast to the $\overline{G}$ index (Berezhko *et al.* 1993), this quantity is the CR fluctuation power in the chosen frequency range, and we used it as the CR fluctuation index here.

In our analysis, we also used the 27-day data on the CR intensity J acquired at the Oulu station and normalized to September 1985. To avoid possible errors like a long-term trend, we corrected the data according to the information at http://cosmicrays.oulu.fi/readme.html#norm.

As the solar-activity index, we used the 27-day data on the sunspot number R_Z from the OMNI database at http://nssdc.gsfc.nasa.gov/omniweb/ow.html.

All of the data were time referenced according to the Bartels rotation numbers.

RESULTS AND DISCUSSION

Figure 1 shows the sunspot number R_Z (Fig. 1a), which is the universally accepted solar-activity index, the CR intensity J recorded at the Oulu station (Fig. 1b), and the CR fluctuation indices $P2$ (Fig. 1c) calculated for the two CR stations for the period under study. For the Tixie and Oulu stations, the $P2$ index is indicated by filled squares and open circles, respectively. To mutually normalize the data, the CR fluctuation index $P2$ was multiplied by a constant factor of 1.33, because of the different statistical counting of the neutron monitors at these stations.

We clearly see from Figs. 1a and 1b that the sunspot numbers and the CR intensity are in antiphase, whereas the CR fluctuation indices (Fig. 1c), on the contrary, vary synchronously with the solar-cycle phase. The CR fluctuation indices $P2$ calculated from the data of the two stations closely match in the overlapping time interval and complement each other, which allows them to be considered as a single index throughout the interval under study.

Our calculation of the correlation matrix between the CR index $P2$ for the Oulu station and the sunspot number R_Z for Bartels rotations 2070–2299 suggests a significant correlation $\rho(\tau) = 0.67$ for a zero shift and its increase to $\rho = 0.71$ for a shift of $\tau = 10$ solar rotations. This implies that our result is with a high probability (a significance level $\alpha < 0.1$), not accidental and that the $P2$ index peaks at the beginning of the decline in solar activity, when enhanced flare and coronal solar activity is observed (Starodubtsev 1999). The derived correlation coefficients for the Oulu station closely match those calculated previously by Berezhko *et al.* (1993) for the Tixie station ($\rho(0) = 0.60$, $\rho(10) = 0.78$, $\alpha < 0.05$). The small discrepancy stems from the fact that here we use the 27-day CR and solar-activity indices rather than the monthly indices, as in the cited paper. In addition, the $P2$ and $\overline{G}$ indices have a slightly different physical meaning, and they were calculated by using different techniques.

It also follows from Figs. 1b and 1c that the CR fluctuation index anticorrelates with the CR intensity. In this case, the maximum value of the correlation function $\rho(\tau) = -0.78$ is observed without any shift ($\tau = 0$). Thus, the maximum CR fluctuation amplitude is observed when the CR intensity J reaches its minimum at high solar activity.

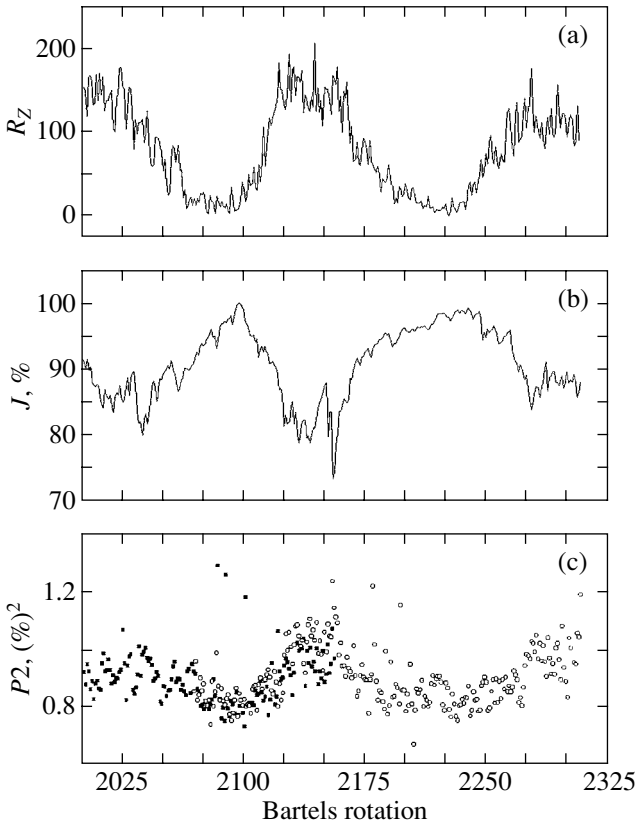

Fig. 1. The temporal behavior of the sunspot number R_Z (a), the CR intensity recorded at the Oulu station J (b), and the CR fluctuation index $P2$ (c) relative to the Bartels rotation number.

At the same time, the CR intensity itself is in antiphase with the sunspot number, and the maximum of the correlation function $\rho(\tau) = -0.90$ is observed for a shift of $\tau = 5$ Bartels rotations, which corresponds to the mean delay between the solar-activity and CR variations (Usoskin *et al.* 1998). It thus follows that the ground-level CR intensity minimum slightly lags behind the solar maximum, and the intensity variations themselves are also related to manifestations of flare and coronal solar activity.

Let us briefly discuss the possible physical mechanism of the observed CR fluctuations. Several authors (Owens 1974; Toptygin 1983; Berezhko and Starodubtsev 1988) developed a theory of CR fluctuations in random magnetic fields and compared it with observations. In these papers, the fact that a modulation can arise from both Alfvén and magnetosonic waves during the interaction of high-energy CRs ($E \sim 1$ GeV) with the interplanetary magnetic field engages our attention. In the former and latter cases, the anisotropic and much larger (in magnitude) isotropic parts of the CR distribution function are modulated, respectively. In the case of Alfvén waves, the observed CR fluctuation spectra are satisfactorily described by the theory down to frequencies $\nu < 10^{-4}$ Hz (Owens 1974). This restriction can be understood if we take into account the fact that, in this case, a CR modulation occurs during the resonant interaction with the random IMF component; for typical SW conditions (a magnetic field intensity $B = 6$ nT, a SW speed $U = 400$ km s^{-1}), the resonant frequencies for Alfvén waves are $\nu_{\rm res} \approx 1.18 \times 10^{-3}$ Hz and $\nu_{\rm res} \approx 1.05 \times 10^{-4}$ Hz for CR particles with energies of 5 and 500 MeV, respectively. At the same time, the CRs recorded by neutron monitors, even at high latitudes, have a minimum energy $E > 500$ MeV. In contrast, for the CR modulation by fast magnetosonic SW turbulence, the theoretical CR fluctuation spectra in the frequency range studied here agree well with the observed spectra (Berezhko and Starodubtsev 1988).

Thus, the results presented in the figure are consistent with the conclusions of Berezhko *et al.* (1993) and also lead us to conclude that the small-scale ($\sim 10^{10}$–10^{12} cm), presumably magnetosonic SW turbulence level must behave in a similar way during the solar cycle. Indeed, as we showed previously (Starodubtsev 1999), significant (by more than two orders of magnitude) regular variations are also observed during the 11-year solar cycle in the inertial

part of the IMF turbulence spectrum in the same frequency range. The local (near the Earth's orbit) generation of MHD waves by the streams of low-energy CRs ($E_p \sim (0.01-10)$ MeV) associated with coronal solar activity (flares and coronal mass ejections) may be responsible for this phenomenon (see Starodubtsev *et al.* (1999) and references therein).

Unfortunately, the available 5-min IMP-8 IMF data only slightly (about 7 years) overlap with the CR data from the two stations. Therefore, we cannot quantitatively study the correlation between the CR fluctuation index $P2$ and the SW turbulence level during the solar cycle. In addition, the IMF measurements are discrete in nature and carry information about the local properties of the medium, while CRs carry information about the integrated properties, and various types of MHD waves are simultaneously present in the observed IMF spectra. Therefore, a high, significant correlation between them on large time scales can hardly be expected.

CONCLUSIONS

Our results provide evidence for the long-term high-frequency modulation of the Galactic CR fluctuation spectrum. In essence, we have confirmed a new, previously unknown CR phenomenon, which was first described by Berezhko *et al.* (1993). It is also confirmed by the corresponding measurements of the inertial part of the IMF fluctuation spectrum during the solar cycle (Starodubtsev 1999), which would be expected from the nature of the CR fluctuations (Berezhko and Starodubtsev 1988).

This phenomenon is observed for particles with energy E of at least $\sim$1 GeV. In the future, it will be undoubtedly of interest to determine the energy thresholds of the high-frequency CR flux modulation. This requires data from mid- and low-latitude CR stations with a sampling step of several minutes in a time interval that covers at least one solar cycle, as well as low-energy CR flux measurements in interplanetary space from spacecraft.

One might expect a considerable increase in the IMF turbulence level in 2003 from the behavior of the CR fluctuation index $P2$, which can appreciably affect the behavior of many parameters of the interplanetary medium and the Earth's magnetosphere.

At present, the 5-min data from the neutron monitors of the above stations are available online in the Internet at http://cosmicrays.oulu.fi and http://www.ysn.ru/ipm.

ACKNOWLEDGMENTS

We are grateful to the National Space Science Data Center, the Goddard Space Flight Center (Greenbelt, MD, USA), for the OMNI database. This work was supported in part by the Russian Foundation for Basic Research (project no. 01-02-17278) and the INTAS (grant no. 2000-0752).

REFERENCES

1. E. G. Berezhko, I. A. Brevnova, and S. A. Starodubtsev, Pis'ma Astron. Zh. **19**, 749 (1993) [Astron. Lett. **19**, 304 (1993)].
2. E. G. Berezhko and S. A. Starodubtsev, Izv. Akad. Nauk SSSR, Ser. Fiz. **52**, 2361 (1988).
3. R. B. Blackman and J. W. Tukey, *The Measurement of Power Spectra* (Dover. Mineola, New York, 1958).
4. L. I. Dorman, *Cosmic Ray Variations and Space Explorations* (North-Holland, Amsterdam, 1974), p. 675.
5. L. I. Dorman, G. Villoresi, A. V. Belov, *et al.*, Nucl. Phys. B (Proc. Suppl.) **39**, 136 (1995).
6. A. Inoue, M. Wada, and I. Kondo, *Cosmic Ray Tables* (Institute of Physical and Chemical Research, Itabashi, Tokyo, 1983), No. 1.
7. V. I. Kozlov, A. I. Kuzmin, G. F. Krymsky, *et al.*, *Proc. of the 13th ICRC, Denver, USA* **2**, 939 (1973).
8. V. I. Kozlov, S. A. Starodubtsev, V. G. Grigor'ev, *et al.*, Izv. Ross. Akad. Nauk, Ser. Fiz. **65**, 385 (2001).
9. K. Kudela and R. Langer, Contrib. Astron. Obs. Skalnate Pleso **25**, 5 (1995).
10. K. Kudela, I. M. Martin, and P. Bobik, *Proc. 26th ICRC, Salt Lake City, Utah, USA* **6**, 444 (1999).
11. K. Kudela, M. Storini, M. Hofer, and A. Belov, Space Sci. Rev. **93**, 153 (2000).
12. A. J. Owens, J. Geophys. Res. **79**, 895 (1974).
13. J. Perez-Peraza, A. Leyva-Contreras, I. Ya. Libin, *et al.*, Geofis. Int. **37**, 87 (1998).
14. S. A. Starodubtsev, Geomagn. Aéronom. **25**, 997 (1985).
15. S. A. Starodubtsev, Pis'ma Astron. Zh. **25**, 626 (1999) [Astron. Lett. **25**, 540 (1999)].
16. I. N. Toptygin, *Cosmic Rays in Intraplanetary Magnetic Fields* (Nauka, Moscow, 1983).
17. I. G. Usoskin, H. Kananen, G. A. Kovaltsov, *et al.*, J. Geophys. Res. **103**, 9567 (1998).
18. E. V. Vashenyuk, V. S. Smirnov, V. S. Ismagilov, *et al.*, *Proc. of the 24th ICRC, Roma, Italy* **4**, 880 (1995).

Translated by G. Rudnitskii

Astronomy Letters, Vol. 29, No. 9, 2003, pp. 599–611. Translated from Pis'ma v Astronomicheskiĭ Zhurnal, Vol. 29, No. 9, 2003, pp. 678–691.

Optical Monitoring of the Central Region of the Globular Cluster M 15 = NGC 7078: New Variable Stars

A. P. Zheleznyak[1*] and V. V. Kravtsov[2]**

[1] *Research Institute of Astronomy, Kharkov National University, Kharkov, Ukraine*
[2] *Sternberg Astronomical Institute, Universitetskii pr. 13, Moscow, 119992 Russia*

Received February 28, 2003

Abstract—We obtained a series of more than two hundred R-band CCD images for the crowded central ($115'' \times 77''$) region of the metal-poor globular cluster M 15 with an angular resolution of $0''.5$–$0''.9$ in most images. Optimal image subtraction was used to identify variable stars. Brightness variations were found in 83 stars, 55 of which were identified with known cluster variables and the remaining 28 are candidates for new variables. Two of them are most likely SX Phe variables. The variability type of two more stars is uncertain. The remaining stars were tentatively classified as RR Lyrae variables. A preliminary analysis of published data and our results shows that the characteristics of RR Lyrae variables in the densest part ($r < 35''$) of the cluster probably change. More specifically, the maximum of the period distribution of first- and second-overtone (RR1, RR2) pulsating stars shifts toward shorter periods; i.e., there is an increase in the fraction of stars pulsating with periods $<0^d.3$ and a deficiency of stars with $0^d.35$–$0^d.40$. The ratio of the number of these short-period RR Lyrae variables to the number of fundamental-tone (RR0) pulsating variables changes appreciably. We found and corrected the error of transforming the coordinates of variables V128–155 in M 15 into the coordinate system used in the catalog of variable stars in globular clusters.

Key words: *star clusters and associations; stellar dynamics; stars, variable and peculiar.*

INTRODUCTION

Globular clusters, particularly their densest central regions, are among the objects whose observational study, as well as the range and level of problems to be solved, significantly depend on the limiting angular resolution achievable in observations. Obviously, new important results of the study of the stellar composition and basic parameters of globular clusters in our Galaxy and others have been obtained from observations that have recently been performed with the Hubble Space Telescope (HST) and ground-based telescopes installed at sites with the best astronomical climate.

The detection and study of photometrically variable objects in crowded stellar fields belong to the range of problems related to the investigation of the stellar populations of globular clusters. Observationally, variable stars of low (compared to RR Lyrae stars) luminosity and small variability amplitude in the central regions of these clusters are the most difficult objects to detect. These primarily include the stars that fall into the region of the so-called blue stragglers in the color–magnitude diagram, as well as the region of the turnoff point and near the main sequence. They are represented by pulsating, eclipsing, and cataclysmic variables. Our primary objective was to attempt to detect such stars, along with hitherto undetected RR Lyrae variables, in the densest central part of the globular cluster M 15, where their number can be large, considering the parameters and the stage of dynamical evolution of this cluster.

By its parameters, M 15 is, in a sense, a unique object among the Galactic globular clusters, especially among those observable in the Northern Hemisphere. According to the catalog by Harris (1996),[1] M 15 is simultaneously among the clusters with the highest mass, central star-crowding level, and density and is at the evolutionary stage of postcore collapse. This is so far the only Galactic globular cluster for which evidence for the presence of a central intermediate-mass black hole has been obtained (Gerssen *et al.* 2002, 2003). In addition, it is distinguished by a large population (more than 150) of discovered variable stars

*E-mail: zheleznyak@astron.kharkov.ua
**E-mail: scorpi@sai.msu.ru

[1] A full updatable catalog is accessible at http://www.astro.utoronto.ca/people.html.

1063-7737/03/2909-0599$24.00

(Clement *et al.* 2001),[2] the overwhelming majority of which are RR Lyrae stars. Recently, this population has been supplemented with new low-luminosity variables (Jeon *et al.* 2001a, 2001b).

In Section 1, we describe the observational data, their reduction, and our method of searching for variables and their photometry. Basic data on the new variable stars are presented and described in Section 2. In Section 3, we make a preliminary comparison of the parameters of the populations of RR Lyrae variables in the central and outer parts of M 15.

1. OBSERVATIONS AND THEIR REDUCTION

Our observational data form the basis for solving the problem formulated above. These data aptly combine a high time resolution and a stable subarcsecond angular resolution throughout the two sets (each three hours long) of our optical monitoring of the central region in the globular cluster M 15.

Observational Data and Preliminary Reduction

We carried out our observations with the 1.5-m AZT-22 telescope at the Maidanak Observatory (Mount Maidanak, Uzbekistan) during two consecutive nights, on July 31 and August 1, 2001. The two nights were estimated to be photometric. The detector was an ST7 CCD camera mounted at the short (1:7.7) Ritchey–Chrétien focus of the AZT-22 telescope. The CCD array of the camera has 765×510 light-sensitive pixels 9×9 μm in size, which corresponds to a pixel angular size of $0''.15 \times 0''.15$ and a $115'' \times 77''$ field of view of the camera for this AZT-22 configuration. The observations were performed in a photometric band close to the standard Johnson–Cousins R band in a continuous frame-by-frame imaging mode with an exposure of 1 min per frame. Given the image digitization and recording time, the imaging rate was about 40 frames per hour. The upper culmination of M 15 occurred at the middle of each set of observations. The total volume of our observational data for the two nights was 248 frames (below, by the term *frame*, we mean the two-dimensional array of counts that reproduces the intensity distribution in the recorded *image*). The seeing estimated for all of our frames from the full width of the seeing image at half maximum (FWHM) showed a subarcsecond resolution almost for the entire volume of our data. The average seeing for the two sets was $0''.74$; an appreciable fraction of frames has a seeing FWHM $< 0''.6$.

[2] An updatable catalog is accessible at http://www.physun.physics.mcmaster.ca/Globular.html.

The preliminary CCD image reduction included the standard procedures of dark-current subtraction, flat fielding, and cosmic-ray particle hit removal. The mean dark current was estimated by averaging a series of 15 "dark" frames, which gives a dark-current master frame. The normalized master frame of a uniform flat field obtained by the median combination of a series of 15 frames containing the R-band images of twilight sky regions was used for the flat fielding. Charged cosmic-ray particle hits in the form of quasi-pointlike peaks were identified in each frame and removed by interpolating the counts in the surrounding pixels. Previously, when studying the photometric properties of the ST7 camera, we found a slight nonlinearity of the output signal (about 10% in the entire range), which probably results from the adjustments of the ST7 output amplifier. Based on tests, we obtained a dependence of the counts in the CCD image on the intensity of the input signal varied in a known way and fitted it by a polynomial. Using this fit, we corrected the intensity in each frame of observational data for nonlinearity.

The Data-Reduction Technique and Results

The search for and photometry of variable stars in crowded stellar fields are an important but, at the same time, difficult problem, particularly for extremely dense objects like the centers of globular clusters. The conventional approach to this problem realized in the standard software packages for stellar-field photometry (DaoPhot, DoPhot) is based on the point-spread function (PSF) fitting technique and involves the decomposition or modeling of groups of close stars by using a particular PSF representation method followed by the estimation of the coordinates and magnitude for each of the stars in the group. Although most of the stellar-field photometry results obtained to date are based on this approach, we know several difficulties that arise when using the PSF-photometry methods. At a high star density in the image, it becomes difficult both to estimate the underlying sky background level and to properly estimate the parameters of the PSF itself. Therefore, the problem of identifying and photometrically measuring variable sources becomes much more complex.

The above difficulties stimulated the search for alternative approaches to the problem of searching for variable objects in crowded stellar fields. In particular, image-subtraction methods were developed. In general, the input data in the search for variable objects are series of sequential frames that contain the images of objects in a selected region of the sky. The idea of the image-subtraction methods is to obtain information about the brightness behavior of a source by analyzing the difference between the

image in each of the frames from the series and the image in a fixed reference frame. The main problem in implementing the image-subtraction methods is the proper reduction of the PSF in the reference frame to the PSF in the current frame. The optimal image-subtraction (OIS) method that has recently been suggested by Alard and Lupton (1998) elegantly solves this problem and allows a nearly optimal difference between the images, i.e., limited by photon noise, to be obtained. The OIS method is based on the following simple assumption: if two images of the stellar field were resampled to a common coordinate system (centered), then the counts in the overwhelming majority of the pixels will be close if the PSFs of the two images are identical. The idea of the method is to determine the convolution kernel $\mathrm{Ker}(u,v)$ that reduces the reference image $R(x,y)$ to the current image $\mathrm{Im}(x,y)$ by analyzing the differences between the PSFs, i.e., to minimize the following difference in all pixels:

$$\sum_{x,y}([R\otimes \mathrm{Ker}](x,y)-\mathrm{Im}(x,y)-\mathrm{Bg}(x,y))^2\to\min, \quad (1)$$

where x,y are the coordinates in the centered frame, $\mathrm{Bg}(x,y)$ specifies the difference between the sky background counts, and the symbol $\otimes$ denotes a discrete convolution. The latter is defined in a pixel with x, y coordinates as

$$\sum_{u=x-p}^{x+p}\sum_{v=y-q}^{y+q}R(u,v)\mathrm{Ker}(x-u,y-v). \quad (2)$$

The convolution kernel $\mathrm{Ker}(u,v)$ is specified on a separate $(2p+1,\ 2q+1)$ array. Alard and Lupton (1998) suggested representing $\mathrm{Ker}(u,v)$ as a sum of fixed bivariate Gaussian functions (the parameters σ_k) modified by polynomials with a degree not higher than i and j:

$$\mathrm{Ker}(u,v)=\sum_{i,j,k,n}A_n e^{-\frac{(u^2+v^2)}{2\sigma_k^2}}u^i v^j. \quad (3)$$

Representation (3) allows the minimization problem (1) to be linearized with respect to the unknowns A_n. Thus, the parameters A_n of the optimal kernel $\mathrm{Ker}(u,v)$ can be determined by solving the system of linear equations by the least squares method. Without dwelling on the detailed description of the method by Alard and Lupton (1998), we note important advantages of the OIS method. When the system of normal equations is constructed, all pixels, i.e., in principle, complete information about the difference between the PSFs of the two images, are used to find the parameters A_n. The OIS method works more reliably when the star density in the image increases, because more pixels contain information about the PSF difference in denser fields. The intensity-conservation condition can be easily deduced by appropriately normalizing the kernel representation parameters A_n. Thus, any variations in transparency, exposure time, and the like between the images are automatically eliminated. Finally, the PSF variations over the field can be taken into account in the solution by introducing a dependence of the coefficients A_n on the coordinates.

In the case of proper subtraction, only the variable part of the intensity remains in the difference image. Thus, only variable objects that are unaffected by the surrounding field can be detected and measured. The difference images can be photometrically measured in a standard way—using aperture or PSF photometry. It should be noted that difference-image photometry gives the variable part of the flux from the object; i.e., when applied to the time sequence of images, it gives a light curve without the constant component. If the total flux is needed for a particular task, then the light curve should be calibrated by performing the photometry of the corresponding objects in the reference image by a standard method.

The idea of the OIS method underlies the software that we developed to process the images of M 15. The reduction algorithm consisted of the following steps:

(1) *Reference-image synthesis*. We selected nine frames with the best seeing (FWHM $\sim 0''.55$–$0''.58$) from the data of the two sets. Using a system of selected reference stars, we determined the image shifts/rotations in each of the selected frames relative to the coordinate system associated with the CCD array. Subsequently, all of the images were resampled to the same coordinate system by using bivariate spline interpolation and were combined pixel by pixel with median weighting. The resulting reference image has FWHM$= 0''.56$ and is virtually free from local defects.

(2) *Image centering*. For the subsequent reduction, all of the images for M 15 from the frames of the two observing sets were centered on the reference image. A correlation algorithm was used to determine the shift/rotation parameters. After the interpolation to the coordinate system of the reference image, the new sequence of centered frames was saved as a series of files.

(3) *Image subtraction*. The main procedure in calculating the difference between the current and reference images involves determining the parameters A_n of the optimal convolution kernel (3), which reduces the reference image to the current image. We specified the convolution kernel $\mathrm{Ker}(u,v)$ as a sum of three bivariate Gaussian functions with fixed

parameters σ_k (1.3, 2.25, and 3.9 pixels) in combination with bivariate modifying polynomials of degrees 4, 3, and 2, respectively. The array size for $\mathrm{Ker}(u, v)$ was 31×31 pixels; the difference between the sky background counts $\mathrm{Bg}(x, y)$ was specified by a bivariate polynomial of the first degree with appropriate coefficients. In our calculations, we broke down the frames of the reference and current images into nine equal rectangular fragments and determined the parameters A_n of the optimal kernel $\mathrm{Ker}(u, v)$ in each of these fragments. The coordinate dependence of the PSF may be disregarded within each fragment, which decreases the number of sought-for parameters to 36 and significantly reduces the expenditure of time on the calculations.

Having calculated A_n for a given fragment of the current frame, we constructed an optimal kernel $\mathrm{Ker}(u, v)$, convolved the corresponding fragment of the reference image with this kernel, and subtracted the convolution result from the current fragment. Analysis of the resulting difference image makes it possible to find and fix the coordinates of the pixels that significantly (by more than 3σ) deviate from the mean in a given region of the difference image and that are associated with variable objects or local defects. Using the coordinates of the marked pixels, we eliminated them from the original system of equations and obtained an improved solution by repeating the above procedure of calculating the parameters A_n.

Having performed the calculations in each of the nine fragments of the current frame, we combined the difference images and formed a full frame of the difference image, which was saved as a file. The absence of any steps at the fragment boundaries in the full difference image is an indicator of proper subtraction.

Figure 1 illustrates how the described algorithm works. The original fragments of the (Fig. 1a) reference and (Fig. 1b) current images for M 15 are shown in the upper part of the figure. Although the PSF in the fragment of the current image (Fig. 1b) is appreciably broader and has a complex elongated shape, the OIS method allows us to find a solution for the optimal convolution kernel $\mathrm{Ker}(u, v)$ (Fig. 1c) and perform the subtraction; the corresponding fragment of the difference image is shown in Fig. 1d. The variable stars ZK6 and 7 (the numbers are from our list; the prefix "ZK" means that the star is a candidate for new variables) are clearly identified; we see that in the current fragment, star ZK6 is fainter, while variable 7 is brighter than they are in the reference image. The modulus of the intensity distribution in the difference images of these variables, naturally, corresponds to the PSF of the current image. We also see from Fig. 1d that the subtraction of the surrounding nonvariable stars, including those overlapping with variables ZK6 and 7, was performed properly. The appreciable residual-intensity fluctuations in the difference image (Fig. 1d), which are mainly attributable to photon noise, are observed only at the positions of the brightest stars (see, e.g., to the left and below variable 7).

Having reduced the data from the two sets of observations of M 15 using the described algorithm, we obtained the corresponding series of difference-image frames for the subsequent analysis. The procedure for finding variable objects can be based both on the analysis of the behavior of each pixel with time, i.e., within the derived sequence, and on the analysis of the average frame from several sequential difference-image frames. We used both approaches to find variable objects. As a result of the selection, we identified a group of pixels with appreciable variability and determined their coordinates (the centroid of the modulus of the difference intensity distribution) in the coordinate system of the reference image. A list of potentially variable objects with the coordinates of their centroids was saved in a separate file for subsequent reduction. The formal measurement error of the centroid coordinates for most objects was about 0.1 pixel ($\sim 0''.02$). The ultimate selection of candidates for variable stars was based on photometric data.

We used aperture photometry, which is easier to realize, to measure objects in the difference image. An aperture 10 pixels ($1''.5$) in diameter was used to measure the intensity in the difference image. Based on the centroid coordinates from our list, we measured the intensity of each residual from all of the difference images. Objects with a deviation from the mean of more than 3% within the entire series were classified as candidates for variable stars. Since all of the images, both the original ones before the subtraction and the difference ones, were reduced to the same coordinate system, it will suffice to formally estimate the photometry error from the total-flux fluctuations within the measuring aperture. Placing the measuring aperture in star-centroid coordinates into the frame of the original (before the subtraction) image and summing the intensities, we estimate the rms measurement error σ_m from the total intensity in the aperture (under the assumption of Poisson statistics):

$$\sigma_m = \frac{1}{\sqrt{\sum_i (I_{0i} \times g)}}. \qquad (4)$$

The summation is over the pixels within the aperture (index i), I_{0i} is the intensity in pixel i before the subtraction (including the sky background), and g is the number of electrons per ADC unit. Our estimates of the formal error σ_m vary within the range $0^m.03$–$0^m.005$, depending on the object's brightness.

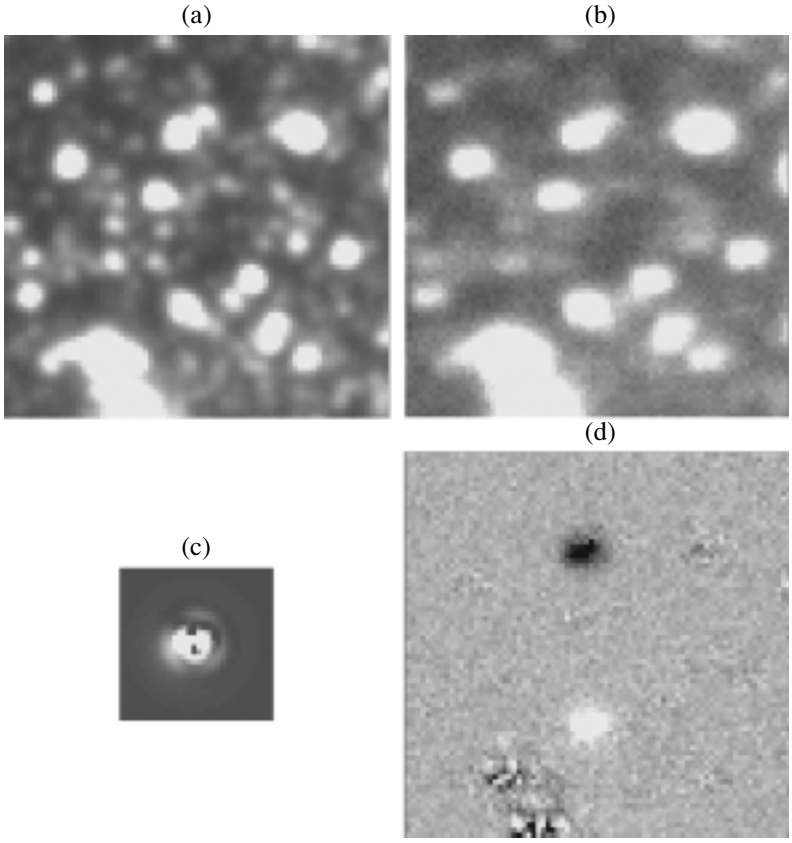

Fig. 1. An illustration of how the optimal image-subtraction (OIS) algorithm works. The original fragments of the (a) reference and (b) current images for M 15; the fragment size is $12'' \times 12''$; (c) the relative-intensity distribution in the optimal kernel $\mathrm{Ker}(u, v)$ calculated from the reference and current images by using the algorithm described in the text. The sizes of the shown image for $\mathrm{Ker}(u, v)$ are 31×31 independent pixels; the gradations for the visualization were chosen to optimally reproduce the faint outer wings. The relative-intensity distribution in the image of the optimal convolution kernel reflects the complex PSF shape for the current image (b); (d) the result of the subtraction of the fragment of the reference image (a) convolved with the optimal kernel from the fragment of the current image (b). The gradations were chosen to represent both positive (lighter) and negative (darker) fluctuations of the residual intensity near a zero mean (gray).

Since we have a sample of almost homogeneous measurements at our disposal, we can also directly estimate the photometry error by analyzing the scatter of individual points about the mean (e.g., on monotonic segments of the light curve after the elimination of the trend). The formal and direct estimates of the photometry errors made for several objects are in satisfactory agreement. Therefore, we considered it possible to use the formal estimate for the remaining objects.

Our reduction of the data from the two sets of observations in a $115'' \times 77''$ central region of M 15 revealed 83 stars with appreciable variability on short time scales. The coordinates and light curves relative to the reference frame form the basis for the subsequent analysis of our sample of candidates for variable stars.

2. NEW VARIABLE STARS

The Identification of Variables and the Determination of Their Coordinates

The overwhelming majority of the new variables in the densest central ($r < 20''$) region of M 15 were discovered in the past decade by Ferraro and Paresce (1993) and Butler *et al.* (1998), who used observations with the HST and the William Herschel (4.2-m) telescope, respectively. A series of several tens of cluster images with a subarcsecond angular resolution allowed the latter authors to confirm the variability of 15 stars from the list by Ferraro and Paresce (1993), to discover 13 new variables (apart from the two known variables V83 and V85), to obtain the phased light curves, and to determine the variability periods for all of these stars. In the catalog by Clement *et al.* (2001), these 28 new variables are designated as V128–155. However, their coordinates in this catalog proved to be erroneous in the sense that

they do not correspond to its coordinate system. This fact was established during the identification by using the cataloged and original data. The formulas in the catalog that were used to recalculate the coordinates are erroneous.

For the above stars, Butler *et al.* (1998) provided both highly accurate rectangular coordinates (in pixels) and a finding chart. Therefore, we were able to reliably identify 19 of the 28 stars with the corresponding stars from our list: V128–142 (46, 61, 58, 59, 60, 57, 56, 53, 51, 50, 38, 42, 35, 30, 36), V144 (25), V145 (24), V152 (45), V155 (66). The numbers of the variables from our list are given in parentheses. It does not include the nine remaining stars, because they exhibited no light variations in our images. Two more stars (565 and 1417) from the list by Butler *et al.* (1998), which most likely correspond to V83 and V85, are also reliably identified with stars 21 and 17 from our list, respectively.

Apart from the stars considered above, several dozen of other known variables from the catalog by Clement *et al.* (2001), which is known to be an extension of the catalog by Sawyer Hogg (1973), fall within our observed field of M 15. Unfortunately, the main drawbacks related to the rectangular (x'', y'') coordinate system of the catalog by Sawyer Hogg (1973) passed to the catalog by Clement *et al.* (2001). For well-known reasons, the accuracy of these coordinates in the catalog is low for most of the variable stars. In particular, as Kadla *et al.* (1988) pointed out, the positions of variables in M 15 were determined in two rectangular coordinate systems with a difference between the zero points larger than $2''$ along each of the axes back in the first quarter of the past century. Therefore, in some cases, confusion with the identification of variables arises, because the differences between their positions determined by different authors reach several arcseconds. In the absence of finding charts, this circumstance makes it difficult to unambiguously identify new variables with previously discovered ones. This is especially true for the central parts of variable-rich globular clusters, such as M 15, where the probability of a close neighborhood of variables is high. We also ran into this problem. However, Kadla *et al.* (1988) published a finding chart for variable stars in the part of the cluster concerned. Therefore, we were able to solve the problem more or less reliably with a number of controversial cases (see below) that arose when we used the cataloged information about the coordinates of the variables. The authors of the paper mentioned above reduced the coordinates for all of the variables known at that time in M 15 to the same coordinate system and pointed out the cases where the same stars were denoted in the catalog by different numbers.

The final identification procedure was performed as follows. We determined the variables from the catalog by Clement *et al.* (2001) that were most reliably identified with stars from our list (mostly in the outer parts of the observed cluster field) and transformed the coordinate system of the former to the coordinate system of the latter. Subsequently, we determined the equatorial coordinates for the stars from the list by Butler *et al.* (1998), our list, and the catalog by Clement *et al.* (2001), naturally, by excluding variables V128–155 from it. In this case, reference stars from the catalog of M 15 stars by Yanny *et al.* (1994) were used for referencing to the equatorial coordinate system. For the stars from all of the lists, we determined the differences $\Delta\delta$ and $\Delta\alpha$ from their equatorial coordinates relative to the M 15 center (the position of the object AC 211), whose coordinates, $\alpha_{2000} = 21^{\rm h}29^{\rm m}58\overset{\rm s}{.}26$ and $\delta_{2000} = +12^\circ10'02\overset{''}{.}90$, were taken from the same paper. Taking into account the small size of the cluster field under consideration and its relatively small angular distance from the celestial equator, we simultaneously take these differences as the rectangular coordinates (x'' and y'') in the system of the catalog by Clement *et al.* (2001).

The identification result is shown in Fig. 2. This figure clearly illustrates the above-described reliable and unambiguous identification of a total of 21 stars from our list with the corresponding stars from the list by Butler *et al.* (1998). The situation with the identification of stars from the catalog by Clement *et al.* (2001) proved to be less certain and reliable because of several controversial cases. As we see from Fig. 2, each of the stars with numbers 2, 8, 15, 19, 20, 26, 27, 28, 33, 73, and 75 clearly do not coincide with any of the nearby catalogued stars. However, on the finding chart from Kadla *et al.* (1988) mentioned above, they are identified with the catalogued variables V47, V120, V119, V117, V84, V109, V100, V115, V95, V106, and V107, respectively. For all of the remaining identified stars, the difference between their coordinates ($\Delta x''$ and $\Delta y''$) and those of the catalogued variables proved to be much smaller and such that $r < 2''$, where $r = \sqrt{(\Delta x'')^2 + (\Delta y'')^2}$. Below, we list the catalogued stars that (apart from the above eleven stars) were identified with stars from our list (their corresponding numbers are given in parentheses): V33 (82), V56 (1), V64 (83), V68–71 (76, 81, 77, 79), V73 (54), V75–77 (43, 49, 66), V79 (16), V81–83 (71, 70, 21), V85–90 (17, 29, 12, 41, 72, 7), and V92–94 (31, 9, 40). In addition, the position of variable 48 in the cluster closely ($<0\overset{''}{.}1$) matches the position of the well-known object AC 211 (Auriere and Cordoni 1981). Auriere *et al.* (1984) identified this object with the X-ray source X2127 + 119 located at the center of M 15.

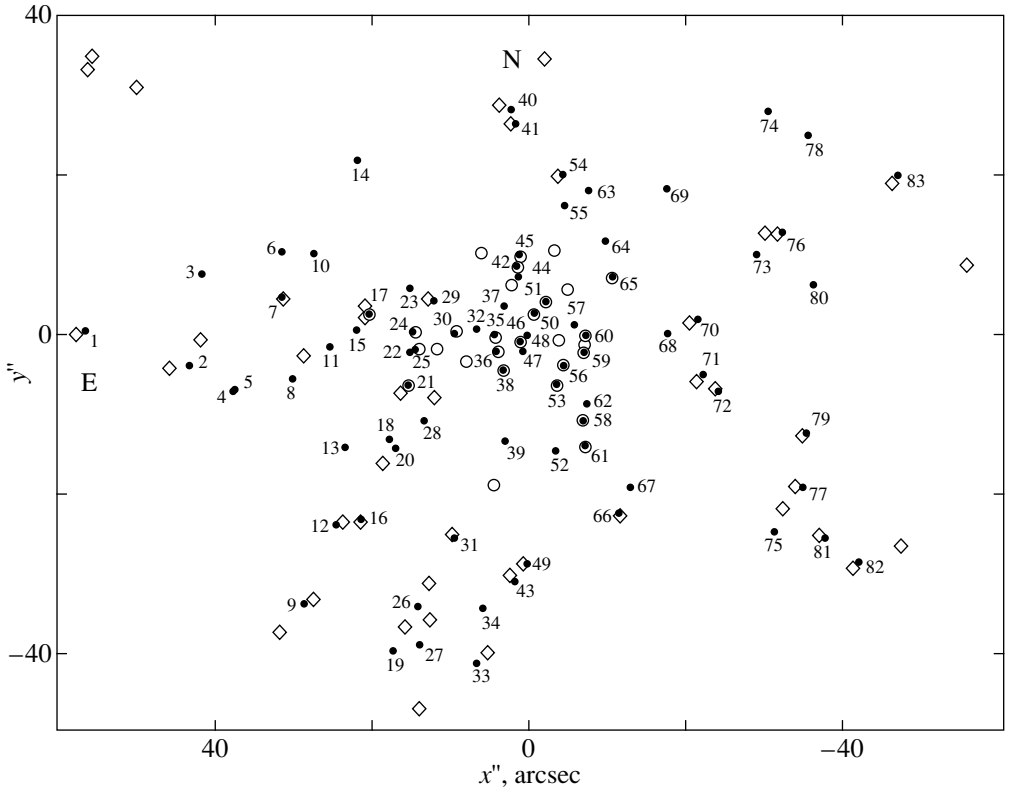

Fig. 2. The identification of stars (1–83) from our list (denoted by dots with the corresponding numbers) with known variables. The stars from the catalog by Clement *et al.* (2001), except V128–155, are indicated by diamonds. The stars from the list by Butler *et al.* (1998), 28 of which are variables V128–155 and two most likely correspond to V83 and V85, are indicated by circles. The differences $\Delta\alpha''$ and $\Delta\delta''$ relative to the coordinates of the M 15 center are used as x'' and y'' of the rectangular coordinate system of the catalog by Clement *et al.* (2001).

We identified a total of 55 of the 83 stars from our list with known variables, while the remaining 28 stars were classified as candidates for new variables in the globular cluster M 15. Their numbers are given in Table 1. This table also presents the coordinates of these stars, which, as was noted above, are the differences $\Delta\alpha''$ and $\Delta\delta''$ relative to the coordinates of the cluster center in arcseconds. To identify new variables (among all of the 83 stars that we discovered), in describing them in the text, the table, and the figures, we added the prefix "ZK" to their numbers.

Table 2 gives corrected coordinates for V128–155. These coordinates are also the differences $\Delta\alpha''$ and $\Delta\delta''$, which may be taken with a sufficient accuracy as the rectangular coordinates (x'', y'') relative to the cluster center in the system of the catalog by Clement *et al.* (2001).

The Classification of New Variables

The basic characteristics of our observations and the achieved accuracy of the (relative) photometry allowed us to reliably establish the fact of light variations in the candidates for variable stars. Unfortunately, however, the total duration of our optical monitoring was not long enough for the same reliable and definite classification of a large number of them. We primarily attribute this to the determination of the subtype of RR Lyrae variables, considering the highest probability of their presence among the discovered new variable stars. At the same time, we do not rule out the erroneous assignment of variables of other types whose periods exceed the duration of each of the two monitoring intervals to the latter. Nevertheless, our quasi-continuous fragments of the light curves make it possible to tentatively estimate the type of the discovered variables from the shape and characteristic features of these curves, the range of brightness variations, etc. This estimate is presented in the column "Type" of Table 1. In addition, this table gives data on the detected brightness variation ΔR, which is not an amplitude value for some of the variables. In designating the different subtypes of RR Lyrae stars, we followed the new system of designations for these subtypes adopted in the catalog by Clement *et al.* (2001): RR0 corresponds to fundamental-mode

Table 1. Data on the 28 new variables in the central region of M 15

N	$\Delta\alpha''$	$\Delta\delta''$	ΔR	Type	N	$\Delta\alpha''$	$\Delta\delta''$	ΔR	Type
ZK3	41.65	7.61	$0\overset{m}{.}20$	RR1?	ZK39	2.91	−13.46	$0\overset{m}{.}28$	RR1?
ZK4	37.66	−7.09	$0\overset{m}{.}45$	RR1?	ZK44	1.21	7.25	$0\overset{m}{.}12$	RR2?
ZK5	37.26	−6.84	$0\overset{m}{.}40$	RR1?	ZK47	0.81	−1.94	$0\overset{m}{.}10$	?
ZK6	31.51	10.34	$0\overset{m}{.}30$	RR0?	ZK52	−3.54	−14.54	$0\overset{m}{.}32$	RR1?
ZK10	27.30	10.25	$0\overset{m}{.}12$	RR2?	ZK55	−4.49	16.33	$0\overset{m}{.}25$	RR2?
ZK11	25.27	−1.47	$0\overset{m}{.}22$	RR1?	ZK62	−7.39	−8.70	$0\overset{m}{.}25$	SX Phe
ZK13	23.29	−14.21	$0\overset{m}{.}30$	RR1?	ZK63	−7.68	18.19	$0\overset{m}{.}28$	RR1?
ZK14	21.82	21.92	$0\overset{m}{.}23$	RR2?	ZK64	−9.75	11.73	$0\overset{m}{.}35$	RR1?
ZK18	17.70	−13.16	$0\overset{m}{.}52$	RR0?	ZK67	−13.04	−19.32	$0\overset{m}{.}30$	RR1?
ZK22	15.27	−2.06	$0\overset{m}{.}42$	RR1?	ZK68	−17.70	0.2	$0\overset{m}{.}20$	SX Phe
ZK23	15.07	5.78	$0\overset{m}{.}52$	RR0?	ZK69	−17.58	18.47	$0\overset{m}{.}30$	RR1?
ZK32	6.65	0.70	$0\overset{m}{.}25$	?	ZK74	−30.51	28.17	$0\overset{m}{.}30$	RR0?
ZK34	5.85	−34.44	$0\overset{m}{.}30$	RR2?	ZK78	−35.53	25.13	$0\overset{m}{.}32$	RR1
ZK37	3.12	3.63	$0\overset{m}{.}20$	RR2?	ZK80	−36.27	6.46	$0\overset{m}{.}40$	RR0?

Note: N are the numbers of the stars from our list classified as candidates for new variables; $\Delta\alpha''$ and $\Delta\delta''$ are the differences in equatorial coordinates relative to the coordinates of the M 15 center (AC 211, epoch 2000.0), which may be taken with a sufficient accuracy as the rectangular (x'', y'') coordinates of the system of the catalog by Clement *et al.* (2001); ΔR is the maximum recorded R-band brightness variation, which is not an amplitude values for some stars; the column "Type" gives a tentative determination of the variability type.

Table 2. Corrected coordinates of the variable stars V128–155 from the catalog by Clement *et al.* (2001)

N	$\Delta\alpha''$	$\Delta\delta''$	N	$\Delta\alpha''$	$\Delta\delta''$	N	$\Delta\alpha''$	$\Delta\delta''$
128	1.03	−0.86	138	3.07	−4.12	148	−3.93	−0.62
129	−7.28	−14.02	139	1.43	8.38	149	2.16	6.20
130	−6.95	−10.71	140	4.15	−0.42	150	5.98	10.25
131	−7.05	−2.23	141	9.23	0.41	151	−7.18	−1.15
132	−7.35	−0.09	142	3.86	−2.11	152	0.92	9.77
133	−5.90	1.30	143	4.32	−18.88	153	−5.05	5.71
134	−4.44	−3.79	144	13.89	−1.81	154	−3.32	10.60
135	−3.68	−6.38	145	14.38	0.31	155	−10.64	7.23
136	−2.24	4.20	146	11.69	−1.81			
137	−0.71	2.52	147	7.91	−3.38			

Note: N are the numbers of the catalogued stars; $\Delta\alpha''$ and $\Delta\delta''$ are the same as in Table 1.

pulsations; RR01 corresponds to a double pulsation mode (in the fundamental tone and the first overtone); and RR1 and RR2 correspond to first- and second-overtone pulsations, respectively.

Although the mean positions of the new variables in the color–magnitude diagram for M 15 cannot be determined from our data, we managed to identify most of them with stars in the catalog from van der Marel *et al.* (2002). It contains photometric data for almost 32 000 stars in the central region of M 15 that was observed with the HST. Therefore, we determined the positions of the following identified new variables in the $V-(B-V)$ diagram constructed from the data of this catalog (Fig. 3): ZK3 (21552), ZK4 (20097), ZK5 (20118), ZK6 (11423), ZK10 (11776), ZK11 (24953), ZK13 (26619), ZK14 (13564), ZK18 (25693), ZK22 (1855), ZK23 (505), ZK34 (27077), ZK37 (3393), ZK39 (8568), ZK44 (2997), ZK47 (5768), ZK52 (10356), ZK55 (2321), ZK62 (10041), ZK64 (4894), and ZK68 (10344). The

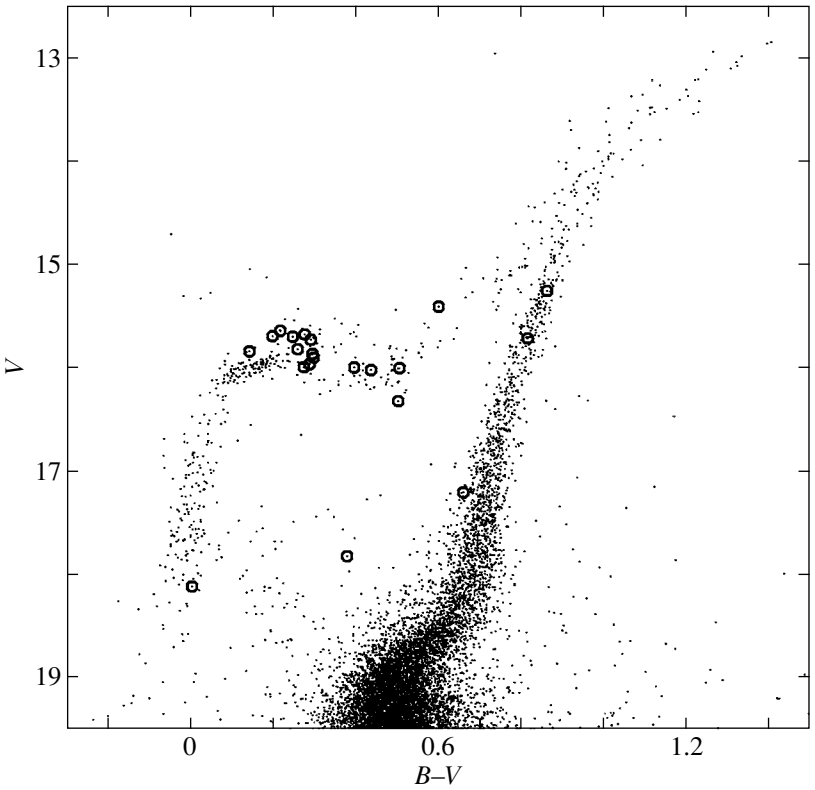

Fig. 3. The $V-(B-V)$ diagram for the central region of M 15 constructed by using the catalog from van der Marel *et al.* (2002). The new variables identified with catalogued stars are indicated by circles.

new variables ZK34 (876), ZK37 (793), ZK39 (784), ZK44 (722), ZK47 (699), ZK52 (511), ZK64 (332), ZK67 (267), ZK68 (210), and ZK80 (46) were also identified with stars of the photometric catalog from Yanny *et al.* (1994), which was compiled from early HST observations. The star numbers from these catalogs are given in parentheses. The identified variables are indicated by circles in Fig. 3. With the exception of five stars (for more detail, see below), the positions of the remaining stars in the diagram are in good agreement with their classification as RR Lyrae variables.

As we see from Table 1, we managed to discover two stars, ZK62 and ZK68, that are, undoubtedly, not RR Lyrae variables. The amplitude and period ($<0\overset{d}{.}08$) of their brightness variations allow us to classify these stars with a high probability as SX Phe variables, especially since, as we see from Fig. 3, ZK62 and ZK68 fall into the region of blue stragglers. Details on ZK62 and ZK68 will be presented in a separate publication. Note that, currently, only one variable of this type is known in M 15. Recently, Jeon *et al.* (2001a) detected it at a distance of several arcminutes from the cluster center. Thus, given the results of our study, the number of SX Phe stars discovered in the globular cluster M 15 reached three.

In contrast to ZK62 and ZK68, we failed to determine the variability type of the other two variables, ZK32 and ZK47. As follows from the photometric data of van der Marel *et al.* (2002), the latter proved to be among the red-giant-branch (RGB) stars above the horizontal branch in the $V-(B-V)$ diagram, while according to the data of Yanny *et al.* (1994), it is located in the $V-(V-I)$ diagram above (by more than $0\overset{m}{.}5$) the blue part of the horizontal branch. ZK10 and ZK39 also proved to be among the RGB stars in Fig. 3. However, the latter, according to the data of Yanny *et al.* (1994), is located near the horizontal branch, while in Fig. 3 it lies below this branch by more than $1\overset{m}{.}0$. Therefore, it may well be that we identified it erroneously in the catalog by van der Marel *et al.* (2002), because the difference in coordinates between it and the star identified in the catalog was larger than that for other variables.

Note, in addition, that star 48, i.e., the object AC 211, in our images exhibited complex brightness variations. On the first night of our observations, they appeared periodic, with $\Delta R \approx 0\overset{m}{.}1$ and a period on the order of $0\overset{d}{.}1$, while on the second night these variations manifested themselves in the relatively slow brightness increase by $\Delta R \approx 0\overset{m}{.}2$, only with a hint at

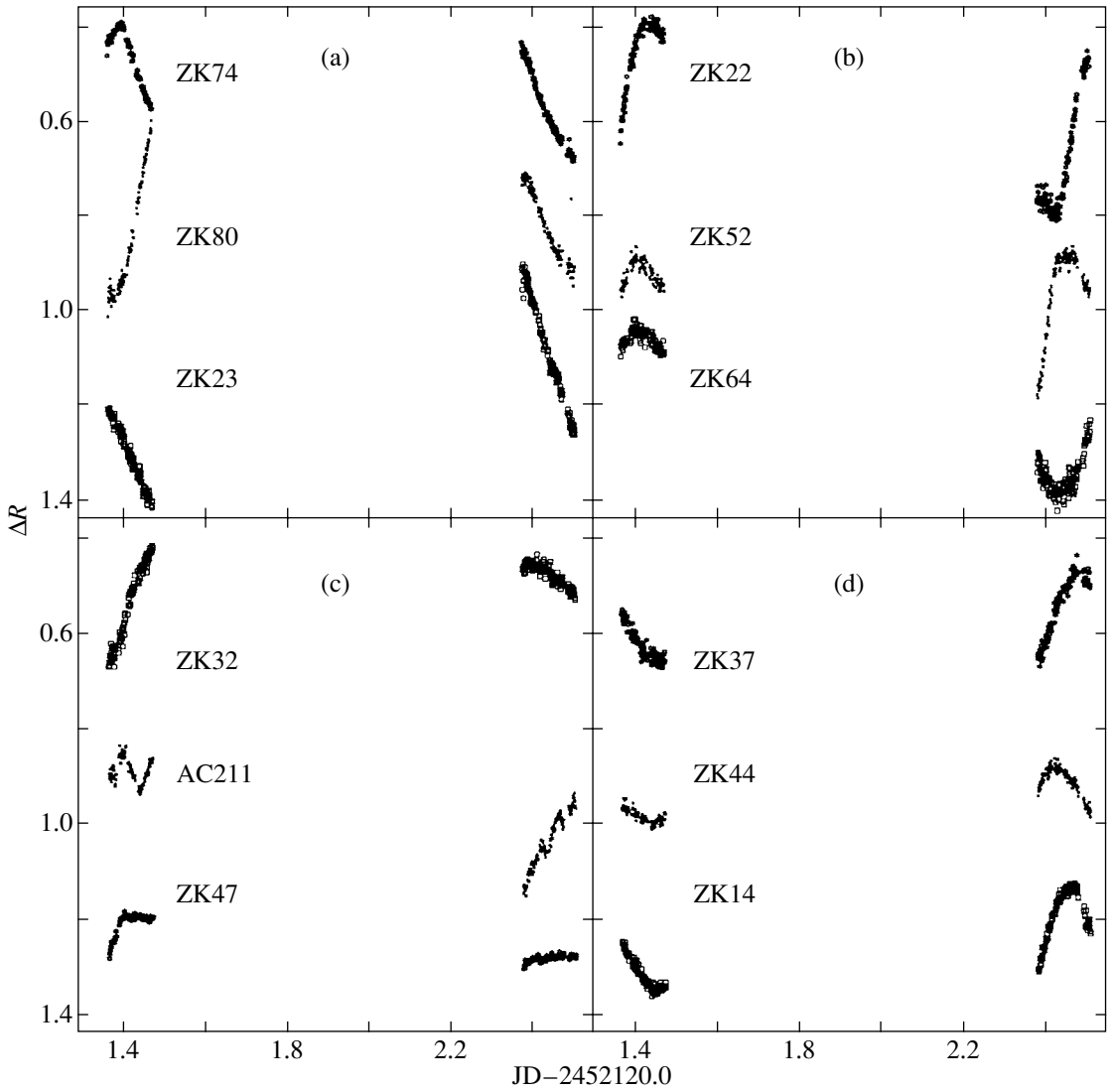

Fig. 4. An illustration of the classification by types of new variables based on their light curves. Three light curves for stars of each of the subtypes (a) RR0, (b) RR1, and (d) RR2 are shown as an example. (c) The light curves for the two stars whose variability type could not be determined; also shown here is the light curve for the object AC 211. For convenience, the light curves were arbitrarily displaced along the vertical axis (relative R magnitudes).

faster brightness oscillations (at the photometry error level).

Our preliminary classification by types of new variables is illustrated by examples of light curves for twelve of these stars in Fig. 4. Figures 4a, 4b, and 4d show the light curves of RR0, RR1, and RR2 stars, respectively. The light curves of the stars mentioned above whose variability type could not be determined are shown in Fig. 4c. This figure also shows the light curve for the object AC 211. The star numbers are indicated near the corresponding curves. For convenience, we arbitrarily displaced the light curves along the vertical axis (ΔR). Formally, there are no RR01 stars among the candidates for new variables. However, this is not an actual fact. It will be possible to reliably establish whether particular stars are of the RR01 subtype only after the determination of their periods. As we see from the figure, we conditionally classified the stars in which the recorded brightness variation allows the amplitude to be determined and, at the same time, ΔR is generally within $0^m.25$ and the shape of the light curve is most likely nearly sinusoidal as being of the RR2 subtype. In this case, there is reason to believe that the second interval of our observations (its duration is $0^d.128$ compared to the duration $0^d.107$ of the first interval of our observations) spans about half the pulsation period of the RR2 stars under discussion; i.e., their periods are $<0^d.3$. The stars classified as RR1 exhibit brightness (including amplitude) variations larger than $0^m.25$ and an indis-

tinct asymmetry in the light curves. For some of them, the pulsation periods can also be $<0^d.3$, as those for the stars classified as RR2. The detected brightness variations in RR0 stars proved to be, on average, even larger than those in RR1 stars. In addition, particular characteristic features, such as an asymmetry, a sharp peak, etc., showed up in their light curves. Nevertheless, in several cases, the determination of the subtypes of new variables is controversial or conditional.

3. COMPARATIVE CHARACTERISTICS OF VARIABLE STARS IN THE CENTRAL AND OUTER PARTS OF M 15

Almost ten years ago, Stetson (1994) performed multicolor photometry of stars in the central part of M 15 by using a large number of CCD images with a subarcsecond angular resolution and an improved procedure of stellar photometry. He found several important changes in the stellar composition that were observed in the cluster region at $r < 30''$, especially in its densest part ($r < 12''$), and showed up in the color–magnitude diagram. In particular, these changes manifested themselves in a significant growth of the population of stars that fell into the region in the diagram between the turnoff point and the horizontal branch, as well as in an apparent reddening of the horizontal branch itself. It would be quite natural to assume that the effects resulting in the detected changes in the color–magnitude diagram could also be reflected on the population of variables located in the same part of the cluster and falling into the same region of the diagram. One of the possible changes is quite a natural and expected result of the dynamical effects in the central part of M 15 or, more specifically, an increase in the number of variables associated with binary stars and blue stragglers. This is confirmed by the study of the central parts of post-core-collapse globular clusters. In particular, in NGC 6397, Kaluzny and Thompson (2002) discovered several variables, among which are eclipsing, cataclysmic, and SX Phe stars. We also managed to discover two SX Phe variables. However, taking into account one of the above results of Stetson (1994), one might expect the actual number of such stars in the central part of M 15 to be significant. Whether any changes could affect the population of RR Lyrae variables proper is quite a different matter.

A preliminary (including frequency) analysis of the light curves indicates that there may be a significant fraction of stars with periods $<0^d.3$ among the new variables classified as RR1 and RR2 and located in the cluster region at $r < 35''$. The most realistic estimation gives a lower limit on the order of seven (of 15), i.e., more than 40%. We noticed that only five (less than 20%) among the stars of the above

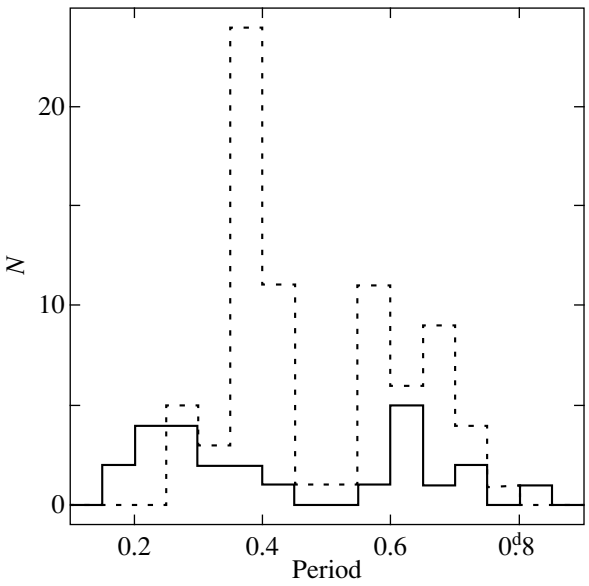

Fig. 5. The period distributions (histograms) of RR Lyrae variables in the globular cluster M 15. The solid and dotted lines indicate the histograms constructed for stars of the central cluster region ($r < 35''$) and for the remaining stars, respectively.

subtypes in the catalog by Clement *et al.* (2001) with measured periods and located at distances $r > 35''$ from the center of M 15 (i.e., with the exception of V128–155, V83, and V85) satisfy this condition; none of them has a period $<0^d.27$. However, the fraction of such stars (more than 60%) significantly increases among the variables of the above subtypes located in the central region of M 15 (i.e., among V128–155, V83, and V85). Almost half of them have periods $<0^d.27$. The change in the ratio of the numbers of RR Lyrae stars pulsating with periods $<0^d.3$ and those pulsating in the fundamental tone (RR0) proves to be more significant: 80% in the central region compared to 15% outside it. Yet another significant difference is that only two (of the 25 sample stars) among the variables in the central part of the cluster have periods in the range $0^d.35$–$0^d.40$, while there are almost a third of such variables of their total number, more specifically, 24 of the 76 sample stars, in the outer parts of the cluster. A similar change probably also pertains to the numerous population of RR01 stars in the outer parts of the cluster.

Based on the data from Butler *et al.* (1998) and from the catalog by Clement *et al.* (2001) analyzed above, we constructed the histograms (Fig. 5) that clearly show the described differences between the period distributions of the RR Lyrae variables located in different parts of M 15. The number of stars in the outer regions of the cluster allows them be separated into three subpopulations (equal in number

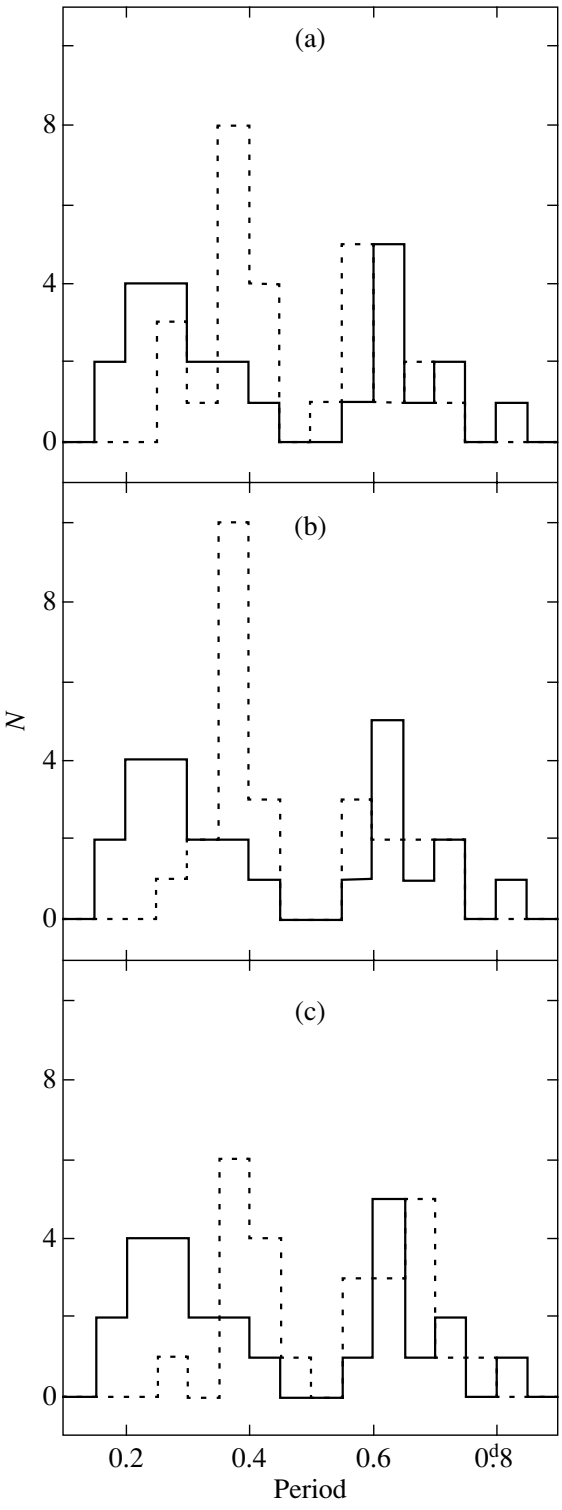

Fig. 6. Comparison of the period distributions (histograms, dotted lines) of RR Lyrae variables located in annular zones at difference distances from the center of M 15 ($r > 175''$ (a), $90'' < r < 175''$ (b), and $35'' < r < 90''$ (c)) with a similar histogram (solid line) constructed for the same variables in the central region ($r < 35''$) of the cluster. Each zone, except $r > 175''$ (26 stars), contains 25 stars.

to the population in the central part) located in annular zones at different distances from the center of M 15: 26 stars with $r > 175''$ and 25 stars each with $90'' < r < 175''$ and $35'' < r < 90''$. This separation makes it possible not only to analyze the period distributions of variables at different distances from the center of M 15 in its outer regions but also to compare each of them with the distribution of stars in the central region. The number of stars in each sample is the same. The derived histograms of the corresponding distributions are represented by dotted lines in Fig. 6 for stars at different distances from the center of M 15. As in Fig. 5, the solid line indicates the period distribution of the variables in the central region. We see from a comparison of the histograms that there is no clear evidence of any systematic differences between the period distributions of the RR Lyrae variables in the three outer parts of M 15 and that each of them significantly differs from the period distribution in the central part. This suggests that the changes (if they are real) occur almost abruptly somewhere at $r < 35''$, where the star density significantly increases and where Stetson (1994) found apparent changes in the color–magnitude diagram of the cluster.

Undoubtedly, the size of the sample of variables in the central region of the cluster (25 stars) is much smaller than the size of their sample (76 stars) in the remaining part of M 15 and is not yet sufficient to draw ultimate and reliable conclusions. However, the presented differences are too striking to be left unnoticed. In addition, a preliminary analysis of our observations of the new variables reveals the same tendency. Of course, we cannot rule out the possibility that the differences being discussed are attributable to selection effects. One of these effects may stem from the fact that, historically, the variables in the outer parts of M 15 were studied mostly by using the methods of photographic photometry of these stars. In contrast, the data on the variables in the central part of the cluster were obtained mainly in the past decade by using much more sophisticated and efficient image recording and reduction techniques. This imbalance between the possibilities of observational studies could lead to the fact that some of the low-amplitude (and, hence, on average, shorter-period) RR Lyrae variables in the outer parts of M 15 have proven to be simply undetectable so far. At first glance, this assumption seems quite justified. However, it should be borne in mind that, while studying several tens of known RR Lyrae stars in a wide cluster field using a CCD array, Silbermann and Smith (1995) discovered only one such low-amplitude variable of this type, namely, V113.

With the addition of data on the periods, light curves, and positions in the color–magnitude diagram of our discovered stars and the already known

but as yet unstudied variables in the central part of the cluster, the sizes of the samples of variables located in the outer and central regions of M 15 will be comparable and quite sufficient for a more substantive analysis.

CONCLUSIONS

We carried out two sets of optical monitoring of the central region in the globular cluster M 15 with a subarcsecond angular resolution and a total duration of about six hours using the 1.5-m telescope. As a result, we obtained more than two hundred R-band images of the cluster. The reduction of our data using the optimal image-subtraction method of Alard and Lupton (1998) revealed brightness variations in 83 stars. Twenty eight of them are candidates for new variables, which constitute the largest population of new variables discovered in one research work in the past 50 years of the study of variable stars in M 15. Apart from the two stars whose variability type could not be determined, the other two stars are likely to be SX Phe variables, while the remaining stars were tentatively classified as RR Lyrae variables. Published data on the variables of this type located in the central region of the globular cluster and a preliminary analysis of our results show that in the densest part ($r < 35''$) of the cluster, the maximum of the period distribution for first- and second-overtone pulsating (RR1 and RR2) stars probably shifts toward shorter periods. In addition to an increase in the fraction of these stars pulsating with periods $<0\overset{d}{.}3$, there is a deficiency of stars in the range of periods $0\overset{d}{.}35-0\overset{d}{.}40$ compared to the period distribution for the population of variables in the farther outer parts of M 15. The ratio of the number of variables with periods $<0\overset{d}{.}3$ to the number of variables pulsating in the fundamental tone (RR0) also changes. We found and corrected the error of transforming the coordinates of variables V128–155 to the coordinate system of the catalog by Clement *et al.* (2001).

ACKNOWLEDGMENTS

We are grateful to the referee, N.N. Samus', for helpful remarks.

REFERENCES

1. C. Alard and R. H. Lupton, Astrophys. J. **503**, 325 (1998).
2. M. Auriere and J. P. Cordoni, Astron. Astrophys., Suppl. Ser. **46**, 347 (1981).
3. M. Auriere, O. Le Fevre, and A. Terzan, Astron. Astrophys. **138**, 415 (1984).
4. R. F. Butler, A. Shearer, R. M. Redfern, *et al.*, Mon. Not. R. Astron. Soc. **294**, 379 (1998).
5. C. M. Clement, A. Muzzin, Q. Dufton, *et al.*, Astron. J. **122**, 2587 (2001).
6. F. R. Ferraro and F. Paresce, Astron. J. **106**, 154 (1993).
7. J. Gerssen, R. P. van der Marel, K. Gebhardt, *et al.*, Astron. J. **124**, 3270 (2002).
8. J. Gerssen, R. P. van der Marel, K. Gebhardt, *et al.*, Astron. J. **125**, 376 (2003).
9. W. E. Harris, Astron. J. **112**, 1487 (1996).
10. Y.-B. Jeon, S.-L. Kim, H. Lee, and M. G. Lee, Astron. J. **121**, 2769 (2001a).
11. Y.-B. Jeon, H. Lee, S.-L. Kim, and M. G. Lee, Int. Bull. Var. Stars **5189**, 1 (2001b).
12. Z. I. Kadla, A. N. Gerashenko, A. A. Strugatskaya, and N. V. Yablokova, Izv. GAO **205**, 114 (1988).
13. J. Kaluzny and I. B. Thompson, astro-ph/0210626 (2002).
14. R. P. van der Marel, P. Gebhardt, *et al.*, Astron. J. **124**, 3255 (2002).
15. H. Sawyer Hogg, Publ. David Dunlap Obs. **3**, 6 (1973).
16. N. A. Silbermann and H. A. Smith, Astron. J. **110**, 704 (1995).
17. P. B. Stetson, Publ. Astron. Soc. Pac. **106**, 250 (1994).
18. B. Yanny, P. Guhathakurta, J. N. Bahcall, and D. P. Schneider, Astron. J. **107**, 1745 (1994).

Translated by V. Astakhov

Astronomy Letters, Vol. 29, No. 9, 2003, pp. 612–620. Translated from Pis'ma v Astronomicheskiĭ Zhurnal, Vol. 29, No. 9, 2003, pp. 643–648.

Peculiarities of the UV Continuum Energy Distribution for T Tauri Stars

A. S. Kravtsova* **and S. A. Lamzin****

Sternberg Astronomical Institute, Universitetskii pr. 13, Moscow, 119992 Russia

Abstract—In the UV spectra of BP Tau, GW Ori, T Tau, and RY Tau obtained with the Hubble Space Telescope, we detected an inflection near 2000 Å in the $F_\lambda^c(\lambda)$ curve that describes the continuum energy distribution. The inflection probably stems from the fact that the UV continuum in these stars consists of two components: the emission from an optically thick gas with $T < 8000$ K and the emission from a gas with a much higher temperature. The total luminosity of the hot component is much lower than that of the cool component, but the hot-gas radiation dominates at $\lambda < 1800$ Å. Previously, other authors have drawn a similar conclusion for several young stars from low-resolution IUE spectra. However, we show that the short-wavelength continuum is determined from these spectra with large errors. We also show that, for three of the stars studied (BP Tau, GW Ori, and T Tau), the accretion-shock radiation cannot account for the observed dependence $F_\lambda^c(\lambda)$ in the ultraviolet. We argue that more than 90% of the emission continuum in BP Tau at $\lambda > 2000$ Å originates not in the accretion shock but in the inner accretion disk. Previously, a similar conclusion was reached for six more classical T Tau stars. Therefore, we believe that the high-temperature continuum can be associated with the radiation from the disk chromosphere. However, it may well be that the stellar chromosphere is its source. © *2003 MAIK "Nauka/Interperiodica".*

Key words: *stars; individual: BP Tau, GW Ori, RY Tau, LkHα 264, TW Hya, T Tau; T Tauri spectra stars; disk accretion.*

INTRODUCTION

Classical T Tauri stars (CTTSs) are young stars with masses $\leq 2M_\odot$ at the stage of contraction toward the main sequence. In most CTTSs, $T_{\rm eff}$ does not exceed 5000 K, but the intensity of their radiation at wavelengths shorter than 3100 Å is fairly high. This fact was first revealed by observations from the Copernicus satellite (De Boer 1977) and then confirmed by observations from the IUE satellite (Imhoff and Appenzeller 1987).

In 1986, Herbig and Goodrich drew attention to the fact that the UV continuum energy distribution for T Tau, RY Tau, and FK Ser has the following peculiarity: whereas the long-wavelength UV (up to about 1800 Å) continuum is an extension of the so-called veiling optical continuum, the shorter-wavelength continuum is almost flat. The UV radiation from CTTSs was then believed to be produced by thick chromospheres. Therefore, Herbig and Goodrich (1986) decided that the long-wavelength UV continuum originated in the lower chromospheres of CTTSs, while the short-wavelength UV continuum originated in their upper chromospheres and/or transition layers. This conclusion was drawn from the analysis of low-resolution ($\Delta\lambda \simeq 6$ Å) IUE spectra. Therefore, the possibility that the observed UV continuum is actually a blend of many low-intensity emission lines could not be ruled out.

At present, the CTTS activity is generally believed to be attributable to mass accretion from a protoplanetary disk onto a central star with a large-scale magnetic field more than 1 kG in strength. It is assumed that the magnetic field of the star stops the disk at some distance from its surface and that the disk material freezes in magnetic field lines and, sliding along them, falls to the star, accelerating to a velocity of $\sim$300 km s^{-1}. Near the surface, the material decelerates in an accretion shock whose radiation accounts for the observed line and continuum emission in CTTSs (see the review by Najita *et al.* (2000) and references therein). The accretion-shock continuum radiation consists of two components whose temperatures differ by several times (Calvet and Gullbring 1998), which could, in principle, explain the effect detected by Herbig and Goodrich (1986). However, we show below that, actually, this cannot be done.

On the other hand, a quantitative analysis of the UV spectra for six CTTSs (T Tau, RY Tau, DR Tau, DS Tau, DG Tau, and TW Hya) indicates that the bulk (>90%) of their emission continuum is formed outside the accretion shock (Kravtsova

*E-mail: kravts@sai.msu.ru
**E-mail: lamzin@sai.msu.ru

1063-7737/03/2909-0612$24.00

and Lamzin 2002a, 2002b; Kravtsova 2003). It thus follows that the magnetic field in the CTTSs under study does not destroy the inner disk regions and that the disk reaches the stellar surface. In this case, the bulk of the accreted material settles in the equatorial plane of the star and only a small fraction of it flows through the magnetosphere and the accretion shock. Here, we also reach a similar conclusion for BP Tau, which suggests that two-flow accretion (through the disk and the magnetosphere) is characteristic of all CTTSs.

Therefore, we discuss how to explain the flat continuum detected by Herbig and Goodrich in terms of the two-flow accretion model. We show that, although the conclusion about the presence of a flat, short-wavelength continuum drawn from the analysis of IUE spectra is not reliable, the abrupt change in the slope of the UV continuum near 2000 Å takes place for at least four CTTSs: BP Tau, GW Ori, T Tau, and RY Tau.

OBSERVATIONAL DATA

The two analyzed low-resolution spectra for BP Tau were obtained on January 12, 2002, with the Space Telescope Imaging Spectrograph (STIS) as part of the program ID 9081. The first spectrum was obtained in the wavelength range from 1600 to 3150 Å with an exposure time of 1 min; 8 min later, a 30-min exposure of the second spectrum that covered the range from 1160 to 1700 Å began. Intermediate-resolution spectra for T Tau were obtained with the STIS on September 8, 2000 (five spectra in the range 1165–1700 Å; the program ID 8157), and February 21, 2001 (three spectra in the range 2300–3100 Å; the program ID 8627). We took all of the HST/STIS spectra from the HST archival database (http://archive.stsci.edu/hst/ target_descriptions.html) and processed them by using the IRAF v2.11 (http://iraf.noao.edu/iraf) and STSDAS/TABLES v2.02 (http://ra.stsci.edu/ STSDAS) software packages. We used the standard techniques described in Chapter 21 of the HST Data Handbook (http://www.stsci.edu/documents/datahandbook.html).

The low-resolution UV spectra of GW Ori, T Tau, and RY Tau used below were also obtained with the STIS and were described previously (Kravtsova and Lamzin 2002b). In addition, we used the low-resolution UV spectra of BP Tau obtained from the IUE satellite in the 1980s. These spectra were taken from the INES database (http://ulda.inasan.rssi.ru) and used without further processing.

THE INFLUENCE OF SPECTRAL RESOLUTION ON THE SHAPE OF THE UV CONTINUUM IN CTTSs

As was pointed out in the Introduction, Herbig and Goodrich (1986) found that the slope of the $F_\lambda^c(\lambda)$ curve, which describes the UV continuum energy distribution for T Tau, RY Tau, and FK Ser, appreciably changed near 2000 Å. Later, an inflection in the $F_\lambda^c(\lambda)$ curve near 2000 Å was also detected in the IUE spectra of the stars LkHα 264 (Costa *et al.* 1999) and TW Hya (Costa *et al.* 2000). Moreover, judging by the atlas of IUE spectra (Gomez de Castro and Franqueira 1997), a large number of CTTSs exhibit a similar feature.

We emphasize that, in all of these cases, we judge the presence of an inflection from the IUE spectra with a resolution $\Delta\lambda \simeq 6$ Å ($R \simeq 250$). However, since there are many lines in the UV spectra of CTTSs, the possibility that we actually take a blend of many weak emission lines for the continuum cannot be ruled out a priori. Currently, the HST archive contains high-resolution spectra only for a few CTTSs; some of them can be used to estimate the influence of spectral resolution on the accuracy of determining the UV continuum level.

T Tau, for which intermediate-resolution ($R \simeq 24\,000$) spectra are available, is the most suitable star for this purpose. At the same time, the spectra of this star in the range 2300–3100 Å were obtained six months after the spectra in the range 1150–1700 Å. Therefore, these data cannot be used to study the UV continuum energy distribution of T Tau. Since the quality of the spectra is rather low, for clarity, the lower panels of Fig. 1 show not the original spectra but those smoothed over 50 points, which corresponds to a resolution $\Delta\lambda \simeq 0.3$ Å. Based on these spectra, we determined the continuum level in the selected regions; the values of F_λ^c are indicated by squares in the middle and upper panels of Fig. 1.

The upper and middle panels of Fig. 1 show the spectra that were obtained from the original spectra by smoothing them with a Gaussian with FWHMs of 3 and 1.2 Å, respectively. In doing so, we found how the original spectra would appear if they were obtained from the IUE satellite (upper panel) and with the STIS at a low ($R \sim 1500$) resolution (middle panel). We see from the figure that, because of the low quality of the original spectra, the location of the continuum was determined inaccurately, particularly at short wavelengths. At the same time, the pattern of the dependence $F_\lambda^c(\lambda)$ is determined confidently enough to judge whether the continuum can be drawn using low-resolution spectra. At short wavelengths, the low-resolution STIS spectra allow

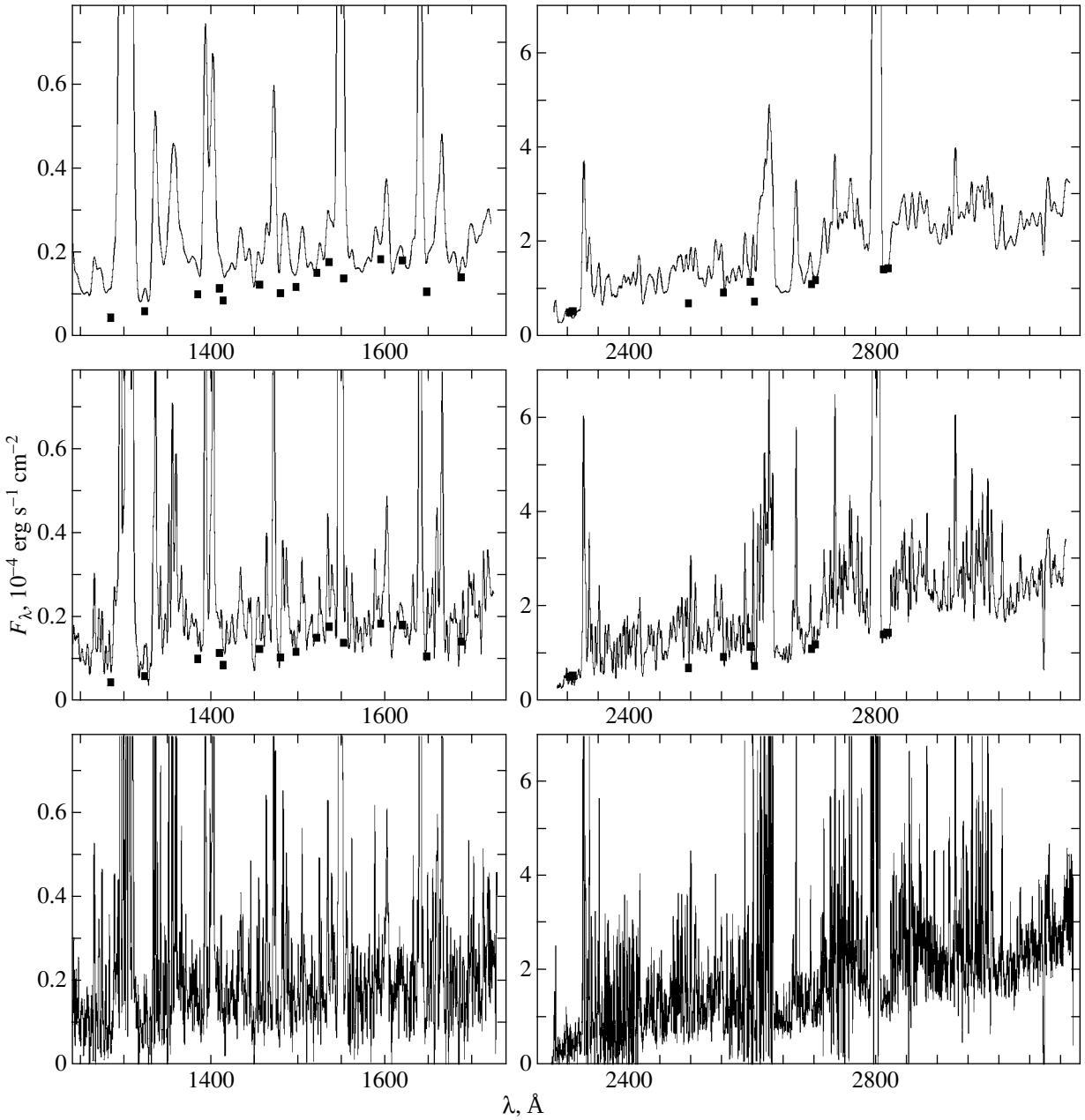

Fig. 1. The UV spectra of T Tau obtained from the original HST/STIS spectra by smoothing: with a moving average over 50 points (lower row), a Gaussian with an FWHM of 1.2 Å (middle row), and a Gaussian with an FWHM of 3 Å (upper row).

us to determine the continuum level with a reasonable accuracy, while the superposition of emission lines in the IUE spectra produces a pseudocontinuum at $\lambda < 1500$ Å whose intensity is appreciably higher than that of the actual continuum. At $\lambda > 2300$ Å, even the IUE spectra allow the shape of the $F_\lambda^c(\lambda)$ curve to be judged with confidence.

Thus, we believe that the conclusion about the presence of an inflection point in the $F_\lambda^c(\lambda)$ curve may be considered reliable if it was drawn from the low-resolution STIS spectra. However, it would be premature to draw a similar conclusion from the IUE spectra.

ANALYSIS OF THE UV CONTINUUM ENERGY DISTRIBUTION USING LOW-RESOLUTION STIS SPECTRA

Figure 2 shows the observed low-resolution STIS spectrum of BP Tau. First, we determined the continuum level in several parts of the stellar spectrum; the corresponding points are indicated in

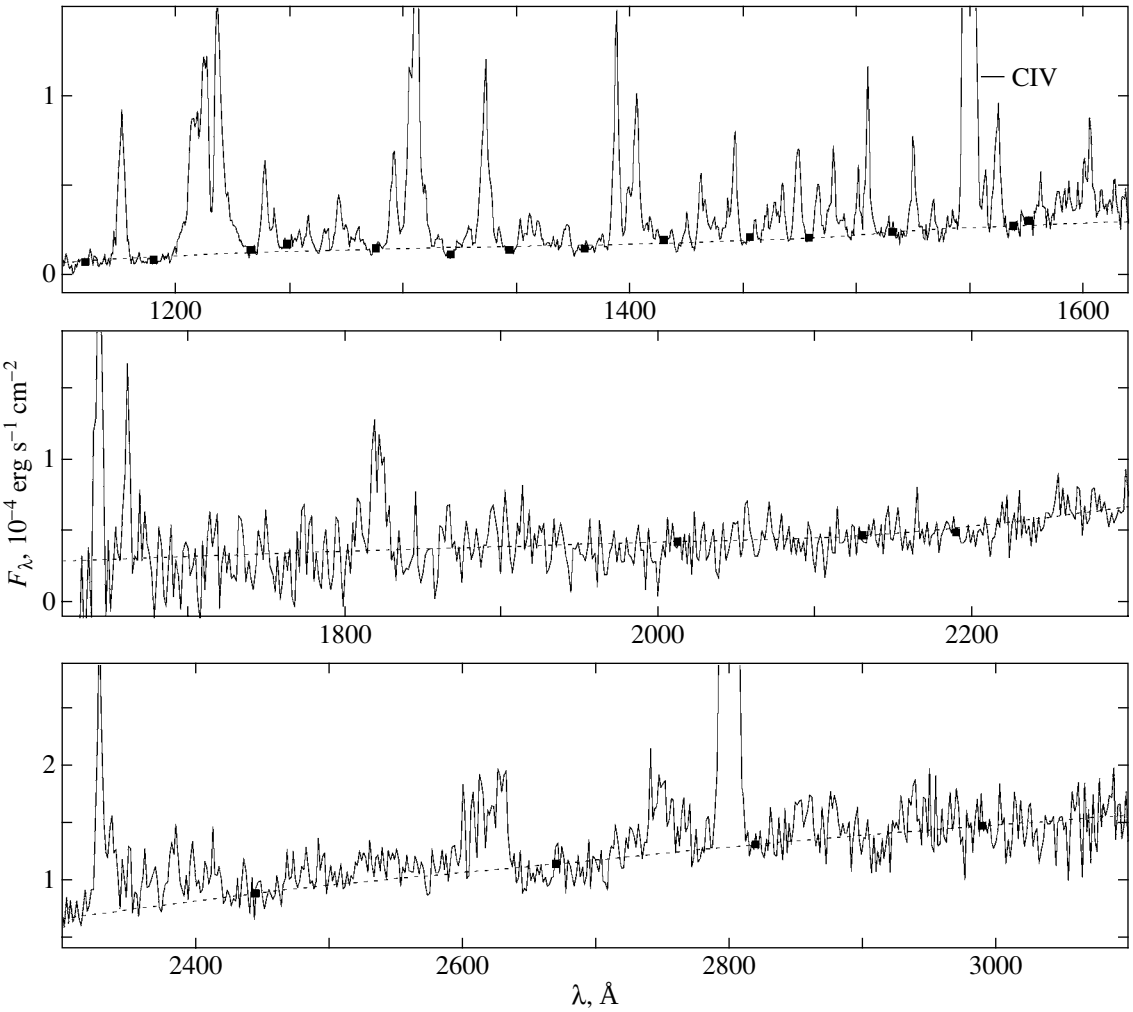

Fig. 2. The analyzed spectrum of BP Tau. The points at which the continuum level (dashed line) was determined are marked by squares.

the figure by squares. We could not fit the set of these points by a single curve and did the following. Using the least squares method, we drew two cubic parabolas through the points: the first and second parabolas were drawn through the points of the short-wavelength ($\lambda < 1570$ Å) and long-wavelength ($\lambda > 2000$ Å) spectra. Since the two parabolas virtually coincided when extrapolated to the range from 1600 to 2100 Å, the resulting curve was taken as the continuum level for BP Tau (dashed line).

We corrected the continuum energy distribution determined in this way for interstellar extinction with various values of A_V. Our results are presented in Fig. 3: for the standard extinction law (left panel) with $R_V \equiv A_V/E_{B-V} = 3.1$ and for the anomalous dependence $A_\lambda(\lambda)$ (right panel) with $R_V = 5.0$ that is characteristic of some stars in Taurus (Mathis 1990). The lower curve in both panels represents the observed energy distribution, and the upper curves represent the distribution corrected for interstellar extinction with the values of A_V indicated near the curves.

Because of the presence of a local maximum in the $A_\lambda(\lambda)$ curve for the interstellar medium near 2200 Å (Mathis 1990), there is a small dip in the observed spectrum of BP Tau in this region. If we take an excessively large value for A_V, then the dip will turn into a hump, which allows the upper limit for the interstellar extinction toward the star to be estimated (for more detail, see Kravtsova and Lamzin (2002b) and Kravtsova (2003)). It follows from Fig. 3 that at $R_V = 3.1$ and 5.0, the hump appears for $A_V > 0\overset{m}{.}4$ and $A_V > 0\overset{m}{.}6$, respectively. Assuming the standard interstellar extinction law, Gullbring *et al.* (1998) found from the optical spectra of BP Tau that $A_V = 0\overset{m}{.}51$. Thus, we believe that the actual value of A_V is close to $0\overset{m}{.}5$.

A characteristic feature of all of the $F_\lambda^c(\lambda)$ curves

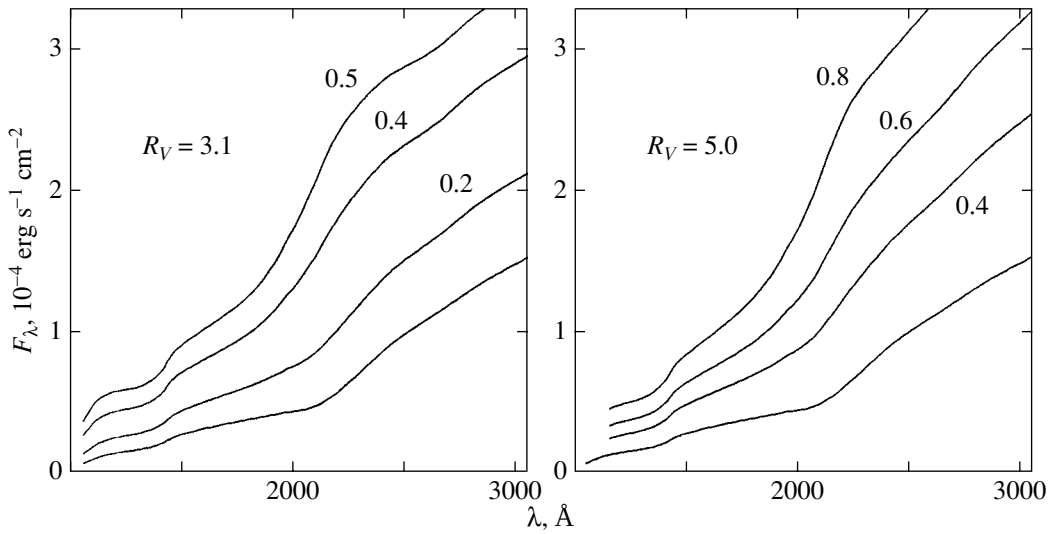

Fig. 3. The UV continuum energy distribution for BP Tau: the observed distribution (lower curve) and the distribution corrected for interstellar extinction with the indicated values of A_V. The left and right panels correspond to the interstellar extinction curves with $R_V = 3.1$ and 5.0, respectively.

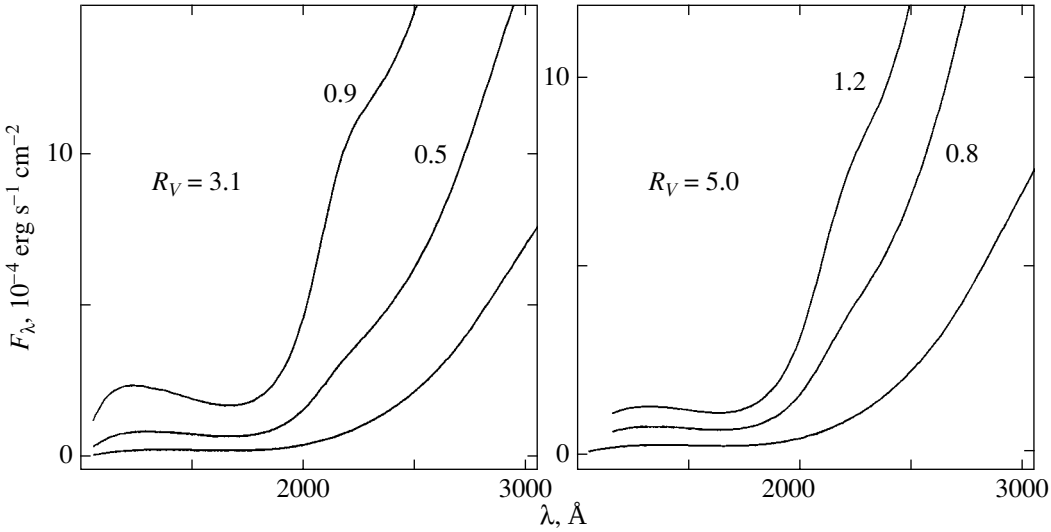

Fig. 4. Same as Fig. 3 for GW Ori.

shown in Fig. 3 is the presence of an inflection near $\lambda \simeq 2000$ Å; i.e., the stellar spectrum exhibits the feature detected by Herbig and Goodrich (1986) for other stars using IUE spectra. Significantly, this conclusion for BP Tau does not depend on the existing uncertainty in the interstellar extinction value and law.

The low-resolution STIS spectrum of GW Ori also exhibits a similar feature. Previously (Kravtsova and Lamzin 2002b), we found that $A_V \leq 0^m.6$ for this star at $R_V = 3.1$. As in the case of BP Tau, this feature is not related to the distortion of the spectrum by interstellar extinction: this can be seen from Fig. 4, which shows the observed continuum energy distribution and the distributions corrected for extinction with various values of A_V for $R_V = 3.1$ (left panel) and $R_V = 5.0$ (right panel).

Analyzing the low-resolution STIS spectra of T Tau and RY Tau, we previously (Kravtsova and Lamzin 2002b) noted that the continuum of these stars appears almost flat at $\lambda < 1700$ Å. We were not completely sure of this because of the low-signal-to-noise ratio in this spectral range. However, judging from the above paper, inflections are undoubtedly present in the $F_\lambda^c(\lambda)$ curves for these stars near 2000 Å. Thus, we confirm the conclusions of Herbig

and Goodrich (1986) that the UV continuum of T Tau and RY Tau has two components. Note, incidentally, that judging by Fig. 1 from this paper, the continuum of T Tau at $\lambda < 1700$ Å is not flat.

To summarize, we may say that the $F_\lambda^c(\lambda)$ curve abruptly changes its slope near 2000 Å for at least four CTTSs (BP Tau, GW Ori, T Tau, and RY Tau). This behavior probably implies that the short-wavelength UV continuum in these stars originates in a region that is much hotter than the formation region of the continuum at $\lambda > 2000$ Å.

DISCUSSION

Currently, the emission continuum of CTTSs is generally believed to originate in an accretion shock (see the review by Najita *et al.* (2000) and references therein). In general, there are three shock-related sources of the continuum: the preshock H II region, the postshock cooling gas, and, finally, the shock-heated part of the the stellar surface. According to Calvet and Gullbring (1998), at a density of the infalling gas $\rho_0 < \rho_{cr} = 3 \times 10^{-11}$ g cm^{-3}, which is characteristic of CTTSs, the post- and preshock regions are optically thin in the Balmer continuum. Therefore, the radiation from the transition layer between the accretion shock and the outer stellar layers mainly contributes to the UV continuum of the shock.

The effective temperature of the transition layer $T_{\rm eff}$ can be estimated by taking into account the fact that the thickness of the post- and preshock regions at $\rho_0 < \rho_{cr}$ is much smaller than the stellar radius (Lamzin 1995, 1998). Half of the accretion-shock-emitted energy then falls on the star and

$$\sigma T_{\rm eff}^4 = \sigma T_*^4 + \frac{1}{2}\rho_0 V_0 \frac{V_0^2}{2}. \quad (1)$$

Here, T_* is the effective temperature of the star and V_0 is the preshock gas velocity. Since T_* is appreciably lower than $T_{\rm eff}$,

$$T_{\rm eff} \simeq \left(\frac{\rho_0 V_0^3}{4\sigma}\right)^{1/4} \quad (2)$$

$$\simeq 7800\left(\frac{\rho_0}{2\times 10^{-11}}\right)^{1/4}\left(\frac{V_0}{350}\right)^{3/4} \text{ K},$$

a numerical estimate can be obtained if the density and velocity are given in g cm^{-3} and km s^{-1}, respectively.

Although the spectrum of the transition layer must differ from the blackbody spectrum, one might expect the continuum intensity at $\lambda < 2500$ Å for $\rho_0 < 3 \times 10^{-11}$ g cm^{-3} to exponentially decrease toward shorter wavelengths, because the maximum of the blackbody curve occurs at a wavelength $\lambda_{\rm max} \simeq 2900(T_{\rm eff}/10^4)$ Å. The presence of an inflection in the $F_\lambda^c(\lambda)$ curve in the spectra of BP Tau, GW Ori, T Tau, and RY Tau at $\lambda \simeq 2000$ Å implies that the short-wavelength UV continuum of these stars originates outside the transition layer, in a region with a temperature much higher than $T_{\rm eff}$.

If the UV continuum of CTTSs originates in an accretion shock, then it would be reasonable to assume that the excess hot continuum is due to the radiation from an optically thin gas in the preshock H II region and/or in the postshock cooling gas. However, computations probably rule out this possibility. This can be seen from Fig. 5, in which the spectrum of BP Tau is compared with the accretion-shock continuum computed by Gullbring *et al.* (2000). In this paper, the observed spectrum of BP Tau was assumed to be a superposition of the photospheric radiation from a K5 V star and three accretion-shock-related components. Our figure is Fig. 1 from the paper by Gullbring *et al.* (2000), from which the curves that separately show the contributions of the post- and preshock regions, as well as the transition layer, were removed.

The spectrum of BP Tau at $\lambda < 3100$ Å shown in Fig. 5 is the mean of all of the low-resolution IUE spectra. Gullbring *et al.* (2000) attributed the deviation of the computed spectrum from the observed spectrum at wavelengths shorter than 2000 Å to variability. However, we showed above that an inflection is also present in the STIS spectra of this star, although the time interval between the mid-exposures of the long-wavelength (1600–3150 Å) and short-wavelength (1160–1700 Å) spectra did not exceed 20 min. We see from Fig. 3 from the paper by Gullbring *et al.* (2000) that for T Tau and GW Ori, the accretion-shock radiation is also appreciably weaker than the observed radiation at $\lambda <$ 2000 Å. For comparison with their calculations, Gullbring *et al.* (2000) took the average IUE spectra for these stars. However, an inflection is also seen in the STIS spectra of these stars, whose long-wavelength and short-wavelength parts were obtained almost simultaneously (Kravtsova and Lamzin 2002b). Hence, the deviation of the computed UV continuum energy distribution from the observed distribution cannot be attributed to variability. If the emission continuum of the CTTSs at $\lambda > 2000$ Å actually originates in the accretion shock, then it follows from the aforesaid that the short-wavelength UV continuum of BP Tau, T Tau, and GW Ori is formed outside the accretion shock.

However, we previously found for T Tau, RY Tau, DR Tau, DS Tau, DG Tau, and TW Hya that

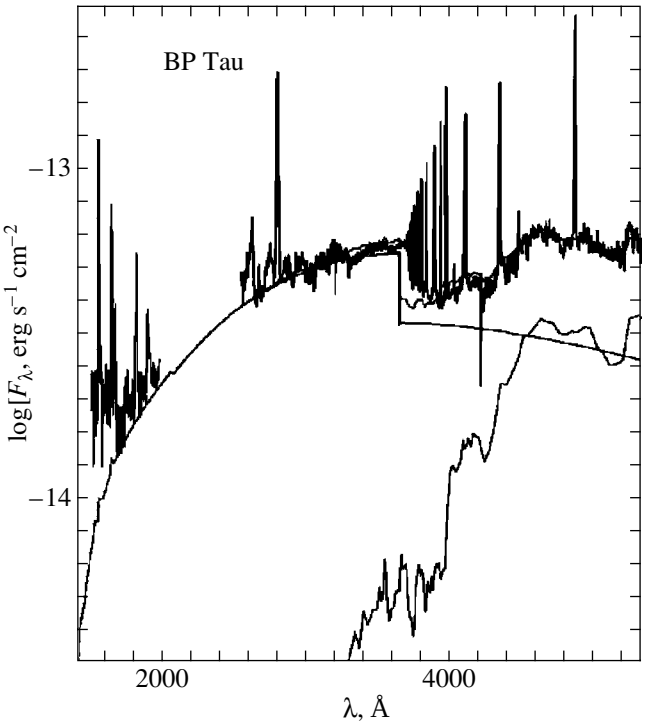

Fig. 5. Comparison of the observed and computed (Gullbring *et al.* 2000) spectral energy distributions for BP Tau. The photospheric stellar spectrum and the accretion-shock-produced spectrum are shown separately.

more than 90% of their emission continuum is formed outside the accretion shock (Kravtsova and Lamzin 2002a, 2002b; Kravtsova 2003). This conclusion was drawn from the comparison of the computed (Lamzin 1998, 2003a; Calvet and Gullbring 1998) and observed ratios of the flux in the C IV 1550 doublet lines to the bolometric flux in the emission continuum. Below, we show that a similar conclusion can also be reached for BP Tau.

We found from the spectrum shown in Fig. 2 that the flux in the C IV 1550 doublet lines at the time of observation was 2.5×10^{-13} erg s^{-1} cm^{-2}. This value is less than 10% larger than the value obtained by Errico *et al.* (2001) from the HST/GHRS spectrum in the 1993 observations and/or the value averaged over all of the spectra observed from the IUE satellite over a ten-year period (Valenti *et al.* 2000). Correcting this flux for interstellar extinction with $R_V = 3.1$ and $A_V = 0\overset{m}{.}5$, we obtain $F_{\rm C\,IV} = 8.4 \times 10^{-13}$ erg s^{-1} cm^{-2}. According to Ardila and Basri (2000), the observed bolometric flux in the continuum of BP Tau attributable to accretion is $F_c^{\rm bol} \simeq 2 \times 10^{-10}$ erg s^{-1} cm^{-2}. It thus follows that $\xi \equiv F_{\rm CIV}/F_c^{\rm bol} \simeq 0.4\%$; this result is virtually independent of the existing uncertainty in the $A_\lambda(\lambda)$ law and the A_V value. Meanwhile, it follows from the calculations of the accretion-shock spectrum (Lamzin 1998, 2003a; Calvet and Gullbring 1998) that ξ must be of the order of several percent.

Thus, as in the case of the six stars mentioned above (for reasoning, see Kravtsova and Lamzin 2002a, 2002b), we conclude that the bulk of the observed emission continuum in BP Tau is formed outside the accretion shock. In our opinion, this is because the magnetic field of the star does not destroy the inner disk regions, and the disk reaches its surface. As a result, the bulk of the accreted material settles in the equatorial plane of the star, and only a small fraction of it flows through the magnetosphere and the accretion shock (for more detail, see Kravtsova and Lamzin 2002a).

In the two-flow accretion model, the emission continuum at $\lambda > 2000$ Å originates mainly in the inner disk and/or the boundary layer. It follows from our analysis of the profiles for optically thin C II, Al II, and Si II lines in the spectrum of DR Tau that these lines originate in the accretion-disk chromosphere (Kravtsova and Lamzin 2002a). This suggests that the disk chromospheres are also responsible for the hot UV continuum at wavelengths $\lambda < 2000$ Å; we believe that its presence has been firmly established in the four CTTS stars that we studied.

The chromospheres of young stars can be an alternative source of the high-temperature continuum. X-ray radiation with energy up to 2 keV is observed

in many CTTSs, including the four stars that we studied, while the accretion shock cannot account for the observed intensity of the radiation with $E > 1$ keV (Lamzin 1999). This radiation is assumed to be produced by the coronal plasma with $T \sim 10^7$ K that is confined by the star's closed large-scale magnetic field lines (Feigelson and Montmerle 1999). The short-wavelength UV continuum can then be associated with the radiation from cooler regions at the footpoints of the same magnetic loops, and these regions may be considered as the stellar chromosphere.

Thus, we believe that the UV continuum of the CTTSs originates either in the chromosphere of the star itself or in the chromosphere of its accretion disk. At this point, both our two-flow accretion model and the ideas of the corona and chromosphere of CTTSs are nothing more than qualitative hypotheses. Therefore, we cannot yet choose between them.

CONCLUSIONS

We have analyzed the low-resolution UV HST/STIS spectra of four CTTSs (BP Tau, GW Ori, T Tau, and RY Tau) and found an inflection in the $F_\lambda^c(\lambda)$ curve near 2000 Å. This inflection probably stems from the fact that the UV continuum in these stars consists of two components: an optically thick gas with $T < 8000$ K and a gas with a much higher temperature. The total luminosity of the hot component is much lower than that of the cool component, but the hot-gas radiation dominates at $\lambda < 1800$ Å. Previously, we reached a similar conclusion for five CTTSs using low-resolution IUE spectra. However, we showed that the continuum level at short wavelength is determined from these spectra with large errors.

We showed that for at least three of the stars studied (BP Tau, GW Ori, and T Tau), the accretion-shock radiation cannot account for the observed dependence $F_\lambda^c(\lambda)$ in the ultraviolet.

Previously, we concluded that for six CTTSs, more than 90% of the emission continuum at $\lambda > 2000$ Å originates not in the accretion shock but in the inner accretion disk. We reached a similar conclusion here for BP Tau. Thus, at this point, the two-flow pattern of accretion has been established for seven CTTSs, i.e., for all of the stars that we studied. In our model, the hot continuum can be associated with the radiation from the disk chromosphere. At the same time, we cannot rule out the possibility that the stellar chromosphere is the source of the hot continuum.

In conclusion, note the following. The stars T Tau, BP Tau, and TW Hya are among the CTTSs for which we concluded that their accretion disk reaches the stellar surface. The mean accretion rate $\dot{M}_{ac}$ for them is $1.3 \times 10^{-7}\ M_\odot\ \mathrm{yr}^{-1}$ (White and Ghez 2001), $1.6 \times 10^{-8}\ M_\odot\ \mathrm{yr}^{-1}$ (Ardila and Basri 2000), and $3 \times 10^{-9}\ M_\odot\ \mathrm{yr}^{-1}$ (Batalha *et al.* 2002), respectively. A magnetic field with a strength above 2 kG was detected in each of these stars (Johns 2002; Johns-Krull *et al.* 1999, 2001; Guenther *et al.* 1999). A dipole magnetic field of such a strength must stop the accretion disk at a distance $> R_*$ from the stellar surface even for T Tau (see formula (1) from Shu *et al.* 2000). The discrepancy between the theory and the observations may stem from the fact that the magnetic field of CTTSs significantly deviates from a dipole field and/or the disk material has a very low conductivity because of the low temperature.

The aforesaid is acceptable if the disk is axisymmetric. However, if the magnetic axis of the star is greatly inclined to its rotation axis, then the symmetry disappears and the disk near the star will break up into separate jets, resembling a spiral galaxy in the plane of the sky (Romanova 2003, private communication). Part of the jet gas that reached the star will move almost radially, and the remaining part will move almost tangentially to the surface. An accretion shock will emerge only in the former case, while the remaining gas will decelerate in the same way as in the boundary layer. For this scenario, the smallness of X implies that gas in the jets falls to the star almost tangentially to the surface.

ACKNOWLEDGMENTS

We wish to thank C. Batalha for information on the paper by Johns (2002) and the reviewer for helpful remarks. This study was supported by the Russian Foundation for Basic Research, project no. 02-02-16070.

REFERENCES

1. D. R. Ardila and G. Basri, Astrophys. J. **539**, 834 (2000).
2. C. Batalha, N. M. Batalha, S. H. P. Alencar, *et al.*, Astrophys. J. **580**, 343 (2002).
3. K. S. de Boer, Astron. Astrophys. **61**, 605 (1977).
4. N. Calvet and E. Gullbring, Astrophys. J. **509**, 802 (1998).
5. V. M. Costa, J. F. Gameiro, and M. T. V. T. Lago, Mon. Not. R. Astron. Soc. **307**, L23 (1999).
6. V. M. Costa, M. T. V. T. Lago, L. Norci, and E. J. A. Meurs, Astron. Astrophys. **354**, 621 (2000).
7. L. Errico, S. A. Lamzin, and A. A. Vittone, Astron. Astrophys. **377**, 577 (2001).
8. E. D. Feigelson and T. Montmerle, Ann. Rev. Astron. Astrophys. **37**, 363 (1999).
9. A. I. Gomez de Castro and M. Franqueira, *ULDA Access Guide to T Tauri Stars Observed with IUE*, ESA SP-1205 (ESA Publ. Division, ESTEC, Noordwijk, 1997).

10. E. Gullbring, N. Calvet, J. Muzerolle, and L. Hartmann, Astrophys. J. **544**, 927 (2000).
11. E. Gullbring, L. Hartmann, C. Briceño, and N. Calvet, Astrophys. J. **492**, 323 (1998).
12. E. Guenther, H. Lehmann, J. P. Emerson, and J. Staude, Astron. Astrophys. **341**, 768 (1999).
13. G. H. Herbig and R. W. Goodrich, Astrophys. J. **309**, 294 (1986).
14. C. Imhoff and I. Appenzeller, in *Exploring the Universe with IUE Satellite,* Ed. by Y. Kondo *et al.* (Kluwer Acad., Dordrecht, 1987), p. 295.
15. C. Johns, Publ. Astron. Soc. Pac., Conf. Ser. **244**, 147 (2002).
16. C. M. Johns-Krull, J. A. Valenti, and C. Koresko, Astrophys. J. **516**, 900 (1999).
17. C. M. Johns-Krull, J. A. Valenty, S. H. Saar, *et al.*, Astron. Soc. Pac. Conf. Ser. **223**, 521 (2001).
18. A. S. Kravtsova, Pis'ma Astron. Zh. (2003, in press).
19. A. S. Kravtsova and S. A. Lamzin, Pis'ma Astron. Zh. **28**, 748 (2002a) [Astron. Lett. **28**, 676 (2002a)].
20. A. S. Kravtsova and S. A. Lamzin, Pis'ma Astron. Zh. **28**, 928 (2002b) [Astron. Lett. **28**, 835 (2002b)].
21. S. A. Lamzin, Astron. Astrophys. **295**, L20 (1995).
22. S. A. Lamzin, Astron. Zh. **75**, 367 (1998) [Astron. Rep. **42**, 322 (1998)].
23. S. A. Lamzin, Pis'ma Astron. Zh. **25**, 505 (1999) [Astron. Lett. **25**, 430 (1999)].
24. S. A. Lamzin, Astron. Zh. (2003a, in press).
25. S. A. Lamzin, Astron. Zh. (2003b, in press).
26. J. S. Mathis, Ann. Rev. Astron. Astrophys. **28**, 37 (1990).
27. J. Najita, S. Edwards, G. Basri, and J. Carr, in *Protostars and Planets IV,* Ed. by V. Mannings *et al.* (Arizona Univ. Press, 2000), p. 457.
28. F. H. Shu, J. R. Najita, H. Shang, and Zh. Li, in *Protostars and Planets IV,* Ed. by V. Mannings *et al.* (Arizona Univ. Press, 2000), p. 789.
29. J. A. Valenti, C. M. Johns-Krull, and J. L. Linsky, Astrophys. J., Suppl. Ser. **129**, 399 (2000).
30. R. J. White and A. M. Ghez, Astrophys. J. **556**, 265 (2001).

Translated by V. Astakhov

Astronomy Letters, Vol. 29, No. 9, 2003, pp. 621–628. Translated from Pis'ma v Astronomicheskiĭ Zhurnal, Vol. 29, No. 9, 2003, pp. 701–708.

The Betatron Effect in Collapsing Magnetic Traps

B. V. Somov* **and S. A. Bogachev**

Sternberg Astronomical Institute, Universitetskii pr. 13, Moscow, 119992 Russia

Received March 25, 2003

Abstract—We consider the question of how the betatron effect affects the particle acceleration in a magnetic trap with a rapidly decreasing length. We show that the additional increase in energy caused by the betatron acceleration as the trap contracts is exactly offset by the decrease in the time of particle confinement in the trap, because the loss cone becomes larger during the contraction. As a result, the particle energy at the time of escape from the trap remains the same as that in a collapsing trap without contraction. We estimate the Alfvén-pumping efficiency in a collapsing trap in connection with the problem of particle acceleration in solar flares. The additional energy acquired by particles from magnetic-field oscillations is shown to be negligible. We discuss the possible observational manifestations of the betatron effect in solar flares. © *2003 MAIK "Nauka/Interperiodica".*

Key words: *Sun, magnetic fields, particle acceleration, solar flares.*

INTRODUCTION

Collapsing magnetic traps emerge not only during the gravitational collapse of stars and other astronomical objects, for example, protostellar clouds with frozen-in magnetic fields. Much more often and under more common conditions, for example, in the interstellar medium, traps with magnetic mirrors that rapidly move toward each other result from a simple kinematic effect—the passage of a nonuniform magnetic field through a shock front. Reflecting from the shock front, particles are trapped in magnetic loops and acquire energy in each reflection from the shock front. This process corresponds to the first-order Fermi acceleration mechanism (Fermi 1954), i.e., the most efficient variety of this mechanism. Observations of interplanetary shocks (Balogh and Erdos 1991) indicate that interplanetary protons are most intensely accelerated precisely in this way (Erdos and Balogh 1994).

Collapsing traps are formed in the solar atmosphere during flares in the process of magnetic reconnection (Somov and Kosugi 1997). Figure 1 illustrates this possibility in a two-dimensional reconnection model. The plasma flows near the reconnecting current sheet (RCS) are indicated by the heavy arrows $\mathbf{v}_0$ (inflow velocity) and $\mathbf{v}_1$ (outflow velocity). The reconnected field lines move from the sheet together with the collisionless ultrahot (with an electron temperature $T_e \gtrsim 30$ MK) plasma toward the magnetic obstacle (MO), a stronger magnetic field region (shaded). The top of each magnetic loop moves with the super-Alfvén velocity $\mathbf{v}_1$ toward the shock wave (SW) and its footpoints are connected with the field sources, spots N and S on photosphere Ph. The electrons and ions preaccelerated in the current sheet are captured in a trap whose length rapidly decreases to zero (collapses) when the top of the loop passes through the shock front.

The particle acceleration can be shown in a very simple model—a long trap with short mirrors: the decreasing (with time) trap length $L(t)$ is much larger than the length l_m of the magnetic mirrors (Fig. 2). We assume that the field $\mathbf{B}$ is uniform and constant inside the trap but grows from $\mathbf{B}$ to $\mathbf{B}_m$ in the mirrors. The quantity B_m/B is called the mirror ratio. The larger the mirror ratio, i.e., the field jump at the shock front, the higher the particle confinement efficiency in the trap. The validity conditions for the model are discussed below.

As the separation between the mirrors decreases, the longitudinal momentum of the particles increases and, as a result, their kinetic energy increases. Under typical conditions of solar flares, the acceleration efficiency of the electrons and ions in collapsing traps is probably very high (Somov and Kosugi 1997; Somov 2000; Bogachev and Somov 2001; Kovalev and Somov 2002, 2003). Meanwhile, the simple model disregards several factors that seem significant. For example, as the trap moves toward a shock wave, the magnetic field strength in the trap must increase (the trap contracts), which causes the transverse particle momentum to increase. This effect, i.e., betatron acceleration, is well known in the physics of the Earth's magnetosphere. In addition, the inevitable

*E-mail: somov@lnfm1.sai.msu.ru

1063-7737/03/2909-0621$24.00

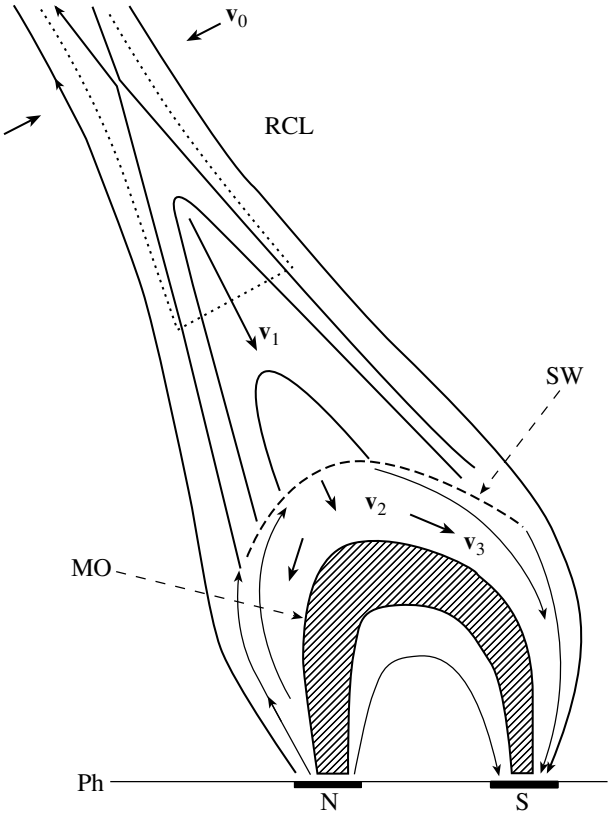

Fig. 1. The magnetic trap between a reconnecting current sheet (RCS) and a shock wave (SW): $\mathbf{v}_0$ is the velocity of the coronal plasma inflow into the current sheet, $\mathbf{v}_1$ is the super-Alfvén velocity of the ultrahot plasma outflow from the current sheet, $\mathbf{v}_2$ is the postshock plasma velocity, and $\mathbf{v}_3$ is the spreading velocity of the compressed and shock-heated plasma along magnetic field lines toward the footpoints of the flare magnetic loop, a magnetic obstacle (MO).

oscillations of the collapsing trap can lead to Alfvén pumping (Alfvén 1949). This effect consists in the betatron particle acceleration and the simultaneous nonadiabatic scattering by small-scale magnetic-field nonuniformities (or particles) and seems to be a very general acceleration mechanism in cosmic plasma (Alfvén and Fälthammer 1963; Bakhareva *et al*. 1970).

Here, our goal is to elucidate how the betatron effect (in a pure form and as a constituent of the Alfvén pumping) affects the particle acceleration in collapsing traps that are formed in the process of fast reconnection during the impulsive flare phase.

THE ROLE OF BETATRON ACCELERATION

If the magnetic field inside the trap is assumed to be uniform and constant, $B = B_0$ (see the Section entitled "Validity conditions for the model"), then the longitudinal particle momentum in the adiabatic approximation increases with its decreasing length $L(t)$ as

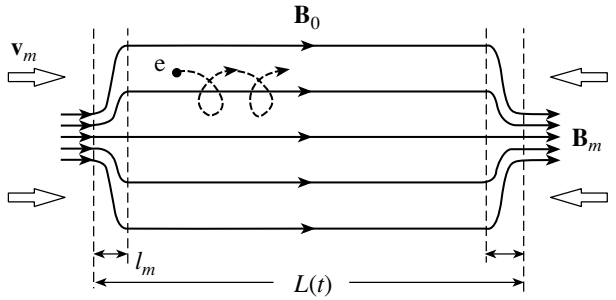

Fig. 2. A model of a long trap with magnetic mirrors moving toward each other; $\mathbf{v}_m$ is the mirror velocity.

$$p_{\parallel}(l) = \frac{p_{0\parallel}}{l}, \tag{1}$$

where the dimensionless trap length $l(t) = L(t)/L_0$. The transverse particle momentum inside the magnetic trap is constant,

$$p_{\perp} = p_{0\perp}, \tag{2}$$

because the first adiabatic invariant is conserved:

$$\frac{p_{\perp}^2}{B} = \text{const}. \tag{3}$$

The time of particle escape from the trap, $l = l_{\rm es}$, depends on the initial pitch angle θ_0 of the particle and is determined by the condition

$$\tan\theta_0 = \frac{p_{0\perp}}{p_{0\parallel}} \le \frac{1}{Rl_{\rm es}}, \tag{4}$$

where the parameter

$$R = \left(\frac{B_m}{B_0} - 1\right)^{1/2}. \tag{5}$$

The kinetic energy of the particle at the time of its escape is

$$\varepsilon = \frac{p_{0\perp}^2}{2m}\left(R^2 + 1\right) = \frac{p_{0\perp}^2}{2m}\frac{B_m}{B_0}. \tag{6}$$

If the thickness of the trap also decreases with its decreasing length, then the field B inside the trap increases as $B(l)$. In this case, it follows from (3) that the transverse momentum increases simultaneously with the longitudinal momentum,

$$p_{\perp}(l) = p_{0\perp}\left(\frac{B(l)}{B_0}\right)^{1/2}. \tag{7}$$

Here, B_0 is the initial (at $l = 1$) field in the trap. The kinetic energy of the particle

$$\varepsilon = \frac{p_{\parallel}^2 + p_{\perp}^2}{2m} = \frac{1}{2m}\left(\frac{p_{0\parallel}^2}{l^2} + \frac{p_{0\perp}^2 B(l)}{B_0}\right) \tag{8}$$

increases faster than that in the absence of trap contraction. For this reason, it seems natural to assume that the acceleration efficiency in a collapsing trap also increases.

Note, however, that, as the trap contracts, the loss cone becomes larger,

$$\theta_{\rm es}(l) = \arcsin\left(\frac{B(l)}{B_m}\right)^{1/2}. \quad (9)$$

Consequently, the particle escapes from the trap earlier. At the time of its escape, the momentum of the particle satisfies the condition

$$p_\parallel(l) = R(l)p_\perp(l), \quad (10)$$

where the parameter

$$R(l) = \left(\frac{B_m}{B(l)} - 1\right)^{1/2}. \quad (11)$$

Hence, using (7), we determine the energy of the particle at the time of its escape from the trap

$$\varepsilon = \frac{p_\perp(l)^2}{2m}\left(R(l)^2 + 1\right) \quad (12)$$
$$= \frac{p_{0\perp}^2}{2m}\frac{B(l)}{B_0}\frac{B_m}{B(l)} = \frac{p_{0\perp}^2}{2m}\frac{B_m}{B_0}.$$

The kinetic energy (12) that the particle gains in a contracting trap is equal to the energy (6) acquired in a collapsing trap without contraction, i.e., in the case $B = B_0 = \text{const}$ where there is no betatron effect.

Thus, the contraction of a collapsing trap (as well as its expansion) does not affect the final energy that the particle acquires during its acceleration. The earlier particle escape from the trap is exactly offset by the faster gain in energy. The acceleration efficiency (the ratio of the final and initial particle energies) is determined solely by the decrease in the length of the trap rather than by its contraction. Characteristically, the acquired energy does not depend on the pattern of decrease in the trap length either. It depends only on the initial particle momentum or, to be more precise, on its transverse component $p_{0\perp}$ and the field jump B_m/B_0.

ALFVÉN PUMPING

If the magnetic field changes not monotonically but periodically, then a particle can gain an additional energy under certain conditions. This phenomenon is called Alfvén pumping. Alfvén (1949) considered a field with local nonuniformities characterized by significant variations at distances smaller than the Larmor radius. When a particle passes through such nonuniformities, condition (3) is violated. The particle motion becomes random, with the momenta tending to be uniformly distributed between the three degrees of freedom. If the field contracts, then a fraction of the energy acquired during the betatron acceleration is transferred to the parallel component of the particle motion. In this case, the decrease in the energy of the transverse motion with decreasing magnetic field is smaller than its increase in the growth time, and the particle acquires an additional energy on completion of the full cycle. Thus, the total particle energy can systematically increase even if the fluctuating magnetic field does not grow. In this case, the pattern of field variation is of no fundamental importance (Alfvén and Fälthammer 1963).

Tverskoi (1967a, 1967b) showed that in a turbulent cosmic plasma, the Fermi acceleration related to the reflection from long strong waves is efficient only in the presence of fast particle scattering by short waves whose length is comparable to the particle Larmor radius. Unfortunately, currently available observations of solar flares give no information about the presence of short-wavelength turbulence in collapsing traps. To avoid superfluous assumptions, we assume that the accelerated particles in the trap are scattered only through Coulomb collisions. Let T be the characteristic period of the relatively slow long-wavelength field variations, for example, Alfvén or magnetoacoustic oscillations of the trap. The realization of the Alfvén pumping mechanism then requires that

$$T > \tau. \quad (13)$$

Here, τ is the characteristic time of the particle momentum redistribution in degrees of freedom. For Coulomb electron–electron collisions, this time is

$$\tau = \frac{{m_{\rm e}}^2 v^3}{\pi e^4 n}\frac{1}{8\ln\Lambda}. \quad (14)$$

The plasma density and temperature in the coronal source of hard X-ray radiation are known from Yohkoh observations (Masuda *et al.* 1994; Tsuneta *et al.* 1997): $n \approx 3\times10^9$ cm^{-3} and $T \approx 10^8$ K, respectively. As a result, the characteristic collision time τ is about 3 s, which determines the minimum period T. Consequently, the number of pumping cycles $N_{\rm c}$ in the trap lifetime ($t \lesssim 10$ s) cannot exceed three.

If the amplitude of the field variations is $\delta B = (k-1)B_0$, then the particle momentum p after $N_{\rm c}$ cycles increases to (Alfvén and Fälthammer 1963)

$$p = p_0\beta^{N_{\rm c}}, \quad (15)$$

where

$$\beta = \frac{1}{3}\left(5 + 2k + \frac{2}{k}\right)^{1/2}. \quad (16)$$

At reasonable amplitudes (e.g., $k \approx 1.1$), the increment in particle momentum is only $0.005p_0$ even after five cycles. This suggests that Alfvén pumping is of minor importance in a collapsing magnetic trap. Alfvén pumping does not appreciably affect the impulsive electron acceleration in solar flares.

As applied to the impulsive phase of solar flares, this conclusion can hardly be changed by attempting to choose conditions that greatly differ from those considered above and, at the same time, are consistent with the currently available observations. Bearing in mind the wide variety of flares, we may assume, for example, that, for some of them, the plasma density inside the trap is slightly higher and the temperature is slightly lower than the corresponding values used to estimate the Coulomb collision time. In this case, collisions will sharply increase in importance, while the efficiency of the main process, the acceleration on the moving magnetic mirrors, will decrease. Instead of being accelerated, the plasma will just be heated on the reconnected magnetic field lines.

THE NUMBER OF PARTICLES IN A TRAP

Let us return to the betatron acceleration in a collapsing trap. Trap contraction increases the loss cone. As a result, the earlier particle escapes from the trap cause the number of particles to decrease,

$$N(l) = N_0 \frac{R_{\text{eff}}(l) l}{\sqrt{1 + R_{\text{eff}}(l)^2 l^2}}. \tag{17}$$

Here, the parameter

$$R_{\text{eff}}(l) = \left(\frac{B_m}{B_0} - \frac{B(l)}{B_0} \right)^{1/2}. \tag{18}$$

Since $R_{\text{eff}}(l) < R$, the number of particles in a contracting trap is always smaller than their number in a collapsing trap without contraction.

The decrease in $N(l)$ does not imply an automatic reduction in the particle density in the trap. As the length of the trap l decreases, its volume $V(l) \sim l$ decreases proportionally to l. We take into account the conservation of magnetic flux $F = B(l)S(l)$ inside the trap. Here, $S(l)$ is the cross-sectional area of the trap, so $S(l)l = V(l)$. Then, the volume is $V \sim l/B(l)$, and the particle density is

$$n(l) = n_0 \frac{B(l)}{B_0} \frac{R_{\text{eff}}(l)}{\sqrt{1 + R_{\text{eff}}(l)^2 l^2}}. \tag{19}$$

Thus, both the number of particles and their density depend on the pattern of increase in the magnetic field $B(l)$.

Let, for certainty, the cross-sectional area $S(l)$ of the trap decrease proportionally to its length l. The field inside the trap is then defined by the formula

$$B(l) = B_0/l, \tag{20}$$

and the effective mirror parameter

$$R_{\text{eff}}(l) = \left(R^2 - \frac{1-l}{l} \right)^{1/2}. \tag{21}$$

The acceleration time in such a trap is shorter than that in a collapsing trap without contraction. At

$$l_{\text{cr}} = \frac{1}{R^2 + 1}, \tag{22}$$

the magnetic field in the trap becomes equal to the field in the mirrors, and the magnetic reflection ceases to work. The parameter R_{eff} becomes zero at this time. The number of particles in a contracting trap decreases (Fig. 3), while their density continuously increases (Fig. 4).

OBSERVATIONAL PREDICTIONS OF THE MODEL

As the trap length decreases, each reflection from a moving magnetic mirror increases the particle velocity by $2V_m$, where V_m is the mirror velocity. Accordingly, the longitudinal particle momentum becomes larger by $\delta p = 2mV_m$, where m is the particle mass. Trap contraction increases the transverse particle momentum through betatron acceleration, thereby increasing the rate of energy gain. At the same time, the field strengthening during the contraction decreases the mirror ratio, i.e., reduces the force of the particle-confining magnetic mirrors. As a result, the faster gain in energy is exactly offset by the earlier particle precipitation from a collapsing trap. The kinetic energy that the particle acquires during its acceleration does not depend on the betatron effect and is always defined by formula (6). Does this imply that the betatron effect will in no way manifest itself in observations of the particle acceleration in collapsing traps during solar flares? Of course not. Future observations may reveal the following features of the model under consideration.

First, trap contraction does not change the energy of the escaping particles, but this energy is reached at an earlier stage of the magnetic collapse, when the trap length is finite and defined by formula (22). In this sense, the betatron effect significantly increases the efficiency of the main process—the particle acceleration on the converging magnetic mirrors. The particle acceleration in shockless collapsing traps primarily becomes more efficient (Somov and Kosugi 1997).

Let us consider a trap with magnetic field lines that concentrate near photospheric sources, as shown in

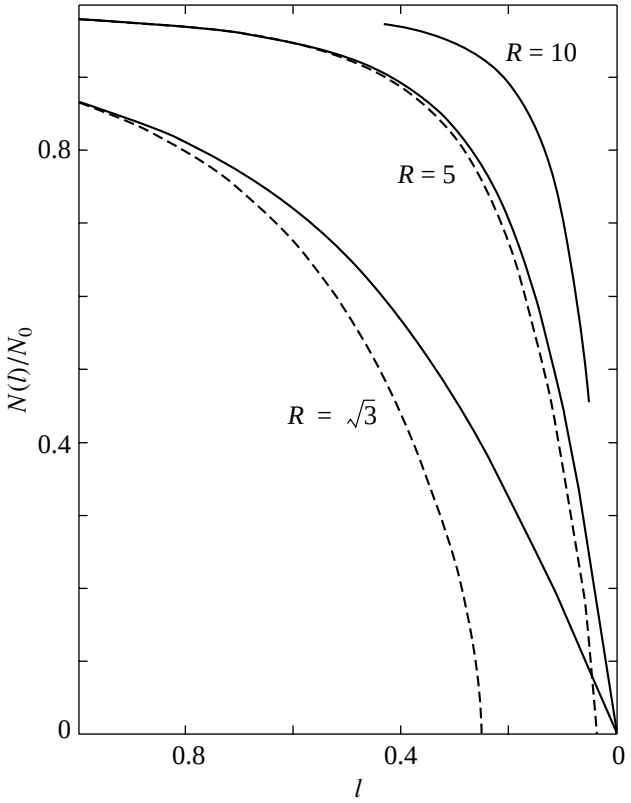

Fig. 3. The number of particles in a trap as a function of its dimensionless length l for various values of the mirror parameter R. The solid lines correspond to a collapsing trap with a constant cross section and, hence, a constant magnetic field, $B = \text{const}$. The dashed lines show how the number of trapped particles will change as the trap contracts. In the extreme case of $R = 10$, the solid and dashed lines virtually coincide.

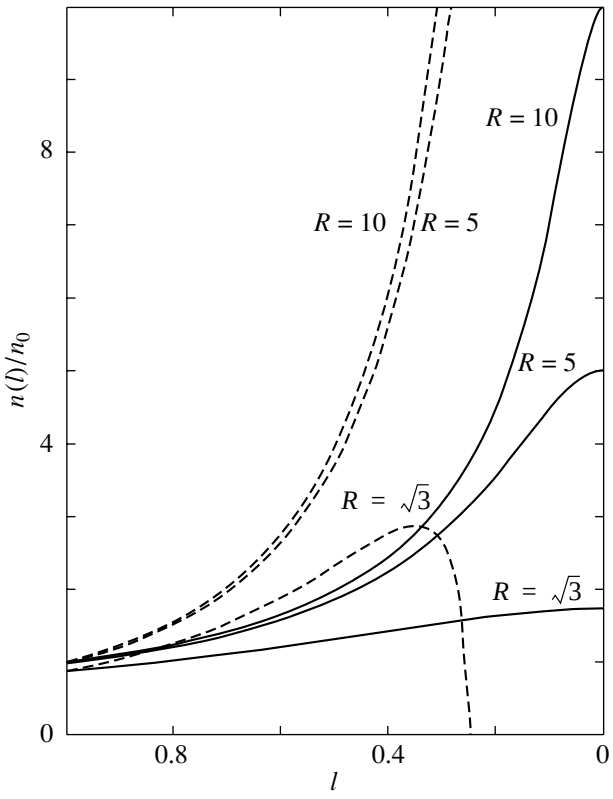

Fig. 4. The density of trapped particles as a function of the dimensionless trap length l and the mirror parameter R. As in Fig. 3, the solid and dashed lines correspond to $B = \text{const}$ and a contracting trap, respectively.

Fig. 5. In such a trap, the length of the reconnected field lines decreases from a value proportional to l_1 to a finite value proportional to l_2. In this case, if we ignore the betatron effect, then the longitudinal particle momentum is defined by the formula (instead of (1))

$$p_\parallel(t) \approx p_\parallel(0)\frac{l_1 + l_2}{l_2 + (l_1 - v_1 t)} \qquad (23)$$
$$\Rightarrow p_\parallel(0)\frac{l_1 + l_2}{l_2}, t \to t_1.$$

The particle acceleration on the magnetic mirrors stops at the time t_1 at a finite longitudinal momentum that corresponds to the residual trap length. Given the betatron acceleration during the contraction of a collapsing trap, the particle can acquire the same energy (6) by this time and earlier if the residual trap length is comparable to the critical length (22).

Second, the betatron effect leads to earlier particle escapes from a collapsing trap, which must be reflected on the time profiles of coronal and chromospheric hard X-ray bursts. The radiation reaches a maximum intensity at various energies earlier because of the faster particle acceleration and precipitation into the chromosphere. In addition, earlier particle precipitation does not cause the density of the accelerated particles in the trap to decrease. The decrease in the volume of the trap during its contraction results in an increase in the density of the trapped particles, despite the reduction in their number. Accordingly, the ratio of the intensity of the coronal hard X-ray radiation to the intensity of the chromospheric radiation, which is generally calculated in the model of a thick target (Syrovatskii and Shmeleva 1972), must change.

Third, an increase in the density of the plasma and the accelerated particles enhances the role of Coulomb collisions. In the absence of contraction, the characteristic collision time is $\tau \sim 3$ s. The betatron effect decreases τ in inverse proportion to the density n. Although the total particle energy at the exit from the trap does not change, it is differently distributed between the nonthermal and thermal components in the source of hard X-ray radiation. Trap contraction also changes the angular distribution of

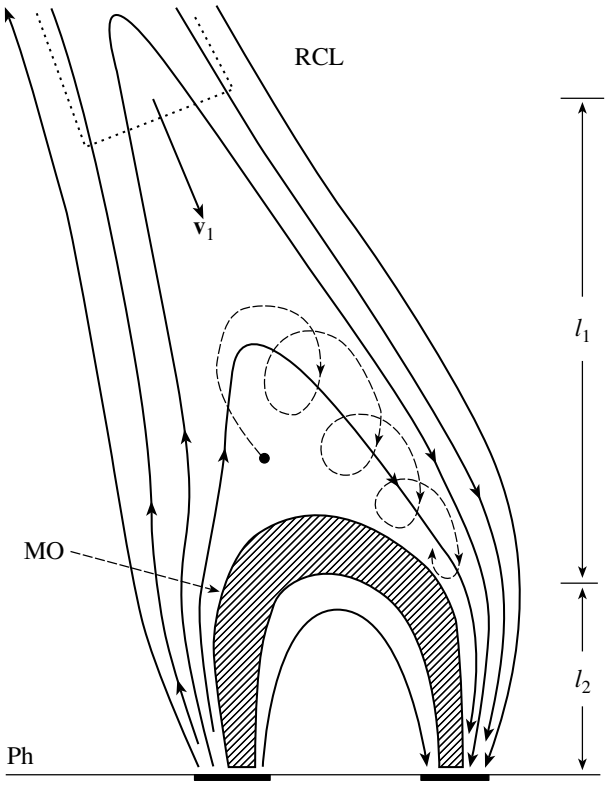

Fig. 5. A shockless collapsing trap in the corona. The magnetic field strengthens as the particle approaches photospheric sources (e.g., sunspots). If the longitudinal particle momentum becomes zero high enough above the photosphere for the particle to undergo no Coulomb collisions in the chromosphere, then it returns to the weaker magnetic field region and reflects.

the escaping particles. It will be possible to study this effect in future observations of the polarization and anisotropy of the X-ray and optical radiation produced by fast particles in the chromosphere.

Finally, if the magnetic-field variations are fluctuations (or these fluctuations are superimposed on a monotonic increase of the field strength in a collapsing trap), then the particle can gain additional energy through Alfvén pumping. However, the efficiency of this mechanism in a coronal trap is very low. The increase in particle energy for the entire collapse time does not exceed one percent and cannot compete with the main effect—the acceleration on the converging magnetic mirrors and the betatron effect. In other words, the process of Alfvén pumping is too slow to be detectable against the background of rapid acceleration during the impulsive phase of solar flares. However, this does not rule out the fundamental possibility of observing the field fluctuations themselves or their oscillations, for example, by radio-astronomical methods.

VALIDITY CONDITIONS FOR THE MODEL

Let us explore the question of how much our results can change if we consider the betatron effect and Alfvén pumping in a collapsing trap of a more realistic shape, for example, as shown in Fig. 1. The initial assumption that the magnetic field inside the trap is uniform and constant, i.e., the approximation of a long trap with short mirrors, seems most inadequate in this connection. What conditions does this approximation actually imply? In what sense is the magnetic field uniform and constant?

We first disregard the field nonuniformities for which significant field variations occur at distances much larger than the Larmor radius of the ions injected into the trap from the reconnecting current sheet. The electron temperature in the latter is very high: $T_\mathrm{e} \sim 10^8$ K (Somov 2000). The proton temperature T_p is lower than the electron temperature. However, even if we assume that $T_\mathrm{p} \sim T_\mathrm{e}$, then the Larmor radius of the protons is $r_\mathrm{L}^\mathrm{p} \sim 10^3$–$10^2$ cm for a magnetic field in the collapsing magnetic trap $B \sim 10$–100 G.

The initial trap length in compact impulsive solar flares is $L(0) \gtrsim 10^9$ cm. Thus, until very late stages of the magnetic collapse ($l \lesssim 10^{-6}$–10^{-7}), the field inside the trap may be considered weakly nonuniform. Can such a field nonuniformity affect the second adiabatic invariant and, as a result, formula (1) for the longitudinal particle momentum? By definition, the second or longitudinal adiabatic invariant is

$$I_2 = \oint \mathbf{p}_\parallel d\mathbf{r} = p \oint \left(1 - \frac{B(r)}{B_m}\right)^{1/2} dr. \qquad (24)$$

As always, according to the general theory of adiabatic invariants (see, e.g., Landau and Lifshitz 1988, § 29), the integration here is along the closed trajectory of the longitudinal particle motion in a trap with fixed magnetic mirrors. In this case, $p = \mathrm{const}$ because $\varepsilon = \mathrm{const}$. Of course, the particle trajectory (and, hence, the integral in the second equality) depends on the shape of the magnetic field lines inside the trap. Taking into account the actual magnetic-field geometry and the fact that the field is weakly nonuniform, we can represent formula (24) as

$$I_2(l) = \oint \mathbf{p}_\parallel d\mathbf{r} = f_g(l) p_\parallel(t) L(t). \qquad (25)$$

Here, $f_g(l)$ is the geometrical factor that results from the integration along the closed trajectory. The characteristic time of one cycle of the longitudinal motion at the initial stage of the magnetic collapse for electrons with a thermal velocity can be estimated as

$$\tau(0) \sim L(0)/V_{Te} \sim 0.1 \text{ s}, \qquad (26)$$

where $V_{Te} \sim 10^{10}$ cm s^{-1} is the mean thermal velocity of the electrons heated in the high-temperature turbulent current sheet. This time is much shorter than the characteristic time of the magnetic-field variations

$$t(0) \sim L(0)/v_1 \sim 10 \text{ s}, \quad (27)$$

where $v_1 \sim 10^8$ cm s^{-1} is the characteristic velocity of the magnetic-loop top toward the shock front, as shown in Fig. 1. The satisfaction of the condition $\tau(0) \ll t(0)$ guarantees the validity of the adiabatic approximation for the longitudinal motion of the trapped particles and ensures that the function $f_g(l)$ is slow. (The specific form of the function $f_g(l)$ is of no importance; it is only important that it changes adiabatically slowly.) For protons and heavier ions, the acceleration is discrete at the initial stage of the magnetic collapse. However, during the collapse, the frequency of reflections from the magnetic mirrors rapidly increases (Somov *et al.* 2002).

Thus, the magnetic field inside collapsing traps in solar flares may be considered weakly nonuniform and slowly changing. Actually, this implies that we may use formula (1). Moreover, the curvature of the magnetic field lines for the conditions under consideration leads to negligibly slow drifts: gradient and inertial ones (for more detail, see Somov 2000, Section 4.2.5). The main effect in the model under consideration is the reflection of particles from the moving magnetic mirrors, i.e., from the front of a collisionless oblique shock wave (see, e.g., Burgess 1995). Here, the proton Larmor radius is the characteristic linear scale length, and the jump in the magnetic field depends on the postshock cooling regime.

Future observations of solar flares may require the development of more refined models that will include the subtle effects attributable to the curvature of the magnetic field lines and field nonstationarity outside the scope of adiabaticity. As regards our main conclusions about the physics of the particle acceleration in collapsing magnetic traps, they were reached in a well-controllable, simple analytic approximation and will be either confirmed or rejected by multiwavelength high-resolution observations of solar flares.

CONCLUSIONS

During the collapse of a magnetic trap, the decrease in its length causes the longitudinal momentum of the particles and, hence, their kinetic energy to increase. Trap contraction increases the transverse momentum and, thereby, causes a further increase in energy, i.e., betatron acceleration. However, as we showed in this paper, this increase in energy is exactly offset by the decrease in the time of particle confinement in the trap, because the trap contraction increases the loss cone. The final energy of the particles escaping from the trap remains the same as the energy of the particles escaping from a collapsing trap without contraction. This energy is defined by formula (6).

In terms of astrophysical applications, especially in connection with the problem of particle acceleration in solar flares, it is fundamentally important that in the presence of betatron acceleration, the particles gain energy (6) and leave the trap before its collapse, i.e., at the residual length $l = l_{cr}$. This effect significantly extends the validity range of the model. It allows us to consider collapsing traps not only with a shock wave but also without it. This situation is to be expected when the reconnection takes place high in the corona, far from photospheric magnetic-field sources, as follows from several Yohkoh and SOHO observations (McKenzie and Hudson 1999; Simnett 2000; Wang and Sheeley 2002). In contrast to compact impulsive flares, so-called smooth flares or long-duration events (LDEs) are characterized by smaller magnetic-field gradients and lower rates of magnetic reconnection. One may also expect the presence of shockless collapsing magnetic traps for such flares.

The model that includes the betatron effect in collapsing traps has several observational manifestations, which gives hope that it will be confirmed in future Solar-B satellite observations of solar flares.

ACKNOWLEDGMENTS

This study was supported by the Russian Foundation for Basic Research, project no. 99-02-16344. We are grateful to the referee for helpful remarks.

REFERENCES

1. H. Alfvén, Phys. Rev. **75**, 1732 (1949).
2. H. Alfvén and Fälthammer, *Cosmical Electrodynamics* (Oxford, 1963; Mir, Moscow, 1967).
3. A. Balogh and G. Erdos, J. Geophys. Res. **96**, 15 853 (1991).
4. M. F. Bakhareva, V. N. Lomonosov, and B. A. Tverskoi, Zh. Éksp. Teor. Fiz. **59**, 2003 (1970) [Sov. Phys. JETP **32**, 1086 (1970)].
5. S. A. Bogachev and B. V. Somov, Astron. Zh. **78**, 187 (2001) [Astron. Rep. **45**, 157 (2001)].
6. D. Burgess, *Introduction to Space Physics,* Ed. by M. G. Kivelson and C. T. Russell (Cambridge Univ. Press, Cambridge, 1995), p. 129.
7. G. Erdos and A. Balogh, Astrophys. J., Suppl. Ser. **90**, 553 (1994).
8. E. Fermi, Astrophys. J. **119**, 1 (1954).
9. V. A. Kovalev and B. V. Somov, Pis'ma Astron. Zh. **28**, 554 (2002) [Astron. Lett. **28**, 488 (2002)].
10. V. A. Kovalev and B. V. Somov, Pis'ma Astron. Zh. **29**, 132 (2003) [Astron. Lett. **29**, 111 (2003)].

11. L. D. Landau and E. M. Lifshitz, *Mechanics* (Nauka, Moscow, 1988; English translation of the 3rd ed. Pergamon Press, Oxford, 1976).
12. S. Masuda, T. Kosugi, H. Hara, *et al.*, Nature **371**, 495 (1994).
13. D. E. McKenzie and H. S. Hudson, Astrophys. J. Lett. **519**, L93 (1999).
14. G. M. Simnett, *High Energy Solar Physics: Anticipating HESSI,* Ed. by R. Ramaty and N. Mandzhavidze (Greenbelt, Maryland, 2000); Astron. Soc. Pac. Conf. Ser. **206**, 43 (2000).
15. B. V. Somov, *Cosmic Plasma Physics* (Kluwer Acad. Publ., Dordrecht, 2000), p. 652.
16. B. V. Somov and T. Kosugi, Astrophys. J. **485**, 859 (1997).
17. B. V. Somov, J.-C. Hénoux, and S. A. Bogachev, Adv. Space Res. **30** (1), 701 (2002).
18. S. I. Syrovatskii and O. P. Shmeleva, Astron. Zh. **49**, 334 (1972) [Sov. Astron. **16**, 276 (1972)].
19. S. Tsuneta, S. Masuda, T. Kosugi, *et al.*, Astrophys. J. **478**, 787 (1997).
20. B. A. Tverskoi, Zh. Éksp. Teor. Fiz. **52**, 483 (1967a) [Sov. Phys. JETP **25**, 317 (1967a)].
21. B. A. Tverskoi, Zh. Éksp. Teor. Fiz. **53**, 1417 (1967b) [Sov. Phys. JETP **26**, 821 (1967b)].
22. Y.-M. Wang and N. R. Sheeley, Astrophys. J. **567**, 1211 (2002).

Translated by V. Astakhov

Astronomy Letters, Vol. 29, No. 9, 2003, pp. 629–634. Translated from Pis'ma v Astronomicheskiĭ Zhurnal, Vol. 29, No. 9, 2003, pp. 643–648.

Slow Solar Wind: Sources and Components of the Stream Structure at the Solar Maximum

K. V. Vladimirsky[1], N. A. Lotova[2], and V. N. Obridko[2*]

[1] *Lebedev Institute of Physics, Russian Academy of Sciences, Leninskii pr. 53, Moscow, 117924 Russia*

[2] *Institute of Terrestrial Magnetism, Ionosphere, and Radiowave Propagation, Russian Academy of Sciences, Troitsk, Moscow oblast, 142190 Russia*

Received March 6, 2003

Abstract—We study the sources and components of the solar-wind spatial stream structure at the maximum of the solar cycle 23. In our analysis, we use several independent sets of experimental data: radio-astronomical observations of scattered radiation from compact sources with the determination of the distance from the Sun to the inner boundary of the transonic-flow transition region ($R_{\rm in}$); calculated data on the magnetic-field intensity and structure in the solar corona, in the solar-wind source region, obtained from optical measurements of the photospheric magnetic-field intensity at the Stanford Solar Observatory (USA); and observations of the white-light corona with the LASCO coronograph onboard the *SOHO* spacecraft. We show that at the solar maximum, low-speed streams with a transition region located far from the Sun dominate in the solar-wind structure. A correlation analysis of the location of the inner boundary $R_{\rm in}$ and the source-surface magnetic-field intensity $|B_R|$ on a sphere $R = 2.5R_{\rm S}$ ($R_{\rm S}$ is the solar radius) has revealed the previously unknown lowest-speed streams, which do not fit into the regular relationship between the parameters $R_{\rm in}$ and $|B_R|$. In the white-light corona, the sources of these streams are located near the dark strip, a coronal region with a greatly reduced density; the nonstandard parameters of the streams probably result from the interaction of several discrete sources of different types.

Key words: *solar wind, heliosphere, solar magnetic fields.*

INTRODUCTION

The slow solar wind ($V \leq 400$ km s^{-1}), the complexity and variability of its spatial structure, and the formation conditions for this structure have been the subject of many studies in recent years (Wang and Sheeley 1990; Kojima and Kakinuma 1990; Schwenn 1990; Tu and Marsch 1995; Fillips *et al.* 1995).

In this paper, we study the role of solar coronal magnetic fields in the formation of slow solar-wind streams at the complex epoch of the solar maximum. In years far from the maximum, the source of the slow solar-wind streams is predominantly the region of low heliolatitudes (Kojima and Kakinuma 1990; Rickett and Coles 1991; Sheelay 1999; Karpen 1999; Luhmann *et al.* 1999). In the years of maximum activity, under solar magnetic field polarity reversal conditions, it would be natural to expect the formation of slow streams in the entire heliosphere (Kojima and Kakinuma 1990; Rickett and Coles 1991; Kakinuma 1990; Kojima *et al.* 2000; Tappin *et al.* 1999).

At present, the specific formation mechanisms of solar-wind streams of different types, both fast and slow, have been studied inadequately. The studies of slow solar-wind streams formed in streamers, which until recently have been considered to be the only type of sources of these streams, are presented in the literature in the greatest detail (Karpen 1999; Luhmann *et al.* 1999, Kojima *et al.* 2000; Tappin *et al.* 1999).

The overall qualitative picture, the relationship between the stream speed measured at large distances from the Sun and the source-surface magnetic-field intensity, has recently been presented by Hakamada *et al.* (2002). More detailed information about the formation mechanism of the slow solar-wind streams was obtained in experimental and theoretical studies of the stream structure at the initial phase, in the source region (Sheelay 1999; Karpen 1999; Tappin *et al.* 1999; Obridko and Shelting 2001; Srivastava *et al.* 1999; Wang *et al.* 1997). In this paper, we study the slow solar-wind streams by using the correlation technique developed by Lotova *et al.* (2000, 2002a, 2002b). In our analysis, we use several independent sets of experimental data. The scattering of radio waves near the Sun by circumsolar plasma was

* E-mail: obridko@izmiran.rssi.ru

observed with large radio telescopes of the Russian Academy of Sciences, Pushchino. The intensity and structure of the coronal magnetic field were determined by solving the field equations in the region $R_S \le r \le 2.5R_S$. As the boundary conditions, we used the optical measurements on the solar surface, on the sphere $R = R_S$, carried out at the Stanford Solar Observatory (USA). To refine the data on the stream structure in the source region, we also used the optical observations of the white-light corona performed with the LASCO coronograph onboard the *SOHO* spacecraft.

RADIO-ASTRONOMICAL OBSERVATIONS AND CORONAL MAGNETIC FIELDS

Radio-astronomical observations of the radiowave scattering by circumsolar plasma form the basis for studying the solar-wind stream structure. Observations of quasar scintillations at large ($R \sim 0.5$–1.0 AU) distances from the Sun are conventional here. The most complete results were obtained by Kojima and Kakinuma (1990), Kojima *et al.* (1998), and Asai *et al.* (1998). Radio maps of the spatial solar-wind speed distribution at large distances from the Sun, $R \ge 0.5$–1.0 AU, are annually, since 1973, obtained in the Solar–Terrestrial Environment Laboratory of the Nagoya University (Japan) (Kojima and Kakinuma 1990; Hakamada *et al.* 2002). These maps reveal a stream structure, but the original coordinates of the streams in the solar-wind source region are difficult to restore from them.

Our studies are aimed at investigating the stream structure near the Sun at distances $R \sim 10$–$40R_S$. This is a more complex experimental problem, but it allows us to directly relate the parameters of the accelerated plasma streams to their coronal sources. This extension of the research possibilities is quite important, considering the large amount of information on the coronal structure accumulated in the last years in spaceborne experiments. The difficulties in studying the solar wind near the Sun stem from the fact that the number of quasars that approach the Sun at small distances, $R \le 10R_S$, is small and that the quasars themselves at the short wavelengths necessary to observe scintillations here are weak sources. Therefore, in our experiments, we combine two different methods in which we obtain the same radial dependence of the scattering angle $2\theta(R)$ using quasars at meter wavelengths and the scintillation index $m(R)$ derived from observations of maser sources in the water vapor line ($\lambda = 1.35$ cm). The observations are carried out with large Pushchino radio telescopes of the Russian Academy of Sciences: DKR-1000 and RT-22.

Since the deviations of solar-wind streams from the radial direction at distances on the order of a few tens of solar radii are small, the temporal and angular coordinates of the radio-astronomical observations were directly transferred to the solar-wind source region, to an arbitrary source surface, a sphere of radius $2.5R_S$ that was considered as the region of the onset of circumsolar plasma stream acceleration. Thus, we have a unique opportunity to compare the data on the plasma stream acceleration and velocity with the data on the stream magnetization in the source region. Observations of radio sources that displace in the celestial sphere for many days yield a dependence of the scattering on the projected distance of the line of sight from the Sun. As the parameter that characterizes the stream acceleration rate, we use the distance of the inner boundary of the transonic transition region R_{in} from the Sun determined from the radial dependence of the scattering. A closer location of the boundary R_{in} to the Sun corresponds to a more intense plasma acceleration and higher stream velocities (Lotova *et al.* 1995).

The data on the magnetic-field intensity and structure in the source region were obtained by solving the field equations in the region $R_S \le R \le 2.5R_S$. The calculations were carried out in the potential approximation by using the method developed at the Wilcox Solar observatory (Scanford, USA) and the Institute of Terrestrial Magnetism, Ionosphere, and Radiowave Propagation (Russian Academy of Sciences) (Hoeksema *et al.* 1982; Obridko and Shelting 1992). The results of our calculations were presented in two forms: we determined the absolute values of the radial field component on the source surface $|B_R|$ reconciled in time and angular coordinates with the recording time of R_{in}, the inner boundary of the transition region. In addition, we obtained data on the closed or open type of magnetic-field-line structure in the source region to be able to judge the conditions for the penetration of the frozen-in magnetic field into solar-wind streams.

The table gives the results of our observations: the names of the sounding sources, the recording dates of R_{in}, and the sounding geometry: E/W hemisphere, heliolatitude φ, and distance R_{in}. The last columns contain the results of our calculations of the coronal magnetic field: the field intensity on the source surface $|B_R|$ ($R = 2.5R_S$) and the magnetic-field structure near the Sun ($R \le 2R_S$): the open, closed, or mixed type of configuration of the magnetic field lines. The last column give data on the structure of the white-light corona as observed with the LASCO C2 coronograph onboard the SOHO spacecraft. Our comparison of the pairs of values of R_{in} and $|B_R|$ presented below is an experimental study of the causal relations in the solar-wind-stream acceleration mechanism. The reliability of the conclusions that can be drawn from this comparison is largely corroborated by the

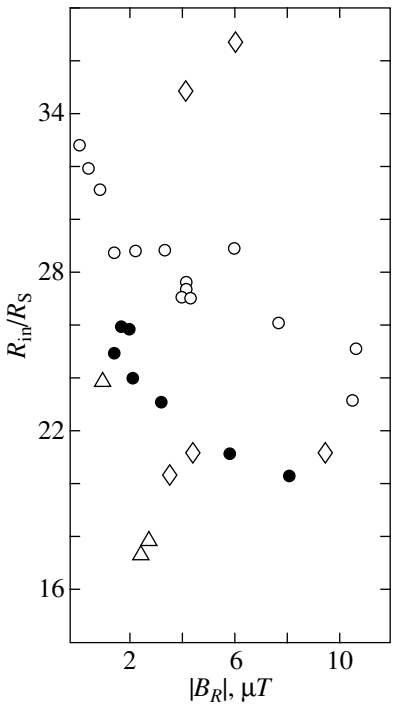

Fig. 1. Correlation between the geometry of the inner boundary of the solar-wind transition region (R_{in}) and the intensity of the solar coronal magnetic fields $|B_R|$ at an $R = 2.5R_S$ level.

optical observations of the plasma stream structure in the region of the white-light corona.

DISCUSSION

The twenty-nine sets of experimental data on solar-wind streams obtained in 2000 at the solar maximum are collected in the table. This table mainly contains the pairs of values of R_{in}/R_S and $|B_R|$. The twenty-nine experiments of the table are divided into four groups according to the structure of the stream sources. An even clearer division of the streams into groups arises when examining the correlation diagram in Fig. 1, which compares the pairs of values of R_{in} and $|B_R|$. The first type of stream (the triangles in Fig. 1, experiments 1–3 in the table) is the fast solar wind, which is poorly represented at the solar maximum and which was studied in detail at other phases of the solar cycle (Lotova *et al.* 2002a, 2002b; Vladimirsky *et al.* 2003). Two groups of slow solar-wind streams are clearly identified in Fig. 1. The second group of experiments, 4–10 in the table, are represented by filled circles in Fig. 1. These streams have the main body of the streamers as the sources. The third, largest group of streams, experiments 11–24 in the table, is represented by open circles in Fig. 1. This group corresponds to the mixed, closed, and open magnetic-field structure

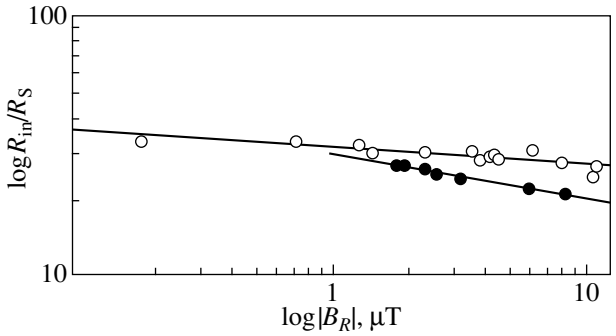

Fig. 2. Two groups of slow solar-wind streams. The straight lines are least squares fits.

in the source region and to the ray structure of the white-light corona emission. Comparison of the values of R_{in} (the location of the inner boundary of the transition region) and $|B_R|$ (the magnetic-field intensity on the source surface) reveals three branches of the regular dependence in the R_{in}, $|B_R|$ correlation diagram (Fig. 1) to which, according to the data of the table, different coronal sources correspond. Thus, different types of streams show up in Fig. 1 as different branches of the correlation between the parameters R_{in} and $|B_R|$. Apart from the above two groups of slow solar-wind streams, the 2000 data revealed the previously unknown, slowest streams, which do not form any regular dependence in the correlation diagram (the diamonds in Fig. 1). These streams are few in number, and their origin can be attributed to the complex interaction between several sources of different types.

Let us consider in more detail the two types of slow solar-wind streams highlighted in Fig. 1 by the regular correlation between R_{in} and $|B_R|$. These two groups of streams are shown in Fig. 2 on a logarithmic scale (the notation is the same as in Fig. 1). The two branches are characterized by a nearly linear dependence. The straight lines were drawn by the least squares method and have different slope: the lower and upper branches have indices $\alpha_1 = -0.182$ and $\alpha_2 = -0.075$, respectively. The difference in slopes may be considered as an independent confirmation of the different nature of the streams. Against the general background of the very complex stochastic processes that take place in the solar cycle and are distinguished by the complexity of the formation and acceleration of solar-wind streams, the existence of an unambiguous relationship gives hope for the existence of a relatively simple group of parameters that determine the acceleration process, which is consistent with model theoretical studies of the circumsolar plasma acceleration. Marsch and Tu (1999) considered the cyclotron resonance as the mechanism of energy exchange between Alfvén waves and

The solar-wind stream structure as determined from radio-astronomical data and the coronal magnetic fields in 2000

No.	Source	Date, 2000	E/W	φ, deg	R_{in}/R_S	$\lvert B_R\rvert$, μT	Magnetic field structure B_R	White-light corona structure
1	3C133	June 6	E	14.0	24	0.6	Open	Streamer sidelobe
2	S255	June 22	E	−82.0	18	3.1		
3	S255	June 24	W	−79.0	17	2.65		
4	3C2	March 3	E	−9.4	20	8.13	Closed	Streamer
5	IRC-20431	Dec. 17	E	16.0	26	1.81		
6	3C225	Aug. 9	E	−2.0	26	1.95		
7	3C133	June 14	W	29.0	25	2.33		
8	3C144	June 22	W	−4.0	24	2.60		
9	3C228	Aug. 24	W	12.0	23	3.25		
10	3C228	Aug. 18	E	9.0	21	5.86		
11	3C138	June 15	W	−51.0	29	6.11	Mixed	Ray emission
12	IRC-20431	Jan. 1	W	5.0	33	0.18		
13	W31(2)	Dec. 16	E	30.0	32	0.74		
14	W28A2(1)	Dec. 30	W	−11.4	31	1.30		
15	3C225	Aug. 24	W	3.0	29	1.47		
16	3C215	Aug. 15	W	5.0	29	2.39		
17	3C138	June 7	E	−66.0	29	3.60		
18	3C208	Aug. 11	W	−26	28	4.38		
19	3C212	Aug. 12	W	−17.8	27.5	4.26		
20	3C207	Aug. 7	W	−35.0	27	4.58		
21	3C245	Aug. 25	E	40.0	27	3.87		
22	3C172	June 28	E	14.0	26	7.94		
23	3C154	June 30	W	32.0	25	10.91		
24	3C166	June 26	E	−22.0	23	10.54		
25	3C2	March 23	W	−5.4	21	4.06		Complex structures near the dark region
26	3C5	March 18	E	−5.8	20	3.54		
27	3C5	March 29	W	−1.4	21	9.66		
28	W31(2)	Jan. 2	W	14.3	35	4.53		
29	GGD4	June 27	W	9.9	37	6.65		

plasma ions. The gyrofrequencies in the parameter that describes the wave–particle energy exchange are proportional to the field intensity. Our parameter R_{in} depends inversely on the acceleration rate, which determines its relation to the field intensity $|B_R|$. The process as a whole is very complex, its particular features are unclear, but the crucial role of the intensity of the frozen-in magnetic field may be considered to have been firmly established.

Let us now turn to the third type of slow solar-wind streams (the diamonds in Fig. 1), which, as was mentioned above, show no regular correlation between R_{in} and $|B_R|$. In the table experiments 25–29 correspond to this type of stream. Consider each of these cases separately.

Experiment 25, the table, March 25, 2000. In Fig. 1, the corresponding point with $R_{in} = 21R_S$ and $|B_R| = 4.06\ \mu T$ is close to the streamer branch (filled circles), but the coronal magnetic field here is mixed. According to the LASCO C2/SOHO data, this weak magnetic field emerges in the region of interaction between a weak streamer and the ray structure of the white-light corona. The low-speed solar-wind stream results from the interaction of the low-speed streams of two types produced by different sources in the solar corona.

Experiment 26, the table, March 18, 2000. In the correlation diagram (Fig. 2), the corresponding point has the parameters $R_{in} = 20R_S$, $|B_R| = 3.54\ \mu$T. This case is identical to the previous case. Here, the low-speed stream results from the interaction of low-speed streams from two sources: a weak streamer and the ray structure of the white-light corona.

Experiment 27, the table, March 29, 2000. In Fig. 1, the point with $R_{in} = 21R_S$ and $|B_R| = 9.66\ \mu$T is located between two branches of the slow solar wind: the branches of streamers and the slower solar wind with a ray structure of the white-light corona (open circles). Analysis of the calculated data on the magnetic field and the white-light corona emission indicates that the mixed magnetic-field structure results here from the interaction of the structure of a weak streamer, a local coronal hole, and the region of the ray structure of the white-light corona.

Experiment 28, the table, January 2, 2000. In the correlation diagram (Fig. 2), the point with $R_{in} = 35R_S$ and $|B_R| = 4.53\ \mu T$ is located unusually far from the Sun, suggesting an extremely low stream speed. This point corresponds to the mixed magnetic-field structure that results from the complex interaction of the ray structure of the white-light corona, a streamer perpendicular to the plane of the sky, and a local coronal hole.

Experiment 29, the table, June 27, 2000. In the correlation diagram, the corresponding point with $R_{in} = 37R_S$ and $|B_R| = 6.65\ \mu T$ is located, as in the previous case, unusually far from the Sun. This point corresponds to the mixed magnetic-field structure associated with the complex interaction of several structures of the white-light corona: the ejection periphery, a local coronal hole, a streamer, and the ray structure of the white-light corona.

All of the above cases of the slowest solar wind (experiments 25–29, the table) are associated with the complex interaction of several different structures of the white-light corona, i.e., several magnetic-field structures of different origins near the dark strip, a coronal region with a greatly reduced density. The above analysis shows that the lack of a correlation between R_{in} and $|B_R|$ may be due to the variations of the type of interacting sources.

CONCLUSIONS

We have established that at the maximum of solar cycle 23 (1999–2001), low-speed streams dominated in the solar-wind stream structure. The main sources of the low-speed streams at the maximum (2000) are coronal magnetic fields of a mixed type, with open and closed field lines. The regions of ray emission structure correspond to them in the white-light corona. Streams with closed loop magnetic-field structures at their bases are another, statistically less represented component of the slow solar-wind streams. In the white-light corona, they are identified with streamers. The two types of low-speed streams form two separate branches of the regular dependence in the correlation diagram between R_{in} (the location of the inner boundary of the solar-wind transition region) and $|B_R|$ (the magnetic-field intensity on the source surface, $R = 2.5R_S$). In addition, the 2000 data revealed one more, previously unknown slowest stream component. In the R_{in}–$|B_R|$ correlation diagram, it forms no regular branch. Nevertheless, this stream component can be separated into an independent group associated with the mixed magnetic field produced by the interaction between the magnetic fields of the sources of various types located near the dark strip, a coronal region with a greatly reduced density. The lack of a regular correlation between R_{in} and $|B_R|$ is probably attributable here to the variations of interacting discrete sources.

ACKNOWLEDGMENTS

The radio-astronomical data were obtained on two facilities: the RT-22 (registration number 01-10) and DKR-1000 (registration number 01-09) radio telescopes. We are grateful to the staff of the J. Wilcox Observatory for the data on solar magnetic fields and to the *SOHO* team for the data on the white-light corona structure (all of the data were retrieved via the Internet). This work was supported by the Federal Program "Astronomy," the Program "Leading Scientific Schools" (project no. 00-15-96661), and the Russian Foundation for Basic Research (project no. 01-02-16308).

REFERENCES

1. K. Asai, M. Kojima, P. K. Manoharan, *et al.*, J. Geophys. Res. **103**, 1991 (1998).
2. J. L. Fillips, S. J. Bame, B. L. Barnes, *et al.*, Geophys. Rev. Let. **22**, 3107 (1995).
3. K. Hakamada, M. Kojima, M. Tokumaru, *et al.*, Solar Phys. **207**, 175 (2002).

4. J. T. Hoeksema, J. M. Wilcox, and P. H. Scherrer, J. Geophys. Res. **87**, 10 331 (1982).
5. J. T. Karpen, *Proc. of Int. Conf. Solar Wind–9,* Ed. by Sh. R. Habbal *et al.* (AIP, Woodbury, New York, 1999), p. 47.
6. M. Kojima, K. Fujiki, K. Hakamada, *et al.*, Adv. Space Res. **25**, 1893 (2000).
7. M. Kojima and T. Kakinuma, Space Sci. Rev. **53**, 173 (1990).
8. M. Kojima, M. Tokumaru, H. Watanabe, *et al.*, J. Geophys. Res. **103**, 1981 (1998).
9. N. A. Lotova, V. N. Obridko, and K. V. Vladimirsky, Astron. Astrophys. **357**, 1051 (2000).
10. N. A. Lotova, V. N. Obridko, and K. V. Vladimirsky, Astron. Zh. **79**, 377 (2002a) [Astron. Rep. **46**, 339 (2002a)].
11. N. A. Lotova, V. N. Obridko, K. V. Vladimirsky, *et al.*, Solar Phys. **205**, 149 (2002b).
12. N. A. Lotova, K. V. Vladimirsky, I. Yu. Yurovskaya, and O. A. Karelov, Astron. Zh. **72**, 757 (1995) [Astron. Rep. **39**, 675 (1995)].
13. J. G. Luhmann, D. Larson, and J. T. Hoeksema, *Proc. of Int. Conf. Solar Wind–9,* Ed. by Sh. R. Habbal *et al.* (AIP, Woodbury, New York, 1999), p. 725.
14. E. Marsch and C.-Y. Tu, *Proc. of Int. Conf. Solar Wind–9,* Ed. by Sh. R. Habbal *et al.* (AIP, Woodbury, New York, 1999), p. 393.
15. V. N. Obridko and B. D. Shelting, Solar Phys. **137**, 167 (1992).
16. V. N. Obridko and B. D. Shelting, Solar Phys. **201**, 1 (2001).
17. B. J. Rickett and W. A. Coles, J. Geophys. Res. **96**, 1717 (1991).
18. R. Schwenn, *Physics of the Inner Heliosphere,* Ed. by R. Schwenn and E. Marsch (Springer-Verlag, New York, 1990), p. 99.
19. N. R. Sheelay, *Proc. of Int. Conf. Solar Wind–9,* Ed. by Sh. R. Habbal *et al.* (AIP, Woodbury, New York, 1999), p. 41.
20. N. Srivastava, R. Schwenn, and B. Inhester, *Proc. of Int. Conf. Solar Wind–9,* Ed. by Sh. R. Habbal *et al.* (AIP, Woodbury, New York, 1999), p. 115.
21. S. J. Tappin, G. M. Simnett, and M. A. Lyones, Astron. Astrophys. **350**, 302 (1999).
22. C.-Y. Tu and E. Marsch, Space Sci. Rev. **73**, 1 (1995).
23. K. V. Vladimirsky, N. A. Lotova, and V. N. Obridko, Geomagn. Aeron. (2003, in press).
24. Y.-M. Wang and N. R. Sheely, Jr., Astrophys. J. **355**, 726 (1990).
25. Y.-M. Wang, N. R. Sheely, Jr., J. L. Phillips, and B. E. Goldstein, Astrophys. J. **488**, L51 (1997).

Translated by G. Rudnitskii

Astronomy Letters, Vol. 29, No. 9, 2003, pp. 635–639. Translated from Pis'ma v Astronomicheskiĭ Zhurnal, Vol. 29, No. 9, 2003, pp. 715–719.

The Lagrange–Jacobi Equation in the Finite-Size Many-Body Problem

L. G. Luk'yanov, L. P. Nasonova*, and G. I. Shirmin

Sternberg Astronomical Institute, Universitetskii pr. 13, Moscow, 119992 Russia

Received March 31, 2003

Abstract—We determine the values of the barycentric energy constant that necessarily result in collisions between bodies. The standard Hill stability regions in the problem of four or more bodies are shown to be located inside the regions where collisions are inevitable. Only in the problem of three finite bodies is part of the Hill stability region preserved where the bodies can move without colliding with one another. We point out possible astronomical applications of our results. © *2003 MAIK "Nauka/Interperiodica".*

Key words: *celestial mechanics, many-body problems, Lagrange–Jacobi equation, Hill stability, body collisions.*

Consider a system of n absolutely rigid finite-size bodies M_1, M_2, ..., M_n of arbitrary shapes and densities. Each body M_i $(i = 1, ..., n)$ has a mass equal to m_i.

The mutual attraction of these bodies is characterized by the force function

$$U = \sum_{j>i} U_{ij}, \tag{1}$$

where $U_{i,j}$ is the force function of Newtonian mutual attraction of bodies M_i and M_j. The force function depends on the coordinates of the centers of mass of the bodies and on the Euler angles that determine the spatial orientation of the bodies.

The motions of bodies with force function (1) can be described by a system of differential equations of translational and rotational motion. Here, we retain only the first terms in the expansions of the force function U_{ij} into a power series in inverse mutual distances r_{ij} (Duboshin 1975):

$$U_{ij} = f \int\limits_{(M_i)} \int\limits_{(M_j)} \frac{dm_i dm_j}{\Delta_{ij}} = f\frac{m_i m_j}{r_{ij}} + \ldots, \tag{2}$$

where f is the universal gravitational constant, Δ_{ij} is the distance between the current points in the computation of integrals over the volumes of bodies M_i and M_j, and r_{ij} is the distance between the centers of mass of these bodies.

In this approximation, the $(12n)$-order differential equations of translational and rotational motion break up into two independent systems of $(6n)$-order equations, each of which separately determines the translational and rotational motions.

Below, we consider only the translational motion. We assume that bodies M_i and M_j have collided with each other if $r_{ij} = a_i + a_j$, where a_i is the distance between the center of mass of the body M_i and the most distant point of its surface.

Such a formulation of the problem allows the existence of the following Lagrange–Jacobi equation (Duboshin 1975):

$$\ddot{R} = 2U + 4h, \tag{3}$$

where

$$R = \frac{1}{m}\sum_{j>i} m_i m_j r_{ij}^2,$$

is the barycentric moment of inertia of the system of bodies, $m = m_1 + m_2 + \cdots + m_n$ is the total mass of the entire system, and h is the barycentric energy constant.

The force function of a system of n absolutely rigid bodies always obeys the following inequalities:

$$V \geq U \geq 0, \tag{4}$$

where the constant V corresponds to the value of U for a certain compact (optimum) contact of all n bodies where each body is in contact with at least two other bodies. No other compact arrangement of n bodies can yield U values higher than V.

The quantity V can be written as

$$V = \sum_{j>i} V_{ij}, \tag{5}$$

where V_{ij} is the value of the force function of mutual attraction of bodies M_i and M_j for the compact contact of the bodies mentioned above. According to (4)

*E-mail: nason@sai.msu.ru

1063-7737/03/2909-0635$24.00

and (5), we assume that for any i and j the following inequalities always hold:

$$U_{ij} \le V_{ij}. \tag{6}$$

The compact contact of all bodies mentioned above can be considered an analog of the n-tiple collision in the problem of n material bodies, although in the case of such contact there may be pairs of bodies that are not directly in contact with each other. It is clear that for such pairs the force function U_{ij} can acquire values exceeding V_{ij}. However, this fact imposes no fundamental constraints on the subsequent results.

The energy integral for the problem considered has the following form in barycentric coordinates:

$$T - U = h, \tag{7}$$

where T is the kinetic energy of the n-body system, and h is the barycentric energy constant.

The domain of possible motions of the n-body system at $h < 0$ is determined by the following inequality

$$U \ge -h. \tag{8}$$

Conditions (4) for the force function can then be refined as follows:

$$V \ge U \ge \begin{cases} -h & \text{for } h < 0 \\ 0 & \text{for } h \ge 0. \end{cases} \tag{9}$$

We now use these inequalities to derive from the Lagrange–Jacobi equation (3) via double integration the following formula:

$$\beta(t) \ge R \ge \alpha(t), \tag{10}$$

where $\beta(t)$ and $\alpha(t)$ are second-order polynomials with constant coefficients

$$\beta(t) = R_0 + \dot{R}_0 t + (V + 2h)\, t^2,$$

$$\alpha(t) = \begin{cases} R_0 + \dot{R}_0 t + ht^2 \text{ for } h < 0 \\ R_0 + \dot{R}_0 t + 2ht^2 \text{ for } h \ge 0; \end{cases}$$

R_0 and $\dot{R}_0$ are initial conditions.

The quantity R is, by its physical meaning, bounded from below by $R_{\min}$, which corresponds to a compact contact of the bodies. Therefore, R is physically meaningless outside the interval

$$\infty > R \ge R_{\min}. \tag{11}$$

Moreover, a system of n bodies may cease to exist even at R values larger than $R_{\min}$, i.e., in the case of a pairwise contact between bodies M_i and M_j.

Inequalities (10) allow qualitative results that apply to an infinite time interval to be easily obtained from formula (3). We see from (10) that any solution $R(t)$ of Eq. (3) Always lies between two parabolas. Therefore, depending on the value of energies constant h, the following conclusions can be made regarding the dynamical evolution of an n-body system.

A. Let $-V/2 > h \ge -V$. The quantity R then lies between the two parabolas (10), which tend to $-\infty$ at $t \to +\infty$. Therefore there always exists such a time instant τ, when either R becomes equal to $R_{\min}$ (n-th order collision), or a smaller number of bodies collide. These are the only possible outcomes of the evolution of n bodies in this case.

B. If $0 > h \ge -V/2$, the quantity R lies between the parabola $\beta(t)$, which tends to $+\infty$ at $t \to +\infty$, and parabola $\alpha(t)$, which tends to $-\infty$. Therefore the behaviour of the system in this case cannot be predicted. Any outcome is possible: the breakup of the system (when one or several bodies escape to infinity), a collision of one or several bodies or, finally infinitely long existence of the system as a single whole with finite R. Only in the latter case the system can be stable in the Lagrange or Jacobi sense and the conditions for B are necessary conditions for such stability. Khil'mi (1950) showed that in a stable system quantity R oscillates about some finite level.

C. Now let $h \ge 0$. In this case there are two possible scenarios for the variation of R at $t \to \infty$. Either $R \to \infty$; i.e., the system disrupts via the escape of at least one body to an infinite distance, or R decreases and at a certain time instant τ that two or more bodies collide. The initial system ceases to exist in its initial form. The second possibility can be realized only in the case a negative initial rate $\dot{R}_0$, i.e., on the downward branches of parabolas $\alpha(t)$ and $\beta(t)$.

For the problem of n material points we have $V \to \infty$, and cases A, B, and C reduce to two cases: case B, which expands to $0 > h > -\infty$, and case C, whereas case A totally disappears. Condition $h < 0$ is a necessary condition for the stability of n point bodies. Cases B and C for n material points were first considered by Jacobi (see, e.g., Subbotin (1968)).

Case A is of interest for the analysis of close encounters of finite-size bodies. Of special interest is its application in combination with the analysis of the Hill stability regions found by Luk'yanov and Shirmin (2002) and Luk'yanov *et al.* (2003) by constructing surfaces of zero kinetic energy.

The above authors give the following Hill stability criterion for the problem of n finite-size perfectly rigid bodies:

$$-V^{(n)} > h \ge -V, \tag{12}$$

where $V^{(n)}$ is the maximum value of the force function $U^{(n)}$ obtained from U by eliminating body M_n.

In inequality (12), the bodies are numbered so that $V^{(n)}$ is the greatest of $V^{(s)}$, where $s = 1, 2, \ldots, n$. If

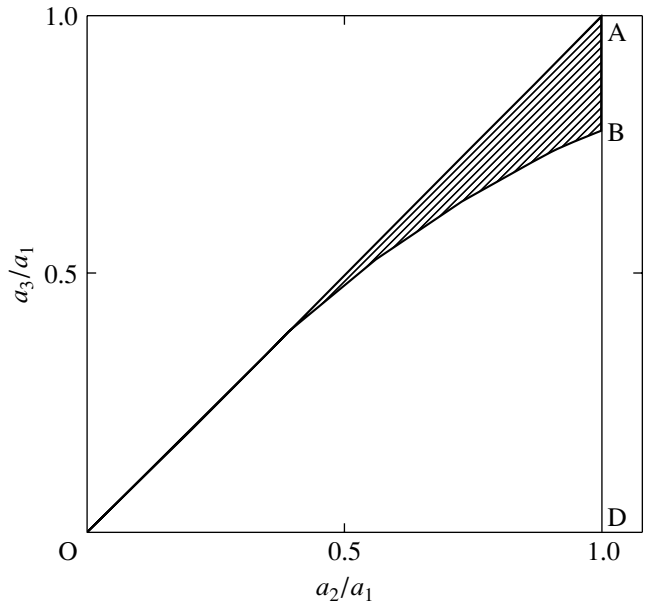

Fig. 1. Relative sizes of the bodies for which the Hill stability region is greater than the region of inevitable collisions between the bodies (dashed). In contrast, inside OVD, the region of inevitable collision of the bodies is larger than the Hill stability region.

all bodies have the same mass density, such a numbering coincides with the numbering in the order of decreasing masses when

$$m_1 \geq m_2 \geq \ldots \geq m_n.$$

Below, we also assume that the following inequalities are always satisfied for the adopted numbering:

$$U_{ij} > U_{ks} \quad \text{and} \quad V_{ij} > V_{ks}, \tag{13}$$

if $i + j < k + s$.

Case A shows that the Hill stability in the vicinity of the nth order contact of bodies is rather relative, because at $-V/2 > h \geq -V$ the motion always ends with a collision. It remains only to establish whether the Hill stability is possible outside the interval for case A. To do this, one must compare $V/2$ and $V^{(n)}$.

We now show that for the problem of four and more bodies the following inequality is satisfied

$$V^{(n)} \geq V/2, \tag{14}$$

i.e., the entire Hill stability region lies inside region **A**. Indeed, let us select in (5) all terms containing subscript n and write V in the form

$$V = (V_{1n} + V_{2n} + \ldots + V_{n-1,n}) + V^{(n)}.$$

We now substitute the resulting $V^{(n)}$ into Eq. (14) to obtain

$$V \geq 2\,(V_{1n} + V_{2n} + \ldots + V_{n-1,n})\,.$$

We then use formula (5) for V and reduce similar terms to obtain

$$(V_{1,n-1} + V_{2,n-1} + \ldots + V_{n-2,n-1}) + \ldots \tag{15}$$
$$+ (V_{1\,3} + V_{2\,3}) + V_{1\,2} \geq V_{1\,n} + V_{2\,n} + \ldots + V_{n-1,n}.$$

Given (13), it can be easily seen that inequality (15) and, consequently, inequality (14) are satisfied.

Inequality (14) becomes an equality in the case of the problem of four identical bodies of equal mass and size. Inequality (15) can then be written in the form of the following evident equality

$$(V_{13} + V_{23}) + V_{12} = V_{14} + V_{24} + V_{34},$$

because $V_{ij} = V_{ks}$ for any i, j, k, and s.

For the three-body problem, inequality (14) can be either satisfied or not satisfied, depending on the masses, sizes, and densities of the bodies. Indeed inequality (14) imposes such constraints on the sizes and masses of bodies M_1, M_2, and M_3 that inequality

$$V_{1\,2} \geq V_{1\,3} + V_{2\,3} \tag{16}$$

is satisfied. We consider the satisfaction of these constraints in more detail by assuming that bodies M_1, M_2, and M_3 are uniform spheres with mass densities ρ_1, ρ_2, and ρ_3 and radii a_1, a_2, and a_3, respectively. For such spheres, condition (16) can be rewritten as

$$\frac{a_1^3 a_2^3 \rho_1 \rho_2}{a_1 + a_2} \geq \frac{a_1^3 a_3^3 \rho_1 \rho_3}{a_1 + a_3} + \frac{a_2^3 a_3^3 \rho_2 \rho_3}{a_2 + a_3}. \tag{17}$$

If we further assume that $\rho_1 = \rho_2 = \rho_3$ and denote $x = a_2/a_1$ and $y = a_3/a_1$, we can rewrite inequality (17) in the following form:

$$F(x, y) \leq 0, \tag{18}$$

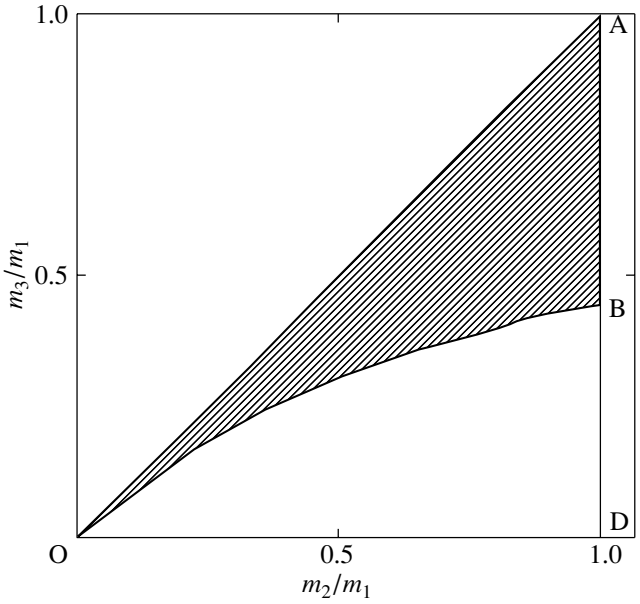

Fig. 2. Relative masses of bodies corresponding to Fig. 1.

where

$$F(x,y)=\frac{y^3}{1+y}-\frac{x^3}{1+x}+\frac{x^3y^3}{x+y},$$

and x and y obey, according to the adopted numbering, the inequalities

$$1\geq x\geq y>0. \tag{19}$$

Curve OB in Fig. 1 corresponds to the equality sign in formula (18) and the triangle OAD determines all physically admissible values of a_2/a_1 and a_3/a_1 in accordance with formula (19). In the region OBD, inequality (18) is satisfied, and in the dashed region OAB, the inequality opposite to (18) is satisfied. Figure 2 shows similar results for the relative masses m_2/m_1 and m_3/m_1.

Dashed regions illustrate such parameters of uniform spherical bodies that the Hill stability regions are greater than the collision region in case A.

The interval OD of the x axis in Figs. 1 and 2 corresponds to the passage to the limit where the mass and size of body M_3 become equal to zero. This interval is adjacent to the region OVD, where the collision conditions (18) are satisfied. In other words, if the mass (or size) of body M_3 is much smaller than that of bodies M_1 and M_2, such a system is doomed to a collision. And only if m_3 is close enough to m_2 up to $m_3=m_2$, are the Hill stability conditions satisfied and the conditions of inevitable collision (dashed region) not satisfied.

CONCLUSIONS

A simultaneous analysis of the regions of Hill stability and those of inevitable collision of bodies (case **A**) shows that in the problem of four or more bodies, the Hill stability regions exist but are always located inside the region of inevitable collision. Only in the three-body problem can the region of Hill stability be larger than region **A**. Therefore, there are combinations of masses, sizes, and densities of the bodies that obey the inequality opposite to inequality (16), and this fact ensures the Hill stability in the possible absence of collisions. This requires the satisfaction of the conditions

$$V^{(3)}<V/2,$$

$$-V^{(3)}>h>-V/2, \tag{20}$$

where $V=V_{12}+V_{23}+V_{31}$, $V^{(3)}=V_{12}$. These conditions cannot be called sufficient conditions for the long-term existence of the system, because nobody has proven that no collisions could ever take place in this case.

Figures 1 and 2 show the relative sizes and masses of the three spherical bodies of equal density, for which the Hill stability regions are larger (dashed) or smaller (OVD) than the regions of inevitable collision.

The above results concerning the Hill stability of the motions in the problem of many finite-size bodies allow astronomical applications. Thus, for example, Galactic globular clusters constitute a spherical subsystem with a strong concentration to the Galactic center. Moreover, the observed velocities of stars at galactocentric distances of several Mpc are indicative

of a nucleus mass of several million or even several billion solar masses. It is generally believed that these facts well agree with the assumption that galactic nuclei harbor massive black holes (Kononovich and Moroz 2001).

The second example corresponds to classical stellar dynamics. According to current views of the evolution of star clusters (both globular and open ones), the irrepressible contraction of the central part of the cluster—the collapse of its core—is dynamically inevitable (King 2002).

Thus, galactic astronomy and stellar dynamics allow the existence of some supermassive objects at the centers of stellar systems. This agrees completely with the conclusion of this work about the Hill stability of motions in a system of finite-size gravitating bodies. More specifically, since the size of the Hill stability region is comparable to that of the region of space inside which collisions between its constituent bodies are highly likely, an object of considerable mass and density may well exist at the center of the system.

REFERENCES

1. G. N. Duboshin, *Celestial Mechanics. Basic Problems and Methods* (Nauka, Moscow, 1975) [in Russian].
2. G. F. Khil'mi, Dokl. Akad. Nauk SSSR **70**, 393 (1950).
3. Ivan R. King, *An Introduction to Classical Stellar Dynamics* (Editorial URSS, Moscow, 2002).
4. É. V. Kononovich and V. I. Moroz, *A General Course in Astronomy* (Editorial URSS, Moscow, 2001) [in Russian].
5. L. G. Luk'yanov and G. I. Shirmin, Pis'ma Astron. Zh. **28**, 477 (2002) [Astron. Lett. **28**, 419 (2002)].
6. L. G. Luk'yanov, L. P. Nasonova, and G. I. Shirmin, Pis'ma Astron. Zh. **29**, 317 (2003) [Astron. Lett. **29**, 274 (2003)].
7. M. F. Subbotin, *Introduction to Theoretical Astronomy* (Nauka, Moscow, 1968) [in Russian].

Translated by A. Dambis

Astronomy Letters, Vol. 29, No. 9, 2003, p. 640. Translated from Pis'ma v Astronomicheskiĭ Zhurnal, Vol. 29, No. 9, 2003, p. 720.

Corrections to the Paper by M.Yu. Petukhov and Yu.V. Petukhov* "Parametric Generation of Acoustic-Gravity Waves by Alfvén Waves in the Solar Atmosphere," Astron. Lett. 28, 335 (2002)

When interpreting the physical meaning of the two groups of terms with the coefficients B_1, B_1^* and B_2, B_2^* in expression (41) for the vertical oscillation velocity in an acoustic-gravity wave at a difference frequency, we made a mistake. Actually, our explanations for the terms with B_1, B_1^* should refer to the terms with B_2, B_2^*; in turn, the explanations for the latter should refer to the terms with B_1, B_1^*. Therefore, we made the following erroneous assertions in the text of our paper.

On page 387, in the left column from line 1 to line 3 from the top, we incorrectly assert that "... in the same direction (the terms with B_1 and B_1^* in (41)) and in opposite directions (the terms with B_2 and B_2^* in (41))." The correct version should be "... in opposite directions (the terms with B_1 and B_1^* in (41)) and in the same direction (the terms with B_2 and B_2^* in (41))."

Therefore, on page 388, in the right column in lines 21 and 22 from the bottom, and on page 390, in the right column in lines 1 and 2 from the bottom, we incorrectly assert "... in opposite directions...." The correct version should be "... in the same direction...."

Thus, on page 388, in the right column from line 20 to line 26 and on page 390 in the right column from line 1 to line 6 from the bottom, the same phrase that constitutes one of our conclusions should be correctly read as follows: "... the nonlinear interaction of Alfvén waves propagating in the same direction is the predominant parametric generation mechanism of AGWs at the difference frequency."

This correctly formulated conclusion that follows from our analytical and numerical results is no longer consistent with the conclusions of Wentzel (1974) and the assertions made on their basis by Kaplan *et al.* (1977) and Priest (1982) that the most favorable conditions for the nonlinear transformation of Alfvén-wave energy into acoustic-wave energy arise only in the presence of oppositely directed flows of nonlinearly interacting Alfvén waves. This contradiction stems from the fact that Wentzel (1974) considered the nonlinear interaction of plane Alfvén waves in a homogeneous medium, because he disregarded the increase in their velocity with height, which is inversely proportional to the square root of the decreasing density of the solar atmosphere. It is easy to verify that the following assertion results from this simplified statement of the problem in the paper by Wentzel (1974): acoustic waves at a relatively low difference frequency can be generated by counterpropagating Alfvén waves only at a ratio of the speed of sound to the Alfvén-wave velocity smaller than unity, and unidirectional Alfvén waves can generate acoustic waves only at zero difference and sum frequencies.

Taking into account the continuous stratification of the Alfvén-wave velocity automatically gives rise to oppositely propagating and linearly interacting (coupled) Alfvén waves at each point of the medium. For these waves, the dispersion relations for plane waves used by Wentzel (1974), Kaplan *et al.* (1977), and Priest (1982) no longer hold. Therefore, the relations derived by Wentzel (1974) cannot be used to properly study the parametric generation of acoustic-gravity waves (see, e.g., Kaplan *et al.* 1977; Priest 1982).

REFERENCES

1. S. A. Kaplan, S. B. Pikelner, and V. N. Tsytovich, *Physics of Solar Atmospheric Plasma* (Nauka, Moscow, 1977) [in Russian].
2. E. Priest, *Solar Magnetohydrodynamics* (Reidel, Dordrecht, 1982; Mir, Moscow, 1985).
3. D. G. Wentzel, Solar Phys. **39**, 129 (1974).

*E-mail: petukhov@hydro.appl.sci-nnov.ru

1063-7737/03/2909-0640$24.00